Waveguide photonic microstructures in III-V semiconductors

A thesis for the degree of

Doctor of Philosophy (Ph.D),

submitted to the Faculty of Engineering,

Glasgow University

by

Christopher J. M. Smith

May 1999

ProQuest LLC.
789 East Eisenhower Parkway
P.O. Box 1346
Ann Arbor, MI 48106 – 1346

Abstract

Photonic microstructures are a class of periodic dielectric structures which could lead to a significant evolution in optoelectronic devices. There are, however, several problems with photonic crystals, not least of which is the fabrication of these artificial structures. The fabrication of these artificial crystals in III-V semiconductor materials, specifically optical waveguide heterostructures, have been investigated. Improvements in the fabrication of GaAs/AlGaAs photonic bandgap structures have been made and the development of an AlAs epitaxial layer as a pattern transfer mask has been demonstrated. Two-dimensional photonic bandgap structures have been characterised and good agreement has been obtained between theory and experimental measurements. Subsequently, semiconductor microcavities incorporating photonic bandgap mirrors have been fabricated with mirror reflectivities higher than 90% and high mode Q factors, $Q \approx 500$. The results indicate that photonic bandgap technology has the potential to provide the desired engineering of the environment of a light emitter which will allow control of the emission process. The microstructuring of the material, however, creates significant obstacles to electroluminescence and much research in this area is required if any benefit of photonic microstructures are to be seen.

Acknowledgements

I would like to express my sincere gratitude to the following people and organisations who were key to a successful outcome of this project.

Professor Steven Beaumont for permitting me to do my doctoral work in the department which is fortunate to possess some of the most extensive facilities available in the country. My supervisors at Glasgow University, Professor Richard De La Rue and Doctor Thomas Krauss for providing me with such an interesting and challenging project and for the many useful discussions including the transatlantic and transpacific emails during their sabbaticals. Professor Peter Laybourn who so kindly supervised me during the absence of my two principal supervisors and for the useful advice he provided during that time. I am indebted to Professor Mike Burt and Doctor Robert Grant of British Telecommunications Laboratories for their support and the interest they showed in the project.

The Optoelectronics Research Group and all my colleagues for their support, advice and for the numerous tea-table stories that helped the bad days pass quickly.

The Nanoelectronics Research Centre and all the excellent technical staff without whom this project would have been exceedingly more difficult. In particular, I wish to thank Doctor Stephen Thoms for providing some software fixes on the beamwriter, so that some of my awkward jobs would run.

The Dry Etch Research Group and, in particular, Professor Chris Wilkinson and Doctor Saad Murad for invaluable instruction in the nuances of dry-etching. Dave Clifton and Bill Ward for helping me produce some good devices to measure.

Doctor Martin Dawson at the Institute of Photonics for allowing me to use the oxidation rig and for his advise on all matters relating to steam oxidation.

Dominique Labilloy, Henri Benisty and Claude Weisbuch for their generous invitation to use their facilities at the Ecole Polytéchnique, Palaiseau, France and for the interesting work that we have carried out together and the many useful discussions that have resulted.

Finally, to my wife Nicola and my parents my deepest and most sincere thanks for your moral support without which this project may never have been finished.

To my wife, Nicola, and my parents

TABLE OF CONTENTS

1. INTRODUCTION 1

1.1 Photonic bandgap materials 3

1.2 Photonic bandgap project highlights 9
1.2.1 Initial pattern transfer 9
1.2.2 Novel intermediate pattern transfer layers 11
1.2.3 Pattern transfer to GaAs/AlGaAs 12
1.2.4 Circular resonator with Bragg mirrors 13
1.2.5 In-plane microcavities 14

1.3 Outline 15

2. THEORY 16

2.1 Electromagnetic waves in periodic structures 17
2.1.1 Electromagnetic wave propagation 17
2.1.2 Periodic dielectric structures 18
2.1.3 Wave propagation in periodic structures 19
2.1.4 Equivalence of photonic and electronic bandgaps 24
2.1.5 Photonic bandgap calculations 25

2.2 Optical waveguide 29

2.3 Fabry-Perot cavities 33

2.4 Conclusions 36

3. DEVICE FABRICATION 37

3.1 Lithography 39
3.1.1 Pattern design 40
3.1.2 Electron-beam lithography 42

3.2 Pattern transfer 44
3.2.1 Deposition of dielectric films 44
3.2.2 Transfer of features from PMMA to SiO_2 and SiN_x 45
3.2.3 Pattern transfer to GaAs/AlGaAs 46
3.2.4 Transfer of features to InP-based materials 49

3.3 Conclusions 52

4. FABRICATION PROCESS DEVELOPMENTS 53

4.1 PMMA as an initial pattern transfer mask 53
4.1.1 Introduction 53
4.1.2 Comparison of different resists in S100 machine 54
4.1.3 Comparison of PMMA etch rates in different plasmas in S100 machine 54
4.1.4 Etching of PMMA in CHF_3 57
4.1.5 Application of results to pattern transfer 62
4.1.6 Conclusions 63

4.2 Modified AlAs layer as an intermediate pattern transfer layer 64
4.2.1 Wet, thermal oxidation of AlAs 65
4.2.2 Problems with AlAs oxidation 67
4.2.3 Comparison of masks 68
4.2.4 Plasma fluorination of AlAs 69

4.3 Conclusion 72

5. PHOTONIC BANDGAP STRUCTURES : DESIGN CONSIDERATIONS AND CHARACTERISATION 73

5.1 Optical waveguide design 73

5.2 Photonic bandgap structure design 77

5.3 Experimental set-up 79

5.4 Final sample design 82

5.5 PBG structure characterisation 84

6. PHOTONIC BANDGAP STRUCTURES AND MICROCAVITIES 91

6.1 Microcavities 91

6.2 Disk-like microcavity with Bragg reflectors 94
6.2.1 Cylindrical cavities - theory 96
6.2.2 Design and implementation 98
6.2.3 Results 99

6.3 One dimensional microcavity defined by 2-D PBG mirrors 102
6.3.1 Design and implementation 103
6.3.2 Results and discussion 104

6.4 Two-dimensional microcavities with 2D photonic bandgap structures 109
6.4.1 Cavity layout and implementation 110
6.4.2 Results and discussion 112

6.5 Conclusions 118

7. FUTURE WORK 119

7.1 Electron-beam lithography 120

7.2 Wet, thermal oxidation of AlAs in optoelectronic devices 125
7.2.1 Intermediate pattern transfer mask 125
7.2.2 Increased out-of-plane confinement 126

7.3 Etching of InP-based materials 127

7.4 Loss mechanisms in microcavities with 2D PBG boundaries 128

7.5 Photonic bandgap defects in GaAs materials 129

7.6 InP membrane waveguides 130

7.7 Hexagonal cavities in a 2D PBG environment 131

7.8 Photonic crystal waveguides 132

7.9 Improved characterisation methods 134

7.10 Electroluminescence 134

8. CONCLUSIONS 136

9. PUBLICATIONS ARISING FROM THIS WORK 138

9.1 Journal 138

9.2 Conference 139

10. BIBLIOGRAPHY 141

1. Introduction

The invention of the laser in 1960 [1] and the optical fibre in 1966 [2] revolutionised the world in many ways: they enabled the realisation of transatlantic fibre optic cables, which allow thousands of transatlantic telephone conversation simultaneously; CDs allow the storage of megabytes of information and rely on laser diodes to read and write information; the Internet and the World Wide Web would have been impossible without the means of transmitting data over large distances in a matter of seconds; many modern biological methods rely on the optical investigation and characterisation of molecules. These two basic inventions and the devices that they have spawned affect everyone in everyday life and mark a tremendous achievement of engineering. These great advances, however, have been made with individual devices or with a combination of a few devices integrated together. The integrated optoelectronics revolution, the arrival of "optoelectronic VLSI", as first suggested 20 years ago [3], has still to take place. The two main reasons why there is not an equivalent of Moore's Law for integrated optoelectronics are perhaps two-fold: firstly, optical devices are more difficult to scale as there is not an optical equivalent of Coulombic interactions and, secondly, high current densities are required for many devices, which creates temperature dissipation and power handling problems.

The problem of device size is difficult because in certain applications, for given properties, specific device dimensions are required. As an example, in Fabry-Perot cavities, the length of the cavity defines many of the important properties of the resonator, such as the free-spectral range, the mode spacing and the full-width at half maximum of the resonant mode [4]. Also, the Fabry-Perot cavities used for semiconductor lasers are frequently defined by cleaved facets and so, without high reflection coatings, the maximum reflectivity is 30% - leading to high threshold current densities [5]. Moreover, cleaving stripe lasers into the desired dimensions

becomes increasingly difficult as the length of the cavity is reduced. Even in purely passive devices, there is the important issue of steering the optical signal around the chip: as there is no optical equivalent of a Coulombic potential, sharp bends typically lead to substantial propagation losses as the optical confinement is not strong enough to prevent the guided light from radiating out of the waveguide. This design consideration means that the radius of curvature on devices is limited to greater than about 100 μm, which in turn affects the level of integration.

The level of integration is also limited by the low external quantum efficiency of many light emitting devices. As an example, in a light emitting diode, only 3% of the generated photons actually lead to visible external radiation [5]. This low figure of light extraction results from the low internal critical angle for light extraction and also the reabsorption that occurs in active devices. Many attempts have been made to improve this figure by clever design of the packaging [6], by texturing the surfaces [7] and by engineering the emitter structure itself to have a higher internal quantum efficiency, for example by the use of quantum well [8] and quantum dot active layers [9]. The highest external quantum efficiency achieved to date in a microcavity LED, however, is only 23% [10]. The use of quantum wells and quantum dot layers increases the external quantum efficiency by increasing the internal quantum efficiency of the emitters [5]. In order to increase the internal quantum efficiency further, it will be necessary to have more control over the spontaneous emission process.

In effect, these two problems could be considered two sides of the same coin: the need to move to a regime in which there are stronger light-matter interactions, which can confine the light in smaller structures and which can control the emission process itself. One candidate to perform these tasks that was first suggested in 1987 was Photonic Bandgap (PBG) Materials [11] - a field which has been actively researched in the last decade [12-15].

1.1 Photonic bandgap materials

Photonic bandgap materials is the term which describes a class of 1-, 2- and 3-D artifical structures in which there is a large modulation of the electric permittivity on the length-scale of the photon wavelength. These periodic structures will satisfy the Bragg condition at specific wavelengths [4], which in turn leads to coherent back reflection of the incident electromagnetic radiation, and to stop- and pass-bands in the electromagnetic spectrum. The position and width of these bands is controlled by the periodicity of the structure and also the difference in the propagation constants of the different media contained in the structure. Periodic structures and, in particular gratings, have been used in optical devices for many years, e.g. distributed feedback lasers [16], distributed Bragg reflector lasers [17] and fibre elements for pulse shaping and dispersion compensation [18-21]. Therefore, the general concepts of periodic optical structures are well established and are successfully used in the design of current optical devices. The difference between gratings and PBG structures is, however, both subtle and very important, particularly for many of the applications to which this technology will be applied. Gratings are often characterised by their coupling coefficient, κ, a term which is used in coupled mode theory [22]. In gratings, κ is typically on the order of tens of inverse centimetres, whereas its value in PBG structures would be of the order of several inverse micrometres.[1] These values of κ give a quantification of the strength of the Bragg reflection and give an indication of the distance over which complete reflection of the incident wave occurs. PBG structures could, therefore, be considered a limiting case of conventional gratings, but there is more. PBG structures, as well as producing stop- and pass-bands, also alter the photonic density of states (DOS) [11]. This alteration in the photonic DOS is another key

[1] In coupled mode theory one of the key assumptions is a weak refractive index modulation, so that only the first principal backard and forward travelling waves need be considered. In PBG structures, this condition is not fulfilled and so the theory cannot be rigorously applied. However, the nomenclature of coupled mode theory is still useful in describing PBG structures as the theory is well understood.

factor for future devices and is the main physical effect by which the control of emission processes will be achieved. In this case also, the range where the DOS is zero is controlled by the period, the fill-factor (also known as the mark-space ratio) and the lattice, which defines the periodic structure (Fig. 1.1).

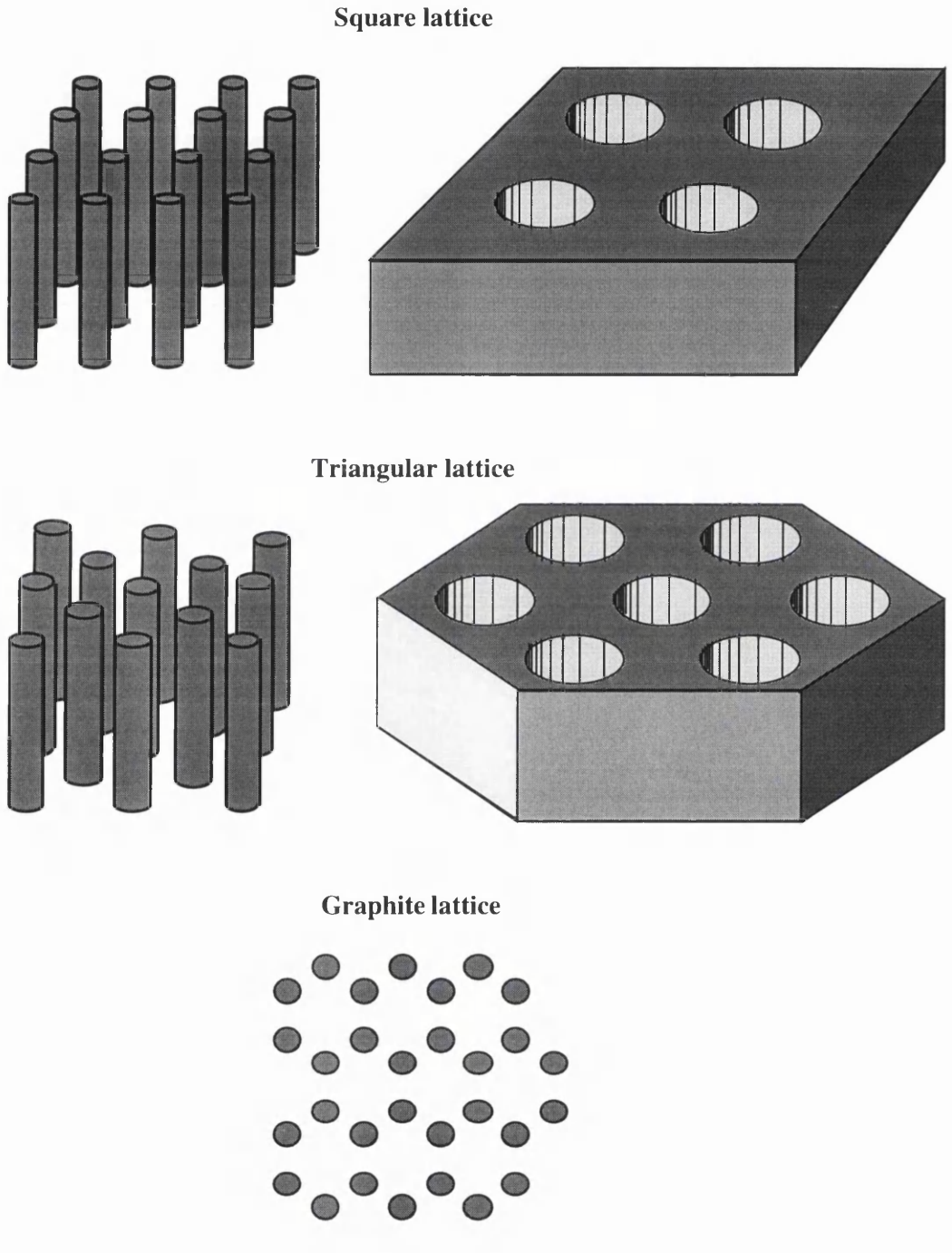

Fig. 1.1 Various 2D PBG lattices.

It is the alteration of the propagation of electromagnetic waves through these periodic structures, caused by the modulation of the bulk material properties, that produces all these interesting effects. Similar phenomena are also observed for the propagation of electrons in crystals, where the atomic lattice sites produce a periodic modulation of the electrical potential [23]. In fact, many of the ideas associated with the electronic analogy are directly transferrable into the photonic case and terms such as Brillouin zones, reciprocal space and Bloch wave functions are used in the discussion of PBG structures [11]. More closely analagous is the propagation of X-rays in crystals [23], for which the Bragg resonance is used to analyse the crystalline structure of different materials. The theories for all of these cases are very similar and, therefore, there is a great depth of knowledge from which to draw. Moreover, the fact that the electromagnetic wave equation, which describes the propagation of an electromagnetic wave through any medium, is scalable from one wavelength to another means that many theoretical results are expressed in terms of normalised frequency, usually wavelength normalised against the period [12].

Indeed, it was the scalability of the electromagnetic wave equation that led Yablonovitch and his group at Bellcore to be the first to demonstrate a true photonic crystal (a 3-D PBG structure) [24]. They were able to manufacture a photonic crystal in a high dielectric constant material (stycast) that gave a PBG at microwave frequencies, 13 to 16 GHz, and by doing so, proved the initial concept. It was far easier to fabricate a photonic crystal for these frequencies as the periods are large, of the order of several millimetres, and so could be manufactured by conventional mechanical drilling. This first experimental demonstration followed shortly after theoretical calculations by several groups predicted that a diamond structure would yield a full 3-dimensional bandgap [25-27]. The good agreement between theory and experiment showed that photonic bandgaps could be produced at all electromagnetic wavelengths, if only suitable

materials could be found and if the fabrication problems associated with smaller periods could be overcome.

This first photonic crystal was investigated further and similarities between the photonic and the electronic cases became ever clearer: photonic donor and acceptor states associated with intentionally introduced lattice defects were demonstrated [28]. Other structures, based on the diamond lattice configuration, were investigated in the microwave regime, particularly the "woodpile" structure [29-32], which was easier to fabricate. Furthermore, it had the ability to be more easily scaled, as these woodpile structures were fabricated using standard silicon micromachining processes [33, 34]. In fact, this structure pushed the spectral position of the PBG into the millimetre range (94 GHz) [29] in the first instance and then at higher, sub-Terahertz frequencies (450 GHz) [30] and most recently at 10 μm (30 Thz) [35]. Subsequent to the early demonstration of these effects, many applications of photonic crystals at microwave frequencies have been demonstrated, including antenae with increased efficiency and directionality [32, 36-49] and filters [50, 51].

The fabrication of these structures involved ingenious use of existing technologies and required pain-staking attention. It was not until 1993 and 1994 that the first attempts were made to fabricate PBG structures at optical wavelengths, due to the sub-micron periods that were required [52-54]. These initial attempts were carried out in III-V semiconductors, this being essentially market driven due to the extensive use of these materials in light-generation, the telecommunications industry and high-speed electronics. Moreover, the existence of well-established micro– and nano-lithography fabrication technology in these materials was readily applicable to the fabrication of 1- and 2-D PBG structures [55]. Photonic bandgap structures have been fabricated in other materials such as synthetic opal [56-71], macroporous silicon [72-75], PbO glasses [76-78], silica fibre [79-83], colloids

[84-87] and also in metals [88-92]. A great deal of effort is currently being focussed on semiconductors, however, as they offer the greatest potential for optoelectronic integration and control of emission processes.

One-dimensional photonic bandgap structures are easier to understand, due to the limited number of variables, and so the first successful measurements were made on 1D semiconductor PBG structures [93]. The added complexity of 2D structures meant that an exhaustive characterisation took another year or two. 2-D structures have the added complication over 1-D structures in that the lattice type and shape of the features is also important. Theoretical results have mapped out the bandgaps for triangular, square and graphite lattice configurations for both holes and pillars and experimental results have characterised the important cases for device applications [12]. In particular, arguably the most important case in semiconductor integrated optics is that of a triangular lattice of holes, as this produces the largest normalised bandgap [12]. Most of the work, therefore, has focussed on this configuration, although some groups have looked at graphite pillars [94-97], but pillars do not lend themselves well to integration as they require free-space propagation. Waveguide photonic microstructures in constrast to pillar microstructures, suffer from diffractive loss primarily into the substrate at the multiple semiconductor / air interfaces. These losses can be minimised by the use of optical mebrane waveguides and by careful choice of the lattice parameters [98]. The majority of PBG structures that have been investigated, however, have overcome this problem by using smaller etched features to minimise the out-of-plane diffraction, which means these structures do not posses a complete bandgap for both polarisations [99]. Transmission measurements of a 2-D triangular lattice of holes have demonstrated the presence of 2-D PBGs [99] and high Q cavities associated with defects in 1-D [100-102] and 2-D PBG structures [103]. Recently, an integral set of transmission, reflection and in-plane

diffraction measurements was made on 2-D PBG structures, which clearly demonstrated most of the effects expected of a 2-D PBG structure [104]. In particular, the full characterisation highlighted the need to consider reflection, transmission and in-plane diffraction when discussing the properties of 2-D PBG structures. Three-dimensional PBG structures have been investigated but due to the difficulties of fabrication at optical wavelengths only a few semiconductor photonic crystals have been made [105-108]. The principle of fabrication was similar to that used to manufacture the first photonic crystal, namely 'drilling' holes in the material, but in this case reactive-ion beam etching was used, as opposed to mechanical drilling. Unfortunately, the difficulty of fabrication meant that only four periods of this photonic crystal were produced and, therefore, the optical results were not as impressive as for the millimetre-wave photonic crystals [106].

More recent results have demonstrated the use of the technology in initial device structures: the first attempt to use 2-D PBG structures as mirrors for laser cavities did not result in a clear reduction in the threshold current density, as would be expected from the reduction in the photon DOS [109]; a 1-D PBG structure has been used as one of the mirrors in a Fabry-Perot laser cavity and high reflectivities, short cavity length laser and milliampere threshold currents were obtained [110]. More recent results have also shown the application of 1D PBG technology to circular microresonators producing increased confinement and high Q factor modes [111]. These results show that investigations of the application of PBG technology in the field of microcavities is well advanced, but much work still remains to be done to fully understand the physics of light-emitting structures in which there is interaction between the light and the surrounding structure. It may be possible eventually that either semiconductor microcavities or PBG structures will produce sufficiently strong light-matter interactions that quantum optical effects, such as spontaneous emission modification, will be observed.

1.2 Photonic bandgap project highlights

The fabrication processes available in the department at Glasgow at the start of the research in this field in 1993 were satisfactory [53], but there was little process latitude and so the properties could vary from one set of structures to another. A major part of my work has been focused on improving the fabrication processes for the GaAs/AlGaAs material system and on establishing a process for the InP-based material system also. The second part of the project has been to fabricate and characterise device-like structures which utilise PBG technology, particularly in the area of GaAs-based microcavities.

1.2.1 Initial pattern transfer

Polymethylmethacrylate (PMMA) is still the most commonly used resist for electron-beam lithography. In part, this is due to its moderate sensitivity and to the high aspect-ratio, nanometre-scale features that can be produced. However, PMMA has long been known to be a poor masking material for subsequent pattern transfer processes, especially those involving plasmas. My work has highlighted some of the critical issues involved in improving the performance of PMMA during reactive-ion etching (RIE) [112]. Specifically, the role of the oxygen background level in the RIE machine is found to be critical in obtaining good selectivities and low RIE lag.[2] The combination of both good selectivity and low RIE lag has allowed the improved pattern transfer of sub-micron features from PMMA to dielectrics (SiO_2 and SiN_x), metals (Ti) and semiconductors (GaAs/AlGaAs).

The transfer of patterns from PMMA to other materials, particularly silica and silicon nitride, is very important to the fabrication of PBG structures. The

[2] RIE lag is the term used to describe the observed reduction in material etch rate for features with smaller dimensions.

improved selectivities allowed better pattern transfer of 2-D PBG structures from PMMA to SiN_x (Fig. 1.2). This result is applicable to SiO_2 also as the RIE process used for SiO_2 is identical to that used for etching SiN_x. Moreover, improved pattern transfer of PBG structures from PMMA to GaAs and AlGaAs was also made possible (Fig. 1.3).

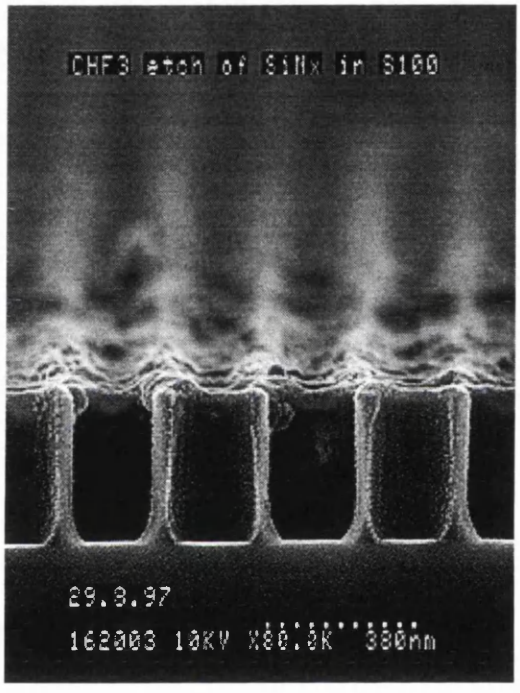

Fig. 1.2 2D PBG structure in SiN_x fabricated by CHF_3 reactive-ion etching using a 200 nm thick PMMA mask.

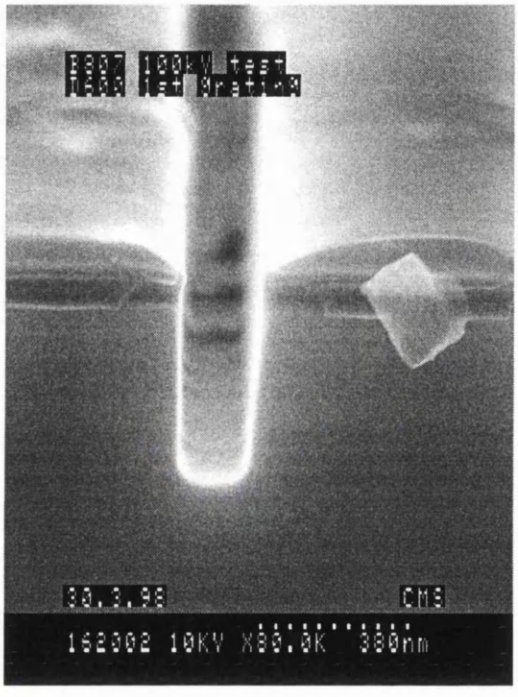

Fig. 1.3 Grating in GaAs fabricated directly by $SiCl_4$ reactive-ion etching using a 200 nm thick PMMA mask.

1.2.2 Novel intermediate pattern transfer layers

The use of intermediate pattern transfer layers, particularly SiO_2 and SiN_x, in the fabrication of PBG structures is widespread. The thin film of SiO_2 or SiN_x needs to be deposited onto the epitaxial material, however, which adds another degree of complication to the fabrication process. Moreover, deposition of thin films either by sputtering or from a plasma can alter the surface regions of the epitaxial material and cause damage to epitaxial layers beneath the surface. Therefore, the possibility of eliminating this deposition stage is attractive. My research into the use of an AlAs layer incorporated into the epitaxial growth and its subsequent modification by wet, thermal oxidation or plasma fluorination has shown encouraging results [113]. Selectivities as high as 70:1 between an oxidised AlAs mask and GaAs have been observed and aspect-ratios of at least 10:1 have been obtained for 1-D PBG structures with a 200 nm period (Fig. 1.4).

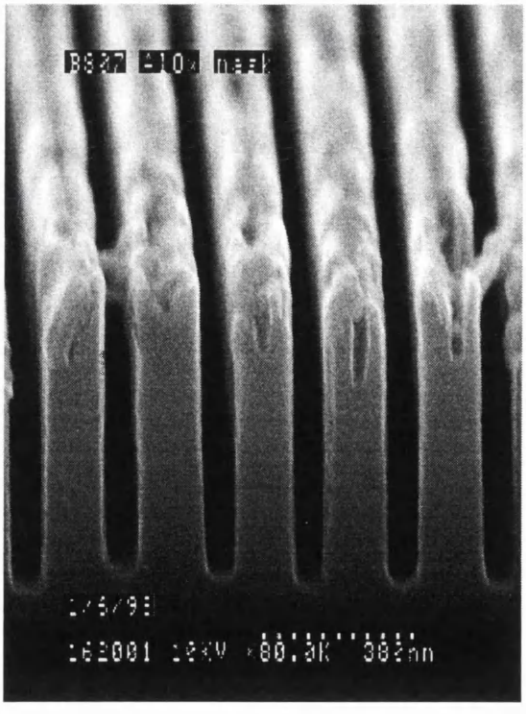

Fig. 1.4 Wet, thermally oxidised AlAs layer used to transfer nanometre features to GaAs using $SiCl_4/O_2$ reactive-ion etching.

1.2.3 Pattern transfer to GaAs/AlGaAs

The ability to produce features in SiN_x and SiO_2 that have more vertical sidewalls and that are an accurate copy of the initial pattern in the PMMA has eased the narrow fabrication tolerances associated with PBG structures. Furthermore, this ability has helped to improve the reliability of fabrication between one set of samples and the next. My research has also resulted in an improvement in the susbequent pattern transfer from the SiN_x mask to the GaAs/AlGaAs epitaxial material (Fig. 1.5). In particular, the selectivity between the SiN_x and the GaAs has been increased slightly and the verticality of the structures in the epitaxial material has been improved. The combination of all these elements has further eased the difficulties in the fabrication of GaAs-based PBG structures.

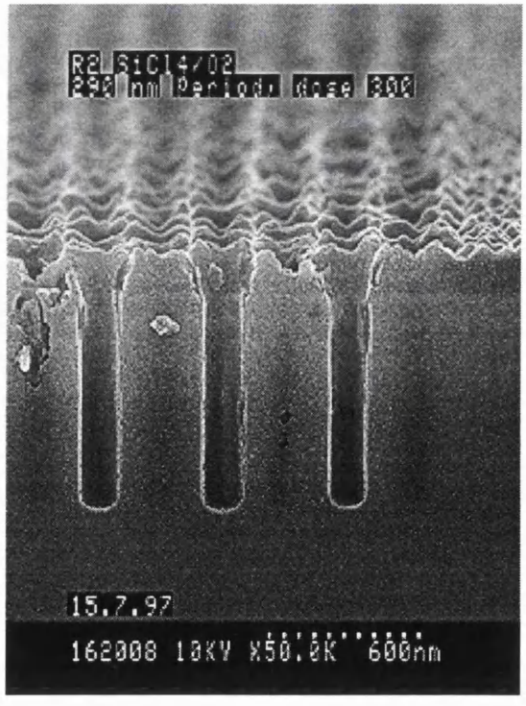

Fig. 1.5 2D PBG structure in an AlGaAs heterostructure fabricated using $SiCl_4/O_2$ RIE.

1.2.4 Circular resonator with Bragg mirrors

One of the important applications of PBG technology will be in the area of microcavity resonators. Circular microcavities (Fig. 1.6) have been fabricated by me and colleagues in France have characterised them and good experimental agreement have been obtained with simple theoretical models [111]. The high-Q modes supported by these circular microresonators, bounded by essentially 1-D PBG structures, are indicative of high reflectivities and good lateral confinement. These results contribute to a more complete understanding of the physical effects observed in microcavities and have shown that micron-sized circular resonators with periodic boundaries can be fabricated.

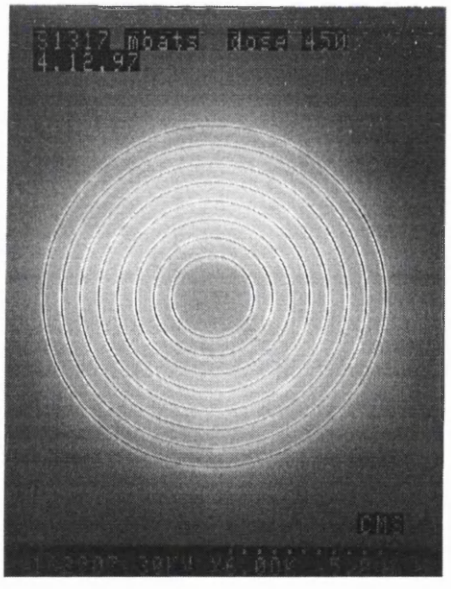

Fig. 1.6 SEM micrograph showing a plan view of a circular microcavity with a Bragg reflector.

1.2.5 In-plane microcavities

Another interesting example of a microcavity that I have explored during this project is a 1-D Fabry-Perot resonator bounded by 2-D PBG mirrors (Fig. 1.7) [114]. High reflectivities (R>90%) and correspondingly low transmission values (T<5%) have been obtained for these mirrors and modes with high Q values have also been obtained (Q=150). Moreover, a good agreement with the well-established Fabry–Perot cavity theory has been obtained and a constant shift in the resonance wavelength is observed for a constant increase in the cavity length. The heterostructure cavity losses, however, have been estimated at about 30% and so further work is required to identify these losses in order to maximise the optical confinement of the cavity.

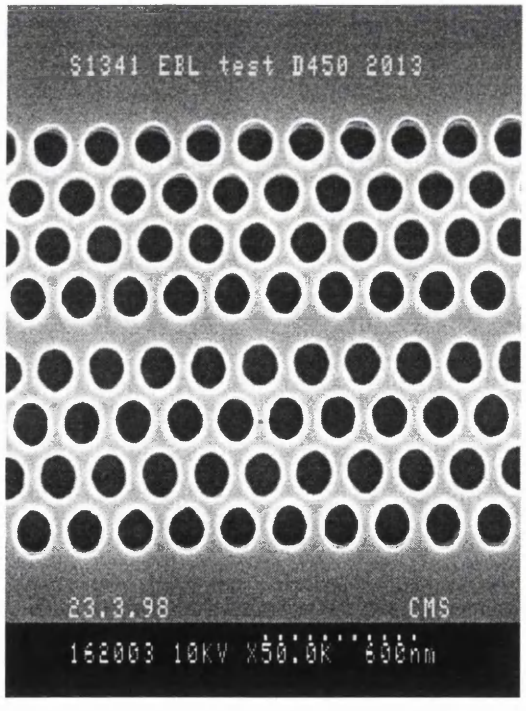

Fig. 1.7 SEM micrograph showing plan view of 1D Fabry-Perot microcavity with 2D PBG mirrors.

1.3 Outline

The remainder of the thesis is laid out as follows:

In chapter two, the basic theory relating to photonic bandgap structures is discussed, as well as the necessary theory relating to Fabry-Perot resonators. The third chapter details the fabrication processes and the fourth chapter expands on various developments in the fabrication processes made during this project. The design strategy for PBG structures, the characterisation method used in this project and the results obtained are discussed in Chapter 5. Chapter 6 describes the results for different types of planar microcavities with PBG boundaries. The future work is outlined in Chapter 7 and the project conclusions are given in Chapter 8.

2. Theory

The field of photonic bandgap structures is an amalgamation of many ideas from different areas of physics, such as solid-state [23], electromagnetism [115, 116] and X-ray diffraction [23]. Therefore, much of the theory and methods of calculation already established in these fields could be readily applied to this new area of research. The basic theory relating to photonic bandgap structures will be detailed here and the possible methods of calculation alluded to briefly. More emphasis will be placed on simpler 1D models which allow the basic properties to be explored and which can be applied with care to the more complex cases.

One of the key considerations in PBG structures is the interaction of the electromagnetic wave and its environment. In the case of semiconductor based PBG structures, there is not just an interaction with the periodic structure, but the optical wave is in many instances confined in an optical waveguide. The optical waveguide is very important, as it provides additional confinement in the vertical dimension, but one which is relatively weak compared with the effect of strong periodic index modulation. The design of waveguides in which PBG structures will be realised is complicated by several factors, however, such as the limits of the fabrication process and the material properties themselves. It will be shown that these variables must be fully considered in the design.

The optical waveguide provides one degree of optical confinement, and PBG structures can provide a further two degrees of in-plane confinement. In particular, PBG structures can be used as mirrors for defining Fabry-Perot cavities and Fabry-Perot theory can be used to determine the resonant wavelength, even for these complex structures, if the appropriate boundary conditions are used.

2.1 Electromagnetic waves in periodic structures

2.1.1 Electromagnetic wave propagation

The properties of electromagnetic waves travelling through dielectric media can be obtained from Maxwell's equations, which are given by:

$$\nabla.\mathbf{D} = \rho \tag{2.1}$$

$$\nabla.\mathbf{B} = 0 \tag{2.2}$$

$$\nabla \times \mathbf{E} = -\frac{\partial \mathbf{B}}{\partial t} \tag{2.3}$$

$$\nabla \times \mathbf{H} = \mathbf{J} + \frac{\partial \mathbf{D}}{\partial t} \tag{2.4}$$

where **D** is the electric flux density, **B** is the magnetic flux density, **E** is the electric field strength, **H** is the magnetic field strength, ρ is the charge density and **J** is the conduction current density. In the media under discussion all the usual assumptions are made, namely that there is no surface charge and the dielectric conductivity and losses are ignored (ρ = **J** = 0). Two other relationships that apply in a linear, isotropic and homogeneous media are :

D=ε**E** , where ε is the electric permittivity (F/m);

B=μ**H** , where μ is the magnetic permeability (H/m).

The electromagnetic wave equation, which is the basis for the analysis of electromagnetic wave propagation in any medium, is obtained from Maxwell's equations. If the electric field is a plane wave with a time variation given by:

$$\mathbf{E} = \mathbf{E}_0 e^{j\omega t} \tag{2.5}$$

where $\omega=2\pi f$ is the angular frequency, then the electromagnetic wave equation in a medium with a relative permittivity, ε_r, and a relative permeability, μ_r, in Cartesian coordinates is:

$$\nabla^2\mathbf{E} + k^2\mathbf{E} = 0 \tag{2.6}$$

where $k=k_0n=\omega n/c=\omega\sqrt{(\varepsilon_0\varepsilon_r\mu_0\mu_r)}$, n being the refractive index. It should be noted that ε_r is a function of frequency, so the refractive index is more correctly written $n(\omega)$. This is an eigenvalue equation and has a general plane wave solution :

$$\mathbf{E}(\mathbf{r}) = E_0 \exp(-j\mathbf{k}.\mathbf{r}) \tag{2.7}$$

where $\mathbf{k}=\mathbf{a}_x k_x+\mathbf{a}_y k_y+\mathbf{a}_z k_z$ and $\mathbf{r}=\mathbf{a}_x x+\mathbf{a}_y y+\mathbf{a}_z z$.

It can be shown that the electric and magnetic fields are perpendicular to each other and transverse to the direction of propagation and so these waves are known as Transverse Electromagnetic (TEM) waves [115].

2.1.2 Periodic dielectric structures

In a periodic dielectric structure, either the electric permittivity or the magnetic permeability is modulated. It is more common in semiconductors for the electric permittivity to be modulated as the semiconductors of interest do not possess diverse values of magnetic permeability. If $\varepsilon(x)$ denotes the electric permittivity in a one-dimensionally periodic system with period a, then the electric permittivity is invariant under a one-period translation (lattice translation)

$$\varepsilon(x) = \varepsilon(x+a) \tag{2.8}$$

where

$$\varepsilon(x) = \frac{1}{a}\sum_{i=1;x=0}^{i=p;x=a}\varepsilon_i x_i \tag{2.9}$$

p being the integer number of different, homogeneous and isotropic media in one period, ε_i being the dielectric permittivity in the ith medium and x_i being the corresponding length of the ith medium.

Alternatively, the periodic function can be expanded as a Fourier series summed over the reciprocal lattice vectors, G :

$$\varepsilon(x) = \sum_{G} \varepsilon_G \exp(iGx) \tag{2.10}$$

where G = 2πm/a is the reciprocal lattice vector and m is an integer that can take any positive and negative value including zero.

The two expressions for the periodic nature of the electric permittivity (2.8 and 2.10) indicate that there are two methods for examining periodic structures, the first in real space and the second in reciprocal space. The two different implementations will be discussed in more detail in later sections.

2.1.3 Wave propagation in periodic structures

The electromagnetic wave equation in a periodic structure is very similar to that in free-space. The only difference is that account must be taken of the periodic nature of the electric permittivity, as described in the previous section. In a periodic system the electric field can also be expressed as a Fourier series summed over all the wavevector values, k, permitted by the boundary conditions, so that

$$E(x) = \sum_{k} C(k) \exp(ikx) \tag{2.11}$$

Substitution of equations 2.10 and 2.11 in the wave equation, (2.6), leads to the eigenvalue equation

$$C(k)k^2 = \omega^2 \sum_{G} \varepsilon_G C(k - G) \tag{2.12}$$

The permitted solutions of this eigenvalue equation correspond to the propagating modes, whereas the forbidden solutions correspond to the photonic bandgaps. This equation can be solved by two different methods, but only one of these, the modal approach, gives a physical insight because the propagation is described in

terms of the elementary waves (Bloch waves) of the periodic structure [117].[3] These waves have a well defined, constant direction of propagation (that of the group velocity) which represents the direction of energy transfer. It has been predicted that future applications will use the interference of these Bloch waves with each other to produce novel devices, such as for beam-steering or for filtering [118, 119].

Another instructive manner in which to consider the propagation of an electromagnetic wave through a periodic structure is to view the structure as a series of dielectric interfaces. In this instance, is is necessary to consider the interfaces between the different media of the structure. Let us consider a dielectric interface with an incident, reflected and transmitted wave as shown (Fig. 2.1). At the boundary between the two media, two conditions must be fulfilled: firstly, the tangential component of the electric fields in both media must be equal at the interface (from Gauss' law) and secondly, the tangential component of the magnetic fields in both media must also be equal at the interface. In one-dimensional structures, the second continuity equation is often written in terms of the first spatial derivative of the electric field, which is proportional to the magnetic field. The application of these boundary conditions leads to Fresnel's law of reflection, Snell's law and the definition of the Brewster angle. Moreover, the amount of light transmitted and reflectivity can be calculated, which in the case of normal incidence is found to be a simple ratio involving the two different refractive indices :

$$R = \frac{(n_1 - n_2)^2}{(n_1 + n_2)^2} \tag{2.13}$$

and in the lossless case the transmission coefficient, T, is related to the reflection coefficient, R, by :

[3] The other method of calculation is coupled mode theory.

$$T = 1 - R = \frac{4n_2}{(n_1 + n_2)^2} \tag{2.14}$$

As can be seen from equations 2.13 and 2.14, the larger the refractive index difference the larger the reflected intensity. Typically at a semiconductor-air interface, 30% of the incident light is reflected, assuming a refractive index of one for air and 3.4 for the semiconductor - a typical value for AlGaAs waveguides.

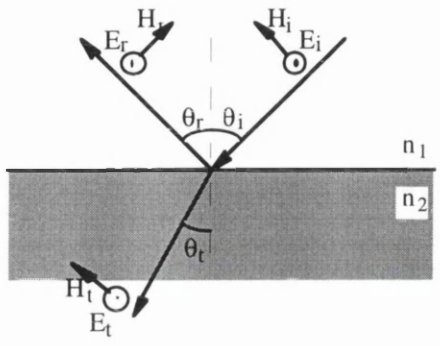

Fig. 2.1 Ray diagram of incident, reflected and transmitted wave at a dielectric interface.

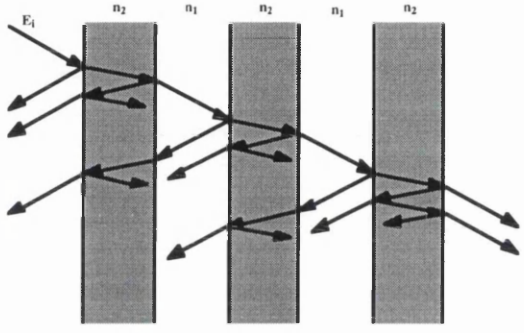

Fig. 2.2 One dimensional periodic structure consisting of a series of parallel interfaces ($n_2 > n_1$). Rays reflect some of the possible multiple ray paths.

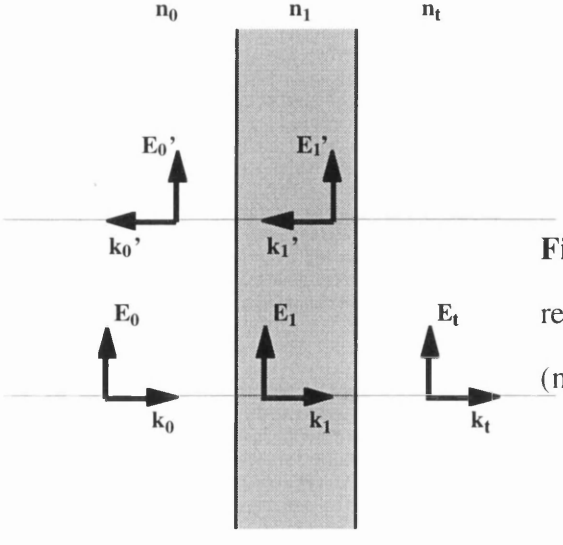

Fig. 2.3 Single dielectric layer with reflected and transmitted rays ($n_1 > n_0, n_t$).

If one now considers a 1-D periodic structure (Fig. 2.2), it can be seen that the periodic structure is simply a series of dielectric interfaces. In order to determine the properties of the whole periodic structure, a summation is made of all the effects at each interface. In the periodic case there will be many counterpropagating waves due to multiple reflection and transmission and these waves will interfere with each other. Under certain circumstances, the forward and backward propagating waves will interfere to produce a standing wave, namely a region in which there are no propagating waves. The theory of multiple layer films can be used to describe the propagation of the field through these structures [4]. The simplest possible structure is that of Fig. 2.3, where there is a single dielectric layer of length l and refractive index n_1 between two infinte media of index n_0 and n_t. After the application of the boundary conditions, the following matrix equation for the electric and magnetic fields respectively are obtained at normal incidence :

$$\begin{bmatrix} 1 \\ n_0 \end{bmatrix} + \begin{bmatrix} 1 \\ -n_0 \end{bmatrix} \frac{E_r}{E_0} = \begin{bmatrix} \cos kl & \frac{-i}{n_1} \sin kl \\ -in_1 \sin kl & \cos kl \end{bmatrix} \begin{bmatrix} 1 \\ n_t \end{bmatrix} \frac{E_t}{E_0} \tag{2.15}$$

A simplified version of this matrix equation is :

$$\begin{bmatrix} 1 \\ n_0 \end{bmatrix} + \begin{bmatrix} 1 \\ -n_0 \end{bmatrix} r = M \begin{bmatrix} 1 \\ n_t \end{bmatrix} t \tag{2.16}$$

where r is the amplitude reflection coefficient, t is the amplitude transmission coefficient and M is known as the transfer matrix. It can be shown that a similar matrix equation can be derived for a periodic structure (Fig. 2.2), but this time the transfer matrix is the product of the individual transfer matrices, that is

$$M_1 M_2 M_3 ... M_n = M = \begin{bmatrix} A & B \\ C & D \end{bmatrix} \tag{2.17}$$

Equation 2.16 can then be solved for r and t in terms of these elements to give :

$$r = \frac{An_0 + Bn_t n_0 - C - Dn_t}{An_0 + Bn_t n_0 + C + Dn_t} \tag{2.18}$$

$$t = \frac{2n_0}{An_0 + Bn_t n_0 + C + Dn_t} \tag{2.19}$$

Alternatively, in many periodic structures, such as Bragg stacks, anti- and high-reflection coatings, the Bragg condition is applicable [4]:

$$a\sin\vartheta = m\frac{\lambda}{2n} \tag{2.20}$$

where a is the period, θ is the angle from the interface normal, m is an integer number, λ is the free–space wavelength and n is the refractive index. This condition is particularly true when the grating has a small refractive index modulation (Δn~0.1). The Bragg condition corresponds to a phase shift of 2π on reflection, which means that the reflected waves from consecutive periods are in phase with each other. The simplest means to accomplish this with two different media is to make the optical thickness of each layer λ/4n (π phase shift). In some PBG structures consisting of alternating air and semiconductor regions, however, this approach is not applicable since other factors, such as diffraction and scattering losses, can prevent the use of large air regions, as would be detemined from the λ/4n condition. This criterion is particularly true for optical waveguide based PBG structures, where there is a confined optical mode incident on the semiconductor-air interface and scattering into air and into the substrate may occur.[4] In this instance, a more exact summation of the contributions from each interface must be made.

[4] There are solutions to this problem, which are guided modes but these have not been explored in this project.

All of the above theories can be applied to multi-dimensional systems as the equations describing the system are identical to the one-dimensional case provided the spatial variables are converted from 1D to multi-dimensional. In multi-dimensional systems, however, there are additional effects to be considered such as diffraction and the geometry of the periodicity, but the boundary conditions at each interface are the same as for the one-dimensional case. Therefore, much insight into many of PBG properties can be ascertained by using simpler 1D models.

2.1.4 Equivalence of photonic and electronic bandgaps

There are very strong analogies between the propagation of an electromagnetic wave and the propagation of single electrons, both in free-space and in periodic structures, if the electron-electron Coulombic interactions are ignored. Considering only the periodic case the analogy becomes very clear if the electromagnetic wave equation is recast in a different form by re-expressing the electric permittivity as :

$$\varepsilon=\varepsilon_{av}+\Delta\varepsilon \tag{2.21}$$

where ε_{av} is the average electric permittivity and $\Delta\varepsilon$ is the modulation amplitude. The wave equation can then be expressed as

$$\frac{\partial^2 E}{dz^2}+\mu\omega^2(\varepsilon_{av}+\Delta\varepsilon)E=0 \tag{2.22}$$

This equation now looks identical to the Schrödinger equation that describes the propagation of electrons [23]:

$$\frac{\hbar^2}{2m}\frac{\partial^2\Psi}{\partial x^2}+(E-V_0)\Psi=0 \tag{2.23}$$

In both equations 2.22 and 2.23, there is a term describing the free-space energy of the particles plus a term corresponding to the periodic nature of the electric permittivity and electric potential respectively. The electric permittivity, or relative refractive index, therefore, plays the role of an electromagnetic "potential" just as the Coulombic interaction between the electrons and crystal cores produces a confining electric potential. This is where the similarity ends, however, and it should be remembered that electrons are fermions and obey the Pauli exclusion principle and that the Coulombic interactions between charged particles can produce very strong potentials. On the other hand, photons are bosons and there is a high probability that bosons will occupy the same energy state. It is this property that makes many optoelectronic devices feasible, such as lasers where almost all the photons are to be found in the same energy state. It is the many similarities between the two cases, however, that allowed early theoretical advances to be made and that permitted experimental research to be focussed on the most important cases.

2.1.5 Photonic bandgap calculations

There are several ways in which the properties of photonic crystals can be calculated, each with its own merits. Theoretical calculations are simplified, compared to the electronic case, because there is not a photonic equivalent of coulombic forces so many-body interactions between electrons need not be considered. The first method is the Plane Wave Method (PWM). A general reference on the PWM for electronic band calculations is given by Cohen and Chelikowsky [120]. This method is based on the application of the Bloch Theorem to the electromagnetic modes of the structure, constructing the periodic field in terms of plane waves and then, for each allowed wavevector, calculating the allowed frequencies $\omega(k)$. It is important to note that the vector electromagnetic field must be used in calculations of three dimensional structures as the scalar

approximation does not give correct results [25-27]. However, in the 2-D case the two polarisations can be separated under certain circumstances [121], allowing the scalar wave equation to be used and much reducing the complexity of the calculation. Several different implementations of the PWM have been suggested [122, 123], some of which are faster and more accurate than others. The PWM is based on an infinite structure and, can, therefore, have some intrinsic disadvantages. An extension of the PWM, called the supercell method [124], permits the application of this method to structures that are not perfectly periodic.

A method with particular relevance for experimental comparison is the transfer matrix method (TMM) [125, 126] as it calculates both transmission and reflection and these are the properties that are measured experimentally. The periodicity of the structure means that its properties at one point in the structure are identical to the properties at the same point an integer number of periods from the reference point. A matrix can, therefore, be constructed to describe the propagation through one period and this matrix can then be multiplied as many times as are required to build up the complete structure.[5] If a defect is introduced, it is easily incorporated by including the matrix describing the propagation through this part of the structure. The TMM requires that Maxwell's equations are discretised on a mesh and the accuracy of the calculation depends on the number of points in the mesh. The approximation can result in problems, especially if there are defects in the structure, since defects can form very high-Q cavities [127] and this method may not then have sufficient spatial resolution to determine the properties of the defect.

In certain circumstances it is better to use a combination of methods, especially if it is thought that there will be small spectral features. The PWM can be used to locate the defect and then the TMM can be focused on the region of interest. This

[5] This formulism represents an extension of the method described in §2.1.3.

combined approach means that no significant feature of the behaviour will be missed and that the calculation time will be reduced.

There are other methods for PBG calculations, which include the Finite Difference Time Domain method [128] and diffraction theory [129]. FDTD is proving increasingly more of interest as it allows both the temporal and spectral properties of any structure to be determined by one set of calculations. In particular, this method is useful in calculating the quality factor of a defect in a periodic structure or a cavity [130]. The key properties of PBG structures have now been calculated in detail, but future interest will lie in the more accurate modelling of experimental results by PWM and TMM and the application of FDTD in determining both the inherent properties of PBG devices and their interaction with the surrounding media.

No matter which approach is chosen it is most common for the results to be plotted in normalised frequency units and to collate these results in what are known as gap-maps (Fig. 2.4). For each particular lattice configuration, there is a gap-map and due to the scalability of the electromagnetic wave equation one set of calculated frequencies used to construct a gap-map can be used for all materials, even though gap-maps are calculated for a particular refractive index [12].

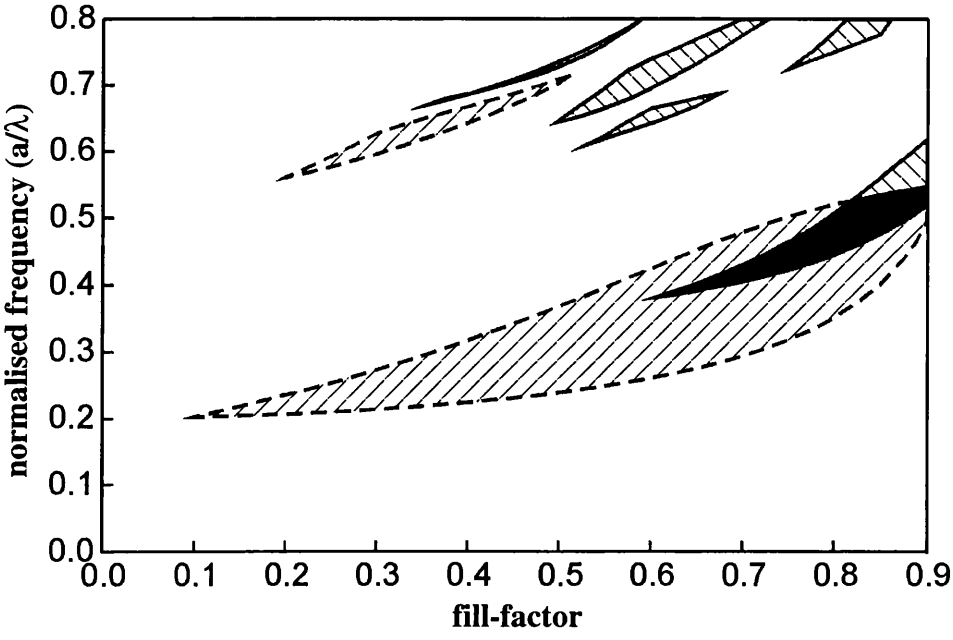

Fig. 2.4 Gap map for triangular lattice of air holes in an AlGaAs heterostructure waveguide (ε=11.0). The areas with dotted borders are the TE stopbands and the firm borders are the TM stopbands; the black shaded area is the region where the individual stopbands overlap and a complete 2D photonic bandgap exists (calculated by David Cassagne at Université de Montpellier II, France).

2.2 Optical waveguide

One of the potential applications for PBG technology is in the confinement of light. The confinement of light in one dimension within a semiconductor heterostructure, however, has been around for several decades in the form of the optical waveguide (Fig. 2.5) [131]. A typical optical waveguide consists of a central core, which has a higher refractive index than the surrounding layers and in which confined optical modes can propagate.[6]

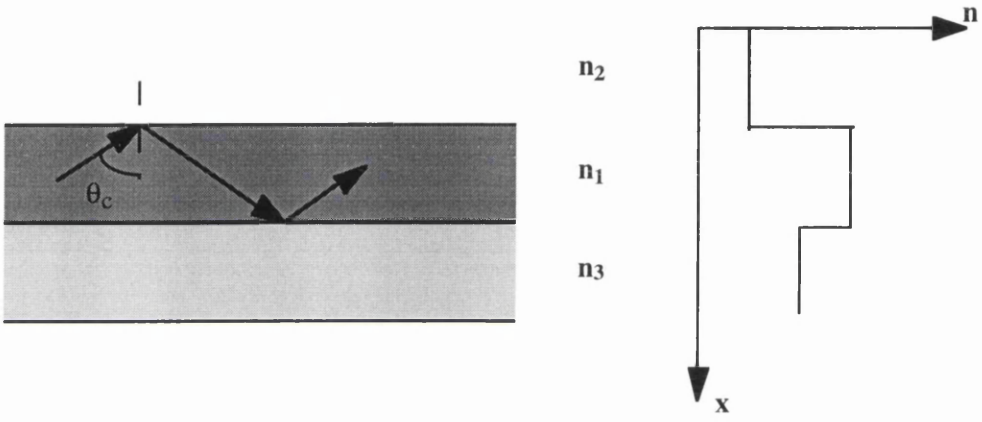

Fig. 2.5 Typical optical waveguide ($n_1>n_3>n_2$).

Let us consider a planar guide and assume that $n_1>n_3>n_2$ (Fig. 2.5). At each interface there will be reflection and transmission of the incident waves. If the incident angle is less than the critical angle, $\varphi_i<\varphi_c$, then the light will escape (radiation modes). On the other hand if the incident angle is greater than the critical angle ($\varphi_i>\varphi_c$), then light is confined within the high refractive medium due to total internal reflection. Moreover, waves experiencing total internal reflection undergo a phase shift on reflection, the magnitude of which depends on the polarisation and the refractive index difference [131]. In the ray model approach this phase shift

[6] In a way, the high refractive index core creates an electromagnetic potential similar to an electric potential in an electrical waveguide (§ 2.1.4.

means that the plane of reflection is behind the actual interface or there is a lateral translation of the ray at the real interface, an effect known as the Goos-Hänchen shift [131]. This phase shift is important when one considers the transverse modes supported by the structure. The condition for supported modes, which corresponds to the constructive interference of the rays, is given by :

$$2dkn_1 \sin\vartheta + \varphi_{1,2} + \varphi_{1,3} = 2N\pi \tag{2.24}$$

where $\varphi_{1,2}$ and $\varphi_{1,3}$ are the phase shifts between media 1 and 2, and 1 and 3 respectively and N is an integer. Due to the complex nature of the phase-shift term, this equation has to be solved numerically. An insightful manner to analyse the properties of a guided mode is to examine the dispersion relation, which once again must be solved numerically. It is most common to plot the dispersion relation for waveguides using normalised parameters:

(a) frequency parameter:

$$V = kd\sqrt{n_1^2 - n_3^2} = d\sqrt{\beta_1^2 - \beta_3^2} \tag{2.25}$$

where $\beta_{1,3}=n_{1,3}\omega/c$

(b) b parameter:

$$b = \frac{n_{eff}^2 - n_3^2}{n_1^2 - n_3^2} = \frac{\beta^2 - \beta_3^2}{\beta_1^2 - \beta_3^2} \tag{2.26}$$

(c) asymmetry parameter:

$$a = \frac{n_3^2 - n_2^2}{n_1^2 - n_3^2} \tag{2.27}$$

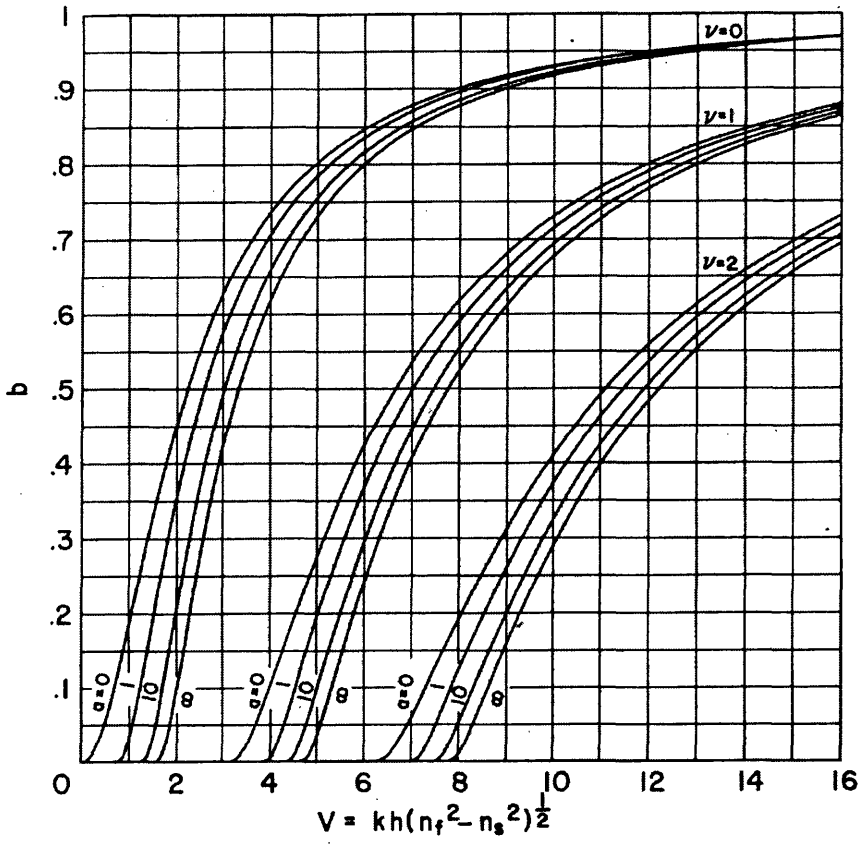

Fig. 2.6 Dispersion diagram for an optical waveguide, plotted with normalised parameters (extracted from Tamir [131]).

A plot of the dispersion relation is shown in Fig. 2.6. It is evident from the plot that the asymmetry parameter has an important effect in determining the cut-off wavelength of the waveguide. In particular, it should be noted for the lowest mode in a symmetrical waveguide (a=0) the mode does not cut-off, namely V can equal zero. However, as the asymmetry increases the cut-off wavelength decreases. It can be shown [5] that the number of modes supported in a symmetric waveguide with thickness, d, is given by :

$$M = \frac{4d}{\lambda}\sqrt{(n_1^2 - n_2^2)} \tag{2.28}$$

It can be seen from equation 2.28 that a thinner waveguide supports fewer modes at a fixed wavelength and that for semiconductor waveguides there are potentially several modes due to the large difference between n_1 and n_2. Both the thickness and refractive indices determine the field distribution of the modes. The general form for a mode in a slab waveguide is :

$$E(x,y,z) = E_t(x,y)\exp(-j\beta z) \tag{2.29}$$

$$H(x,y,z) = H_t(x,y)\exp(-j\beta z) \tag{2.30}$$

which yields a wave equation for TE modes of the form :

$$\frac{d^2E_y}{dx^2} + \left(\frac{\omega^2 n^2(x)}{c^2} - \beta^2\right)E_y = 0 \tag{2.31}$$

where β is the propagation constant; this equation is valid for all modes and for all the different media. The solutions to this equation depend on the layer being considered, but they are sinusoidal in the core guiding layer, namely :

$$E_y(x) = E_s \cos\left[\left(\frac{\omega^2 n_1^2}{c^2} - \beta^2\right)x\right] \tag{2.32}$$

for the symmetrical modes and, for the antisymmetric modes :

$$E_y(x) = E_a \sin\left[\left(\frac{\omega^2 n_1^2}{c^2} - \beta^2\right)x\right] \tag{2.33}$$

where E_s and E_a are normalised electric field amplitudes. The number of modes supported is determined approximately by the integer number of half wavelengths that fit in the waveguide, which is the same condition given in equation 2.28. In asymmetric guides, the solution in the core is given by a superposition of the sinusoidal and cosinusoidal solutions with the amplitudes being determined by the appropriate boundary conditions.

2.3 Fabry-Perot cavities

The Fabry-Perot (FP) cavity is one of the most commonly used resonator structures in semiconductor lasers [131]. This extensive use is attributable both to its theoretical simplicity and the ease with which it can be fabricated.[7] The theory of FP cavities is simply an extension of that of multiple-beam interference. Fig. 2.7 shows a typical ray trajectory that might be observed with multiple reflected and transmitted rays. In effect, it could be considered as a folded version of the periodic structures, which were discussed in §2.1.3.

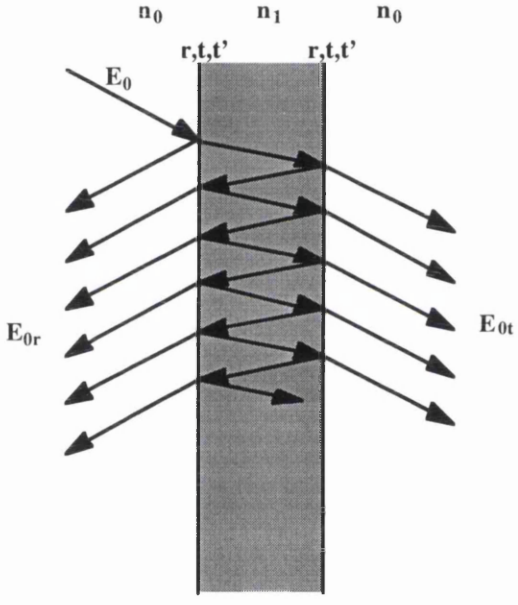

Fig. 2.7 Trajectory of a ray in a thin film giving rise to multiple-beam interference ($n_1 > n_0$).

The reflected and transmitted intensities are found by summation of all the relevant terms. There are two special cases, however, where both interesting physical effects are observed and the mathematics simplifies [4]. The first interesting case

[7] Most semiconductor laser cavities are formed by cleaved facets and in III-V semiconductors the natural cleavage planes on <100> substrates are perpendicular to each other and to the substrate. Therefore, cleaved edges define a cavity with parallel mirrors and which are normal to the direction of propagation.

is when the optical path length difference between successive rays is an integer number of wavelengths. For this condition the summation of the reflected amplitudes is:

$$E_{0r} = E_0 r - E_0 trt'(1 + r^2 + r^4 + ...) \tag{2.34}$$

In the loss-less case tt'=1-r^2 and the above equation simplifies to :

$$E_{0r} = 0 \tag{2.35}$$

This zero in the total reflected wave is due to the destructive interference of the partially reflected waves. The other interesting case corresponds to the condition for constructive interference, namely :

$$\Lambda = (m + \tfrac{1}{2})\lambda \tag{2.36}$$

where Λ is the optical path difference between one ray and the next, given by :

$$\Lambda = 2nd\cos\vartheta_t \tag{2.37}$$

In this case, the reflected electric field, which corresponds to the maximum reflectivity possible, is given by :

$$E_{0r} = \frac{2r}{(1+r^2)} E_0 \tag{2.38}$$

The more general description of the problem, which includes the phase difference between adjacent rays ($\delta = k_0\Lambda$), yields for the reflected intensity :

$$\frac{I_r}{I_i} = \frac{F\sin^2(\delta/2)}{1 + F\sin^2(\delta/2)} \tag{2.39}$$

where F is known as the coefficient of Finesse and is given by :

$$F \equiv \left(\frac{2r}{1-r^2}\right)^2 \tag{2.40}$$

The transmitted intensity, I_t, is derived from the equality, assuming no losses :

$$I_i = I_r + I_t \tag{2.41}$$

Fig. 2.8 shows a plot of equation 2.39 with a maximum in reflected intensity occuring when the phase difference, δ, is given by :

$$\delta = (2m+1)\pi \tag{2.42}$$

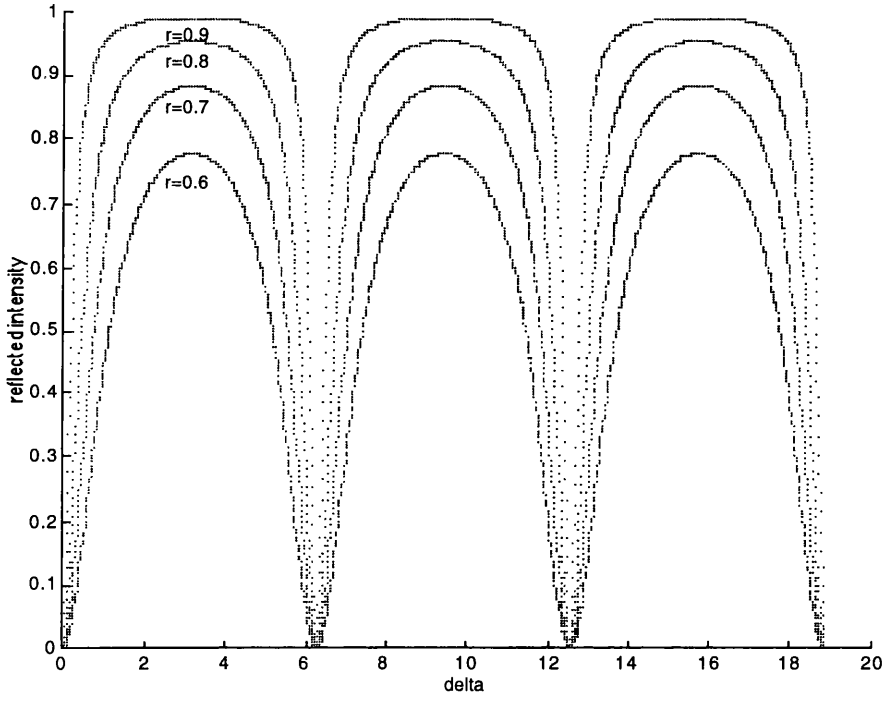

Fig. 2.8 Plot of reflected intensity for different values of finesse.

The condition for resonance in a Fabry-Perot cavity, however, corresponds to a *minimum* in the reflected intensity:

$$\delta = k_0\Lambda = (2nd).(2\pi/\lambda) = 2m\pi \tag{2.43}$$

where d is the total cavity length (i.e. $d = L_c+2L_p$, where L_c is the cavity spacing and L_p is the penetration depth, accumulated at both mirrors) and m is an integer

representing the number of half-wavelengths that fit into the cavity (also known as the cavity order). The derivation of the transmission of such a cavity yields the following results for the width of the transmission peak :

$$\Delta\lambda = \lambda / Q \tag{2.44}$$

where the quality factor, Q, is given by :

$$Q = mF \tag{2.45}$$

and F is the cavity finesse.

Therefore, the higher the reflectivity of the mirrors the higher the Q values and the more well defined the resonance wavelength. If the reflectivities of the mirrors become too high, however, very little light generated inside the cavity will be able to escape. In laser cavities, mirrors can have reflectivities as high as 99.99%, but the mirror reflectivities required depend also on the maximum gain in the media.

2.4 Conclusions

The close similarities between the theory of photonic bandgap structures and many other areas of physics have allowed the quick comprehension of this new field of research. Many of the basic photonic bandgap effects can be determined from much simpler models, provided care is taken in the application of these theories. However, many of the novel effects in photonic crystals will require a more detailed analysis of the specific structures.

3. Device Fabrication

Naturally occuring photonic crystals (PCs), such as opal [56] and butterfly wings [132], are rare and are not found in the materials important in optoelectronic devices, so almost all PCs have to be engineered. This situation offers both advantages and disadvantages, the advantages including accurate design of the structure properties and the possibility of fabricating these structures in specific materials. The majority of the engineering difficulty associated with PBG structures, however, is in their fabrication, particularly in the optical regime, where sub-micron periods are required. At optical and near-infrared wavelengths, it is very difficult to fabricate 3-dimensional PBG structures in semiconductors. Therefore, much of the work has focussed on 2-dimensional or quasi-3D structures, namely in-plane periodic structures fabricated in an optical waveguide.

There are many potential materials in which to engineer 2D PBG structures, such as GaAs, InP and silicon. The growth (or deposition) process varies for these materials, but the definition of the PBG structures in the grown material is essentially identical, regardless of which particular semiconductor is used. The key stages in the fabrication process are pattern definition or lithography and pattern transfer. These two stages can involve several constituent stages and it is these many process steps that complicate the fabrication process. Fig. 3.1 shows the fabrication process for a PBG structure and also indicates more clearly the individual steps that constitute the fabrication process.

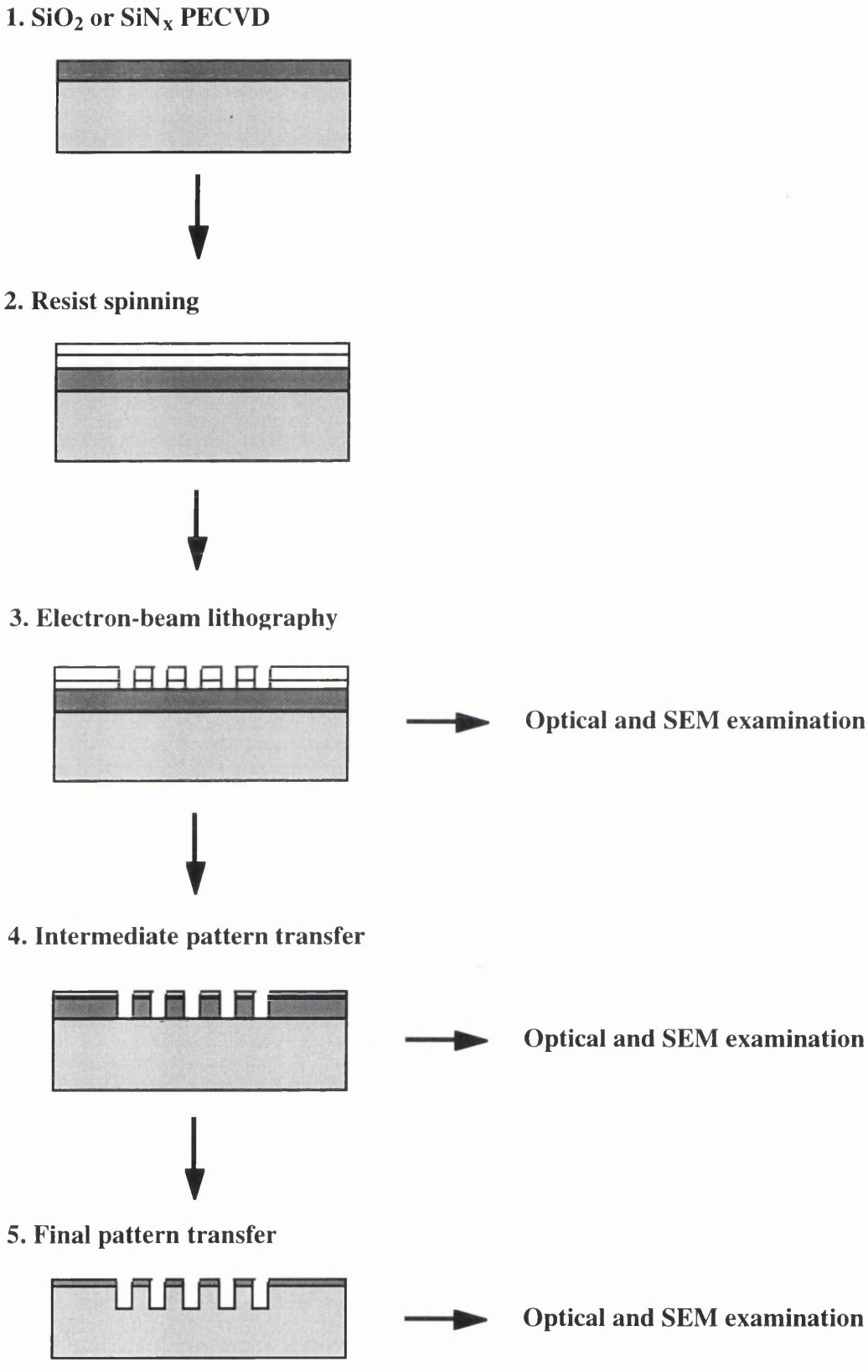

Fig. 3.1 Fabrication process for photonic bandgap structures.

3.1 Lithography

Lithography is essentially the writing or generation of the desired pattern in a material, usually a polymer.[8] There are many different methods of pattern generation, but for structures with photonic bandgaps at near-infrared wavelengths the currently viable techniques are X-ray lithography (XRL) [133], electron-beam lithography (EBL) [55], optical lithography and holography [134]. Holography is a well established technique for generating periodic features in polymers and has been used successfully in the fabrication of 2D PBG structures. The limitation of holography, however, is the difficulty in introducing intentional defects into the regular lattice, particularly at the sub-micron level. Optical lithography is currently capable of fabricating most PBG structures, as 193 nm lithography is already been used in industry. This option, however, was not available to me. XRL has the advantage that it is a parallel process, namely the whole pattern can be generated simultaneously after the mask has been fabricated. However, it is the production of a durable and reliable mask that has given problems in this field for many years. Moreover, if the design needs to be changed then a new mask has to be fabricated every time. On the other hand, EBL is a serial process with each part of the pattern written sequentially, and so it is time consuming. However, due to the need to generate the pattern every time, it is a very useful technique, particularly at the device development stage as it does not require the fabrication of a mask for every design change. Moreover, there is currently much research effort investigating the possibility of using EBL in a more parallel manner [135-137] and the ability to reuse a pattern more than one time [138-141]. These research activities should maximise the capacity of this technique and offer a more attractive package, especially considering the expense of an electron-beam lithographic system. Electron-beam lithography has been used exclusively in this project.

[8] Lithography comes from two two Greek words, ληθοσ (stone) and γραφω (to write), and was used to mean the imprint of ink into porous stone for the transfer of patterns. Its meaning has been extended to mean the writing of a pattern in almost any material.

3.1.1 Pattern design

Electron-beam lithography, as explained above, is a serial process, since a focussed spot is used as the exposure mechanism. Consequently, a great deal of the information that is requred to define any pattern is the binary series detailing whether the electron beam should be blanked or not. The method used here to generate the pattern is a commercial CAD package called WaveMaker (WAM) that generates a standard format gdsii file. The advantage of this approach is that the patterns can be observed visually, which is particularly useful when designing more complex structures such as those involving defects. The two key non-standard parameters that must be set in WAM for the purpose of PBG structures are, firstly, the number of points which define an arc (arcpts) and the resolution with which the points and vertices are defined (res). The resolution is set to 1 nm, which is below the resolution with which the machine can position itself (5 nm). Therefore, no serious errors in the generation of the pattern will arise due to the vertex storage mesh size.

The reason why the number of arc points must be defined is not a limitation of the WAM package itself, but relates to the way in which the next piece of software (CATS) processes the output file from WAM. Specifically, it is memory considerations which restrict the number of arc points that can be used.[9] Fig. 3.2 illustrates the problem. The value to which arcpts is set defines the number of trapezia into which a circle is divided - for 12 arcpts there are 6 trapezia, whereas for 16 arcpts there are 8 trapezia. The maximum number of trapezia with which CATS can deal at any one time is around 900,000. This means that the maximum number of circles with 12 arcpts is 150 000, which, assuming a square lattice with 200 nm period, equates to an area of 77 μm x 77 μm. If patterns with more

[9]Another consideration is the resolution of the lithographic process: a certain number of arcpts is required to accurately reproduce the structure, but beyond this level no significant improvement in the definition of the resist features is observed. This level of accuracy is a function of the resist used and the development conditions.

trapezia are required then the pattern is divided into blocks, each of which are fractionated separately and realigned during exposure. CATS also sets the resolution into which the patterns are to be divided, like a mesh size. This square mesh is overlaid on the pattern and each square is assigned a binary value. The value of the resolution depends on the features sizes being written: for small feature sizes, one can use a nominal resolution as small as 5 nm, the smallest possible allowed by the machine, whereas for larger features one can tolerate a courser mesh.

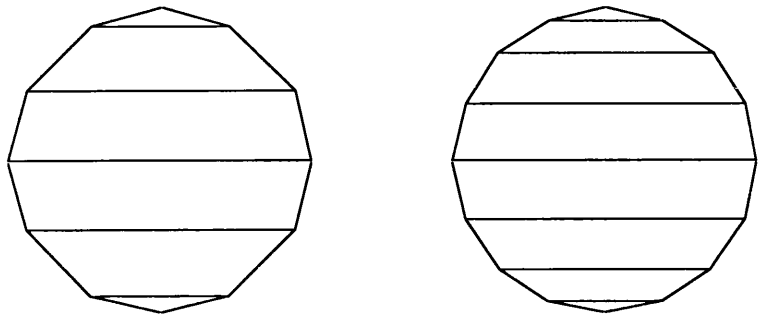

Fig. 3.2 Schematic illustrating the dependence of the number of vertices and the number of trapezia after fractionation.

The output from CATS is a set of files which include the pattern file and the data file which is used by the final piece of software package (bwl). This package sets out the pattern as it is to be written on the sample, assigns the dose to each pattern, specifies the positioning of patterns, the number of copies to be written and also the spot size with which the patterns are to be written. The spot size is the degree to which the Gaussian electron beam is to be focussed and is chosen in relation to the beam step size; in most instances the beam step-size is set equal to the resolution with which the pattern file was fractionated. A general rule of thumb is that the step size should be at least twice the resolution, otherwise the resolution of the pattern file could be lost at the lithography stage. The method for dose determination was an exposure test, namely to write the desired pattern at a series

of different doses and then examine the patterns afterwards to determine the correct dose. The final parameter that needs to be considered, apart from the actual layout of the patterns on the sample, is the interval between calibrations of the machine. The machine needs to be calibrated in order to maintain the beam current at the correct level, to check the writing frequency, the drift of the stage onto which the sample is mounted and other necessary measurements and corrections. The calibration procedure, however, requires the movement of the stage and can result in patterns being misaligned with respect to each other if written before and after calibration respectively . These errors are of particular concern in the fabrication of PBG structures because they generate undesired defects. As a result, I usually set the calibration interval to higher than the total writing time for the sample and, in this way, avoided major misalignments. This strategy is acceptable as most job times are of the order of two to three hours, in which time the assumption that the frequency and beam current have not drifted is reasonable in practice.

3.1.2 Electron-beam lithography

The first stage is the sample preparation, which involves the cleaning of the semiconductor sample, pre-cleaved to the correct size, in organic solvents with ultrasonic agitation. A polymer resist, polymethylmethacrylate (PMMA), which is sensitive to electrons is spun onto the samples. I have used two different types of PMMA in my experiments, the first is Elvacite (Elv) with an average molecular weight of 350,000 and the second is Aldrich (Ald), average molecular weight of 120,000.[10] These resists come dissolved in o–xylene or chlorobenzene in different concentrations, so that different film thicknesses are obtained. Commonly, I used 4% Elv (4% by weight of Elv dissolved in o-xylene) and each layer was spun on at 5,000 rpm for 60 seconds. The sample was then baked in an oven at 180 °C for

[10] Molecular weight is the weight of the polymer chains and is directly related to the degree of polmerisations and average chain length. Lower molecular weight polymers have a higher senstivity to high electron energy bombardment due to the shorter average chain length.

5 minutes, this time being sufficient to drive off the solvent. Generally, two layers of resist are used as this reduces the pin-holing that is sometimes observed in resists and which can degrade pattern definition and the properties of the resist film; two layers also provide a thicker and better mask for subsequent processing. The samples were exposed in the Leica EBPG-HR5 electron-beam lithographic system at an acceleration voltage of 50 kV.

I developed the samples in a mixture of methylisobutylketone (MIBK) and IPA in the ratio of 1:2.5 for 30 seconds, then rinsed them in IPA and blew them dry. I then examined the patterns in the optical microscope. As an example, a resist pattern sputter-coated with Pd:Au is shown in Fig. 3.3 below.

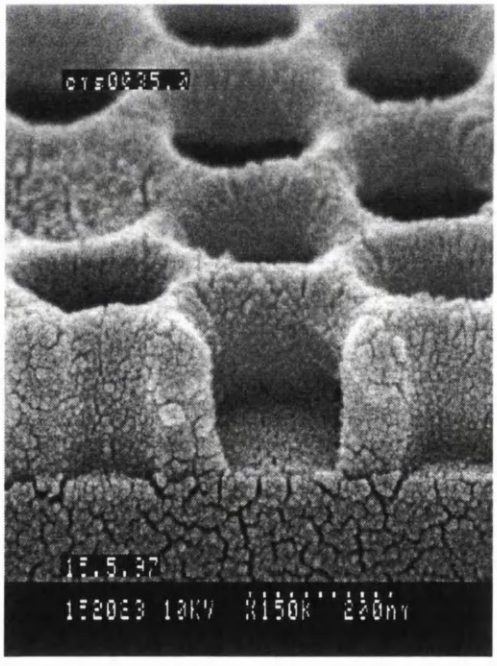

Fig. 3.3 Cross-sectional SEM micrograph of 2D PBG structures in PMMA.

3.2 Pattern transfer

Although it is possible to use electron-beam exposure to write patterns directly in semiconductors, the doses required are several orders of magnitude larger than those required to expose PMMA [142]. The use of PMMA, therefore, allows quicker pattern generation, which reduces some of the potential problems associated with EBL, but it also means that the resist features have to be transferred from the PMMA into the desired material. For the purpose of PBG structures, it is necessary to have a high fidelity pattern transfer process, which maintains the nanometre size features and which transfers the features vertically from one material to another. Generally, this pattern transfer approach requires the use of plasma processing and, in particular, reactive-ion etching. However, there are severe limitations to pattern transfer, particularly the resilience of the mask that is being used to transfer the pattern to another material. In fact, PMMA is not a very good mask in RIE processes because it erodes quickly, which limits the etching time and maximum achievable etch depth. The mask erosion also limits the definition of the features. For this reason an intermediate pattern transfer layer has been included. Generally, this intermediate layer is a thin dielectric film, either silicon dioxide (SiO_2) or silicon nitride (SiN_x) deposited by plasma enhanced chemical vapour deposition (PECVD). There is, therefore, a need to firstly transfer the features from PMMA to an intermediate layer and then to the semiconductor, as shown in Fig. 3.1 above.

3.2.1 Deposition of dielectric films

The dielectric films used, silicon dioxide (SiO_2) and silicon nitride (SiN_x), are deposited using Plasma Enhanced Chemical Vapour Deposition (PECVD) [143]. PECVD, as the name suggests, involves the use of a plasma, which is generated in this instance by a radio-frequency (RF) discharge. The properties of the deposited

film are controlled by the total and relative gas flows, chamber pressure, RF power and substrate temperature. The conditions for the deposition of the films used, however, are standardised in our department and so this complex subject will not be explored further. The general composition of the film is determined by the precursor gases. Specifically, for SiN_x, silane and ammonia are used, with the key plasma reaction between these gases forming the molecule tetra-aminosilane and hydrogen [143]. These molecules eventually deposit on the surface and neighbouring molecules condense to leave a silicon nitride film. In the case of SiO_2, the precursor gases are silane, nitrogen and nitrous oxide [143].

3.2.2 Transfer of features from PMMA to SiO_2 and SiN_x

The process for pattern transfer from PMMA to SiO_2 and SiN_x uses the same RIE process. Fluorine-based gases are used since fluorine chemically reacts with the silicon in the dielectric film to form SiF_4 [143], which is removed by ion bombardment, thereby etching the dielectric film. The fabrication of PBG structures requires vertical pattern transfer, which is best provided by CHF_3 (Fig. 3.4); an alternative is C_2F_6, although the etch rate of the PMMA in a C_2F_6 plasma is greater than for CHF_3 [112], which reduces the thickness of the dielectric layer that can be etched.

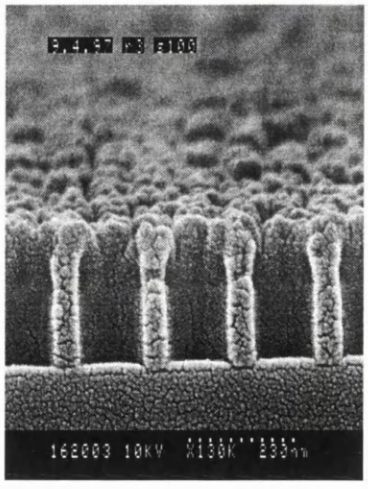

Fig. 3.4 SEM micrograph showing profile of 2D PBG structure in an 150 nm thick SiO_2 layer.

3.2.3 Pattern transfer to GaAs/AlGaAs

GaAs is usually etched with chlorine, either as molecular chlorine [144], or in a molecule [145-147], which can be dissociated by the applied RF field. Throughout this project I have used the gas silicon tetrachloride ($SiCl_4$). The principal gas phase reaction is

$$SiCl_4 \rightarrow SiCl_{4-x} + Cl_x$$

where generally x=1 or 2, with the level of dissociation being determined by the specific conditions (power, flow and pressure) in the reactor. At low power, flows and pressures the most abundant species is *molecular* chlorine (Cl_2), which etches GaAs, but does not etch AlGaAs [147]. At higher powers the density of *atomic* chlorine (Cl) in the plasma increases, as does the etch rate of AlGaAs [148].

In RIE, the chemical reactions - gas-phase and surface - are not the only contributions to the etching mechanism. In capacitively-coupled RIE machines there is also a contribution from the self-induced bias, which is a consquence of the condition for the electron and ion current densities incident on the electrodes to be equal. The induced bias is a function of the operating pressure and applied RF power and accelerates the ions across the plasma sheath onto the bottom powered electrode and the sample (Fig. 3.5). The ions incident on the sample can enhance the etch rate by physical sputtering, the mechanism which is the key in producing anisotropic features. Therefore RIE should be considered as a form of ion-assisted chemical etching.

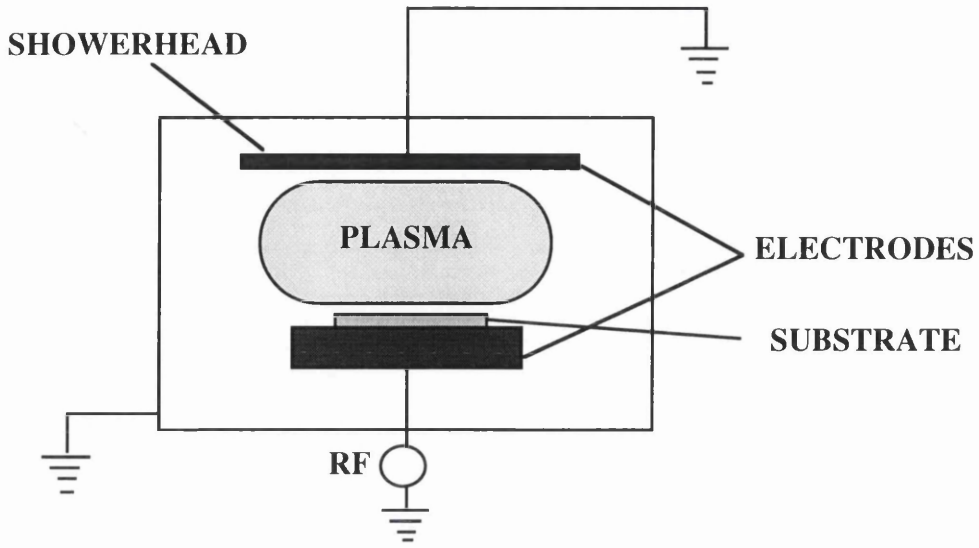

Fig. 3.5 Schematic of a typical reactive-ion etching chamber.

In the fabrication of PBG structures, where highly anisotropic features are normally required, then a large applied RF power is used. High powers ensure that the plasma is well dissociated, thereby ensuring that there is enough atomic chlorine present in the plasma and that the self-induced bias is sufficiently high to provide the necessary ion bombardment for anisotropic pattern transfer. High anisotropy can be achieved with $SiCl_4$ alone (Fig. 3.6), but it can be further increased by the addition of small quantities of oxygen. The addition of small quantities of O_2 to the plasma can produce a significant change in the gas phase reactions [149]:

$$SiCl_4 + O_2 \rightarrow SiO_2 + Cl_x$$

The increased dissociation of the plasma increases the etch rate of both GaAs and AlGaAs from that for use only of $SiCl_4$. Moreover, the deposition of SiO_2 on the side-walls of the etched features protects them from attack by ions with a transverse momentum or from ion recoil (Fig. 3.7). The addition of small flows of oxygen allows highly anisotropic pattern transfer (Fig. 3.8).

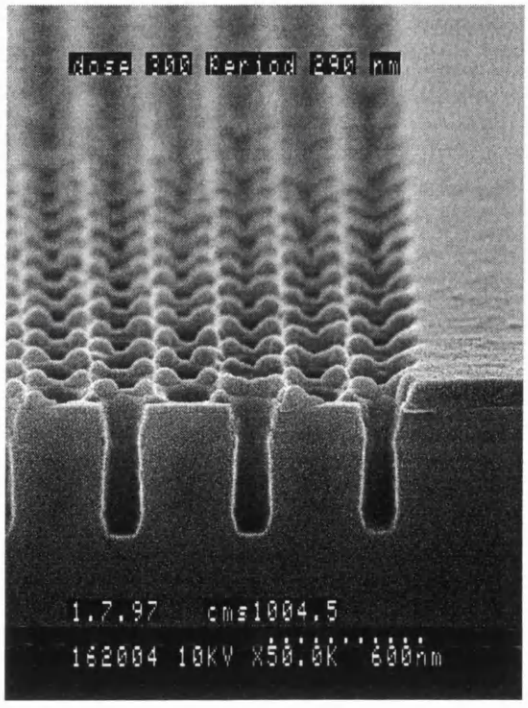

Fig. 3.6 SEM micrograph of 2D PBG structure in AlGaAs fabricated using $SiCl_4$ only.

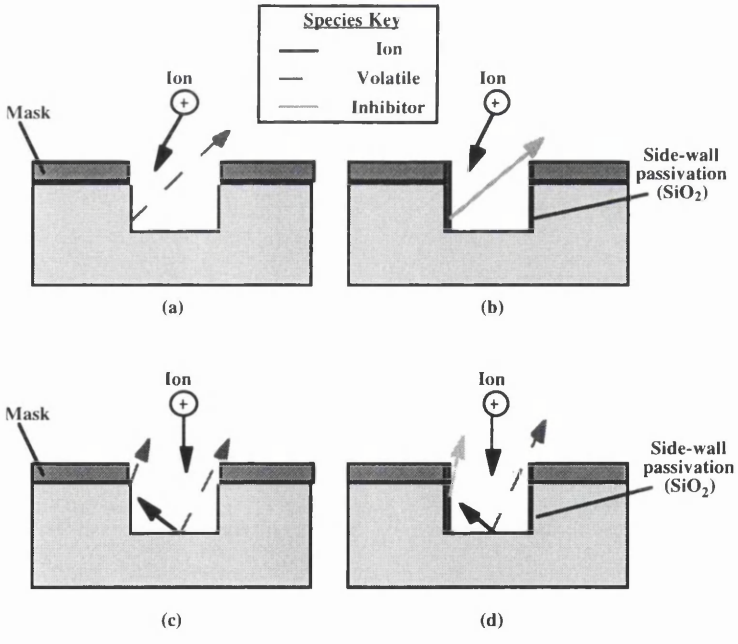

Fig. 3.7 Schematic of the effect of ion-recoil on the sidewalls of features during etching. In $SiCl_4$ the side-wall can be attacked if there is a transverse ion momentum (a) or if a vertical ion recoils into the sidewall (c). In $SiCl_4/O_2$ sidewall passivation (b), which gives preferential etching at the bottom of the features (d).

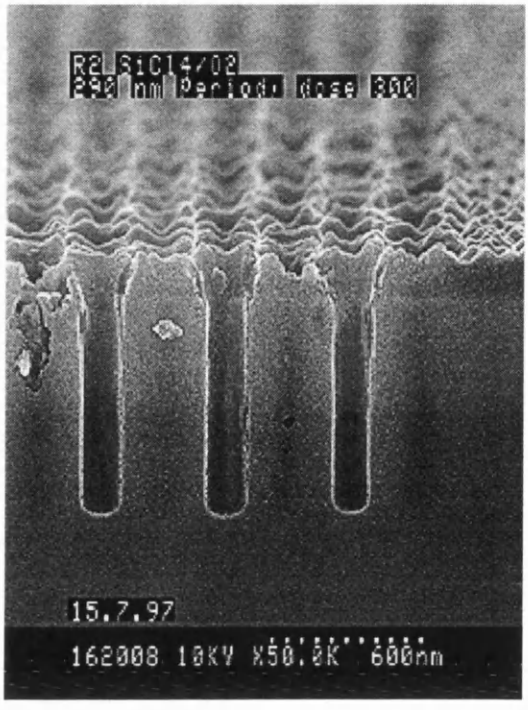

Fig. 3.8 SEM micrograph of 2D PBG structures in AlGaAs etched in $SiCl_4/O_2$ with improved side-wall verticality.

3.2.4 Transfer of features to InP-based materials

Two-dimensional PBG pillars have also been fabricated in InP materials [150, 151], but the etching of PBG structures in InP-based materials is much more complex, particularly as the choice of etching chemistry is not as clear cut as for GaAs-based materials. The most commonly used chemistry is that of CH_4/H_2. CH_4/H_2, however, has many disadvantages, such as hydrogen bombardment of the sample which leads to passivation of donors and the presence of polymer in the chamber. The etching process relies largely on the formation of organometallic products, which are not highly volatile at room temperature. The low volatility of the organo-metallics means that ion-bombardment is important to assist the removal of these products and to etch the semiconductor. However, as the power is increased, the self-induced bias goes up and the dissociation of the plasma increases, which produces more hydrocarbon polymer. The presence of this polymer can be extremely useful as it protects the mask from attack, but for the sub-micron, densely packed features, which are typical for 2D PBG structures, the

polymer deposition protects not only the mask but also the semiconductor from etching. Fig. 3.9a shows a 1D grating with 1 μm period and 100 nm slits etched in InAlGaAs with CH_4/H_2, but a 2D PBG structure (Fig. 3.9b) etched at the same time did not transfer to the semiconductor due to polymer deposition. It is possible to fabricate 2-D PBG structures in InP using CH_4/H_2, but I found the lower limit for etching is around 500 nm period (Fig. 3.10); Fig. 3.11 shows a 2D PBG structure in InP with a smaller period and bell-shaped etched features. The shape of the features indicates the strong sputtering component to the etching and the lack of chemical etching. Unfortunately, for many applications a period of 500 nm is too large and so an alternative solution needs to be found.

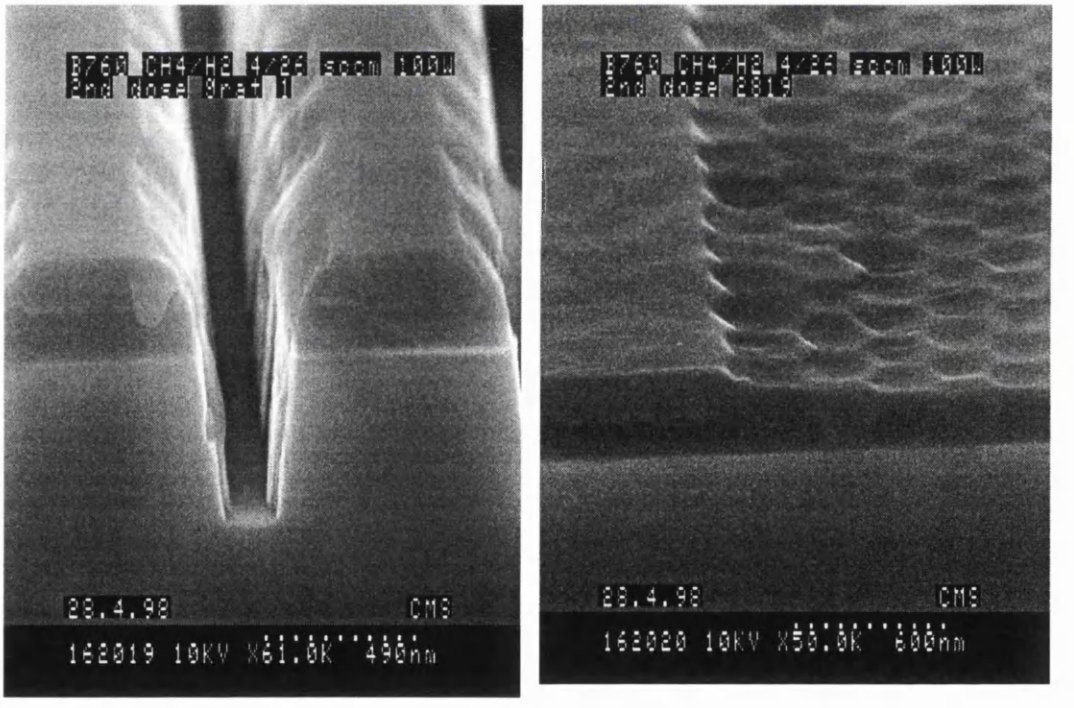

Fig. 3.9 a) 1D grating in InAlGaAs etched in CH_4/H_2 and b) 2D PBG structures etched at the same time.

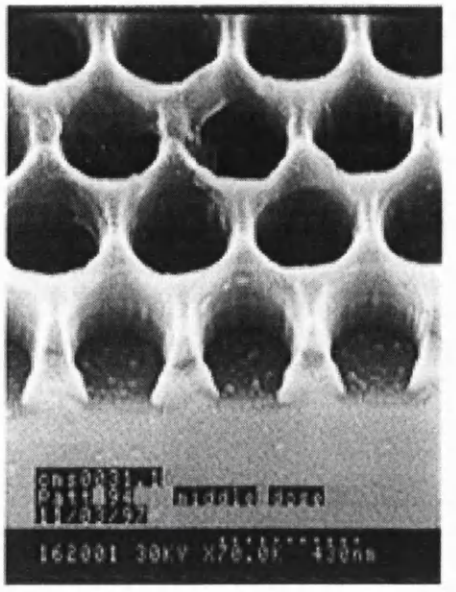

Fig. 3.10 Second order 2D PBG structures etched in InP using CH_4/H_2.

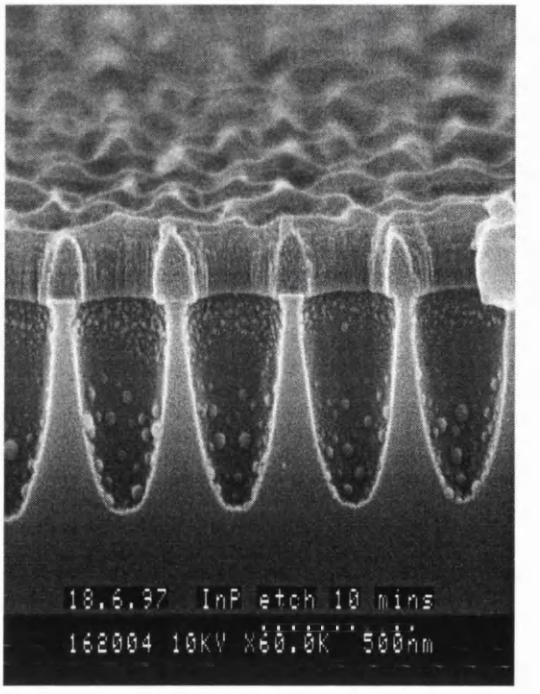

Fig. 3.11 2D PBG structure etched in InP using CH_4/H_2; period is 340 nm.

The problem of excessive polymer formation and deposition can be overcome in certain instances by the addition of small flows of oxygen. The oxygen in the plasma reacts preferentially with the carbon in the gas phase to produce carbon monoxide. The production of this gas reduces the quantity of polymer present and alleviates some of the fabrication problems associated with 2D PBG structures. However, this approach is not possible when either InAlAs or InAlGaAs is being used since the oxygen in the plasma will react with the Al in the heterostructure to form an aluminium oxide, which will stop any further etching (Fig. 3.12).

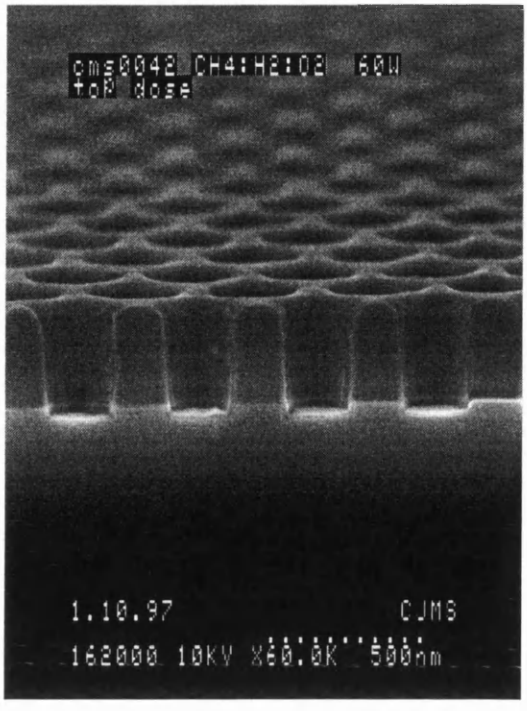

Fig. 3.12 2D PBG structure in InAlGaAs etched in $CH_4/H_2/O_2$. There is no polymer deposition, but only the InGaAs cap layer has been etched.

A commonly used alternative etch chemistry is based on chlorine. However, InCl is not volatile at room temperature even with ion bombardment, and therefore requires the use of high density plasmas (ECR or ICP) [144, 152] and/or elevated substrate temperatures [153]. Unfortunately, it has not been possible during this project to explore these avenues and so no InP-based PBG devices have been fabricated.

3.3 Conclusions

The application of electron-beam lithography and pattern transfer processes, based on reactive-ion etching, to the fabrication of photonic bandgap structures has proved very successful. Good knowledge of the electron-beam lithography software proves useful and there are sufficient tricks that one can play to produce high quality features. The transfer of these sub-micron features to InP-based materials has proven difficult, but has been very successful in the GaAs/AlGaAs material system where highly vertical etching has allowed the fabrication of PBG device structures.

4. Fabrication process developments

The fabrication of PBG structures in GaAs/AlGaAs materials is relatively easy when compared to the attempts at fabrication of these densely packed features in InP-based materials. Due to the difficulties in fabrication of InP PBG structures, the whole of the fabrication process was examined in order to maximise the quality of each individual stage and to look for possible alternative approaches. This detailed characterisation of the complete fabrication process has led to improvements in pattern transfer from PMMA to silica and silicon nitride. Moreover, improved dry-etching of AlGaAs has made the fabrication of PBG structures easier. Two possible alternative intermediate pattern transfer masks have been identified, one of which allows the fabrication of nanometre features with aspect-ratios greater than 10.

4.1 PMMA as an initial pattern transfer mask

4.1.1 Introduction

The low resilience that PMMA exhibits in a RIE plasma ultimately limits the maximum etch depth that can be achieved in any dry-etch process. In response to this limitation much research has been carried out worldwide to improve the resistivity and resilience of EBL resists including PMMA, while balancing this need against improved sensitivity to high-energy electrons [154]. These efforts have been successful in many ways, but for very high resolution patterns, "standard" PMMA is still commonly used. Rather than changing the type of resist, however, it has been discovered that the configuration of the RIE machine can be altered to decrease the etch rate of PMMA and to increase the selectivity between PMMA and thin films, such as SiN_x and titanium [112].

Two RIE machines were used in this study, which allowed the comparison of the etching of PMMA under nominally similar conditions in two different machines. The first machine was an Oxford Plasma Technology System 100 RIE machine (S100), while the second was an Oxford Plasma Technology RIE80 machine (RIE80). Both machines are capacitively-coupled parallel plate reactors, although the S100 is evacuated by a turbomolecular pump and has an integrated loadlock. The etching process was monitored using real-time interferometry with a laser wavelength of 679 nm. The final etch depth was measured using a DekTak surface profilometer. Optical Emission Spectroscopy data were obtained using an EG&G Applied Research OMA III.

4.1.2 Comparison of different resists in S100 machine

Firstly, unpatterned samples coated with the different PMMA resists, Elv and Ald, were etched in the S100 machine using the precursor gas CHF_3. Similar etch rates were obtained for Elv and Ald PMMA, 15 nm/min and 17 nm/min respectively. These etch rates are sufficiently close that it can be considered that differences in molecular weight do not have any effect on the PMMA etch rate. As a result of this finding, 4% Elv (4% weight of Elv in xylene) was used for the rest of the experiments as it had the slightly lower etch rate.

4.1.3 Comparison of PMMA etch rates in different plasmas in S100 machine

The etching of samples coated with PMMA, but left unpatterned, in different fluorine-, chlorine- and bromine-based plasmas was investigated in the S100 machine. The conditions used in these tests had been optimised previously for pattern transfer to thin dielectric or metal films (Table 4.1).

Precursor gas	etch pressure (mT)	DC bias (-V)	flow (sccm)	etch rate (nm/min)
CHF_3	12	260	30	15
C_2F_6	12	320	20	80
SF_6	12	260	20	133
$SiCl_4$	7	330	15	50
HBr	4	350	15	100
Ar	12	270	20	40

Table 4.1 Etch conditions and etch rates of 4% Elvacite in different plasmas in the S100 machine.

The first interesting result observed was the low etch rate for 4% Elv in a CHF_3 plasma, both in absolute terms and also when compared to the etch rates in other fluorine containing gases at similar biases. Sputtering, which will be significant at the biases observed, cannot explain the difference in etch rates, as the etch rate of PMMA in an argon plasma at a similar bias is 40 nm/min.

Gas	Peak intensity (a.u.)
CHF_3	1704
C_2F_6	2616
SF_6	16383

Table 4.2 Optical Emission Spectroscopy peaks of the 703.7 nm fluorine line in CHF_3, C_2F_6 and SF_6 plasmas at the conditions detailed in Table 4.1.

One difference between the plasmas investigated is the chemical component of etching - the atomic fluorine density. Optical Emission Spectroscopy measurements on the 703.7 nm fluorine line indicate that the free fluorine concentration in the CHF_3 plasma is considerably lower than for the other gases (Table 4.2). This lower atomic fluorine density in the CHF_3 plasma is due to the

presence of the hydrogen in the precursor gas: the molecule HF is formed in the gas phase and is not easily dissociated due to its high-binding energy (5.91 eV) [155]. This reduction in fluorine density will have an important effect on the etch rate of the PMMA as it affects the formation rate of volatile compounds, e.g. CF_4 [156], that have formed at the PMMA surface. An alternative mechanism that would assist in lowering the etch rate of PMMA in a CHF_3 plasma would be the formation of fluoropolymer [143]. These results are discussed in more detail in section 4.1.4.

The second interesting result was the lower etch rate of PMMA in a $SiCl_4$ plasma. The etch rate of PMMA in a $SiCl_4$ plasma in the S100 machine (50 nm/min) is lower than in the RIE80 machine operated under similar bias conditions (PMMA etch rate of 100 nm/min). One main difference between these machines is the lack of a turbo pump and loadlock on the RIE80 machine, which results in a higher partial pressure of oxygen in the chamber. It is known indirectly that the oxygen concentration in the RIE80 is higher than in the S100 [148] and also that the addition of very small oxygen flows (< 0.1 sccm) has been shown to increase the etch rate of GaAs through an increased density of both Cl and Cl_2 ions [147]. The difference in partial pressure in the two machines has not been directly quantified, but the indirectly known difference in residual oxygen level will contribute to some degree to quicker etching of PMMA.[11] These differences are discussed below in more detail, following a more detailed investigation into CHF_3 etching of PMMA in the S100 machine.

[11] The differences are known qualitatively because the selective process in the RIE80 machine, which relies on the oxygen background in the machine, cannot be reproduced in the S100 machine at similar conditions.

4.1.4 Etching of PMMA in CHF_3

The low etch rate of PMMA in CHF_3 was of particular interest and so the etch rate of unpatterned PMMA and PECVD SiN_x in a CHF_3 plasma was measured at different biases in the S100 machine (Fig. 4.1a) and the selectivity of SiN_x with respect to PMMA was calculated (Fig. 4.1b). Let us consider the SiN_x etch rate first of all, as it will help explain the more complicated etching of PMMA. The sputtering contribution to any etching levels off at higher power densities, as is shown in Fig. 4.2 which shows the percentage aluminium, as measured by XPS,[12] sputtered from the electrode onto the PMMA surface. Therefore, the almost linear increase in the SiN_x etch rate is attributable to a superlinear increase in the fluorine density; it is known that the etch rate of SiN_x is increased when there is both an abundance of atomic fluorine and sufficiently energetic ion bombardment, as is observed here at the highest power densities [143].

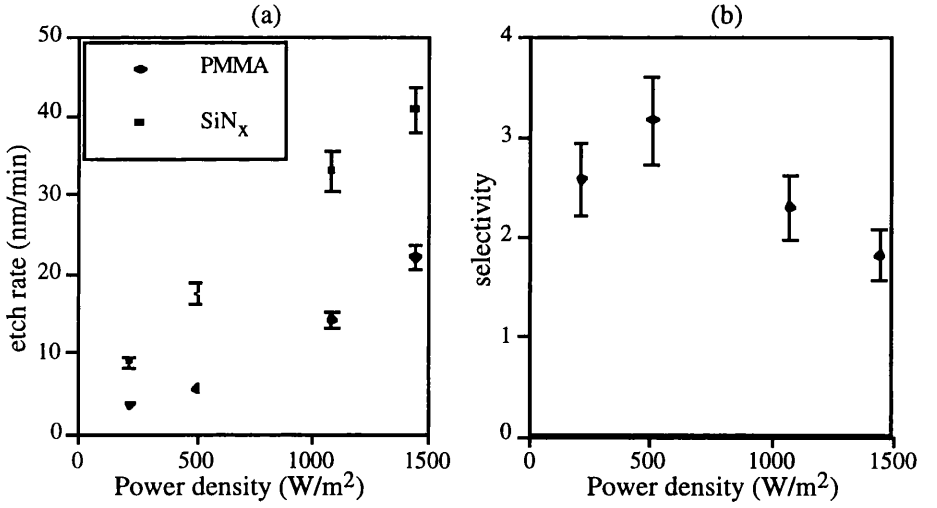

Fig. 4.1 a) Etch rate of unpatterned PMMA and SiN_x in the S100 machine as a function of the RF power density; b) calculated selectivity of SiN_x to PMMA for the S100 machine.

[12] XPS measurements were performed by Loughborough Consultants.

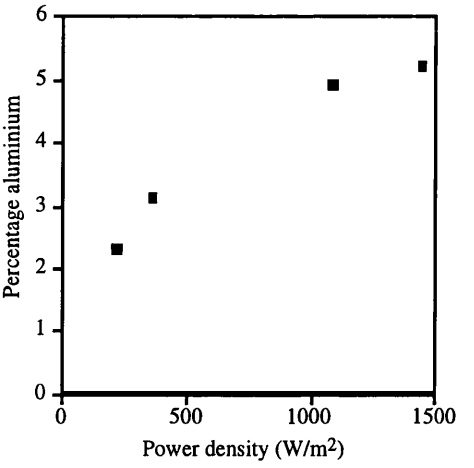

Fig. 4.2 XPS determined aluminium percentage sputtered from the electrode onto the PMMA surface in a CHF_3 plasma, allowing an indirect determination of the sputtering contribution.

Power density (W/m^2)	C/F ratio
0	∞
216	1.9
504	1.8
1079	1.5
1439	1.6

Table 4.3 XPS quantification of the carbon to fluorine ratio at the surface of 4% Elvacite at different power densities.

The explanation of the etch mechanism for PMMA is more complicated, as can be seen from the two regimes of etching (above and below 500 W/m^2), shown in Fig. 4.1a. In part this is due to the chemical reactions, both gas phase and surface, which make direct interpretation of etch rate data more difficult. XPS measurements made of both processed and unprocessed 4% Elv layers (Table 4.3) show that the exposure of the film to a CHF_3 plasma results in either the

incorporation of fluorine into the polymer matrix or fluoropolymer deposition from the plasma. There is evidence of CF_2 and CF_3 molecules in the etched PMMA films, particularly at the higher power densities, and only slight evidence of CF bonds for the highest power densities (Fig. 4.3). These results agree with the previous interpretation of those factors affecting the SiN_x etch rate, namely a greater dissociation of the plasma and an increase in the atomic fluorine density at higher powers. CF_2 and CF_3 peaks are also observed at low powers, supporting the idea of fluoropolymer deposition (Fig. 4.4), which has been observed in the etching of SiO_2 in fluorocarbon plasmas using photoresist masks [143].

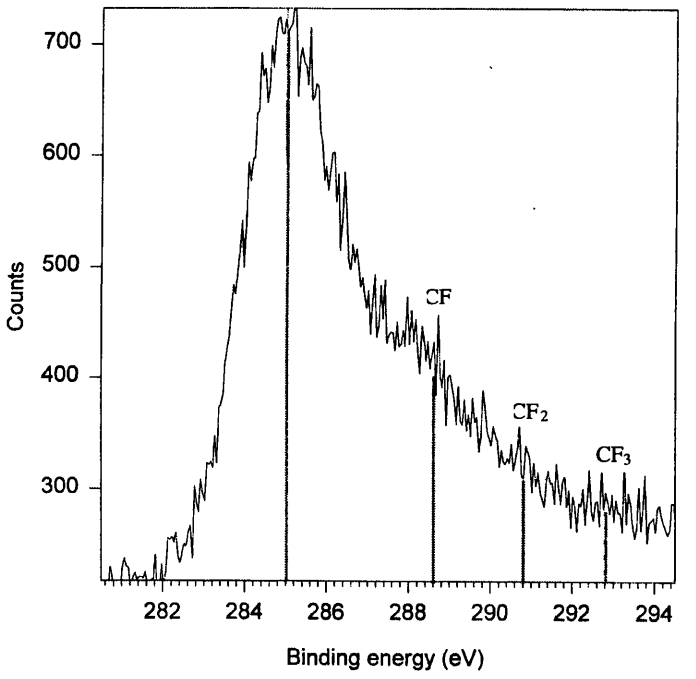

Fig. 4.3 High resolution XPS spectrum of 4% Elvacite etched in CHF_3 at 1439 W/m^2 in the S100 machine.

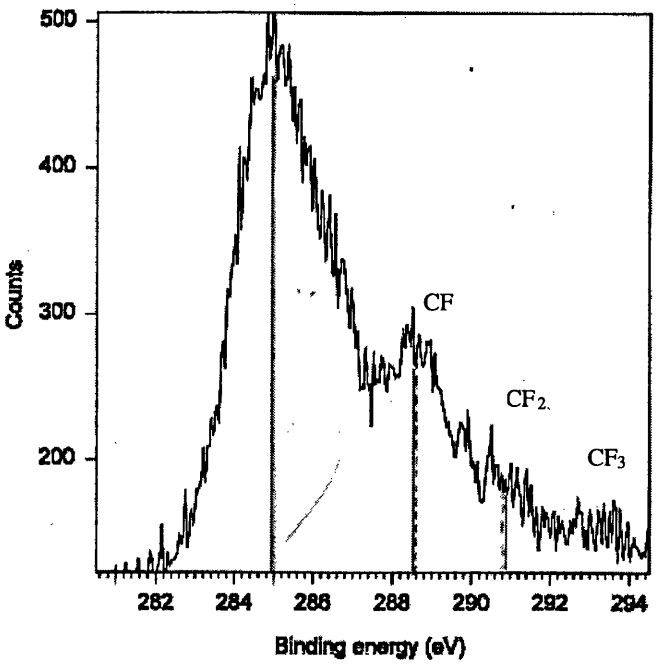

Fig. 4.4 High resolution XPS spectrum of 4% Elvacite etched in CHF_3 at 216 W/m^2 in the S100 machine.

Unfortunately, it has not been possible to distinguish between the modified PMMA and fluoropolymer deposition mechanisms with the equipment available. A possible explanation is that in the low-bias region there is sufficient fluoropolymer deposition to protect the PMMA from chemical attack by fluorine and from ion-bombardment by molecules and radicals, whereas at higher powers the combination of decreasing polymer deposition, increasing atomic fluorine and sufficient ion bombardment allows the PMMA to be etched at a much increased rate.

For comparison, PMMA and SiN_x were etched in the RIE80 machine using CHF_3, the etch rates were measured (Fig. 4.5a) and the resultant selectivities calculated (Fig. 4.5b). The gas flow was kept constant at 20 sccm and the etch pressure at 15 mT, while the R.F. power was varied from 50 W to 125 W. It is apparent that the previously observed increase in selectivity does not occur in the RIE80

machine. As already discussed there is a greater background level of oxygen in the RIE80, which affects the gas phase reactions also in a CHF_3 plasma: the residual oxygen will form the molecule CO in the gas phase, thus reducing the formation of fluorocarbon polymer [157] and increasing the etch rate of the PMMA. The oxygen will affect the quantity of fluoropolymer present in the plasma and, therefore, the degree to which the PMMA is protected. In this case it is expected that the rate of decrease in fluoropolymer formation with increasing power density is greater than for the S100 and that this is the primary reason why no peak selectivity is observed in the RIE80. These differences in the oxygen background level could be quantified using Ar actinometry, but it was not possible to do these experiments during the project due to equipment limitations. Furthermore, the identification of the molecules present in the plasma by laser spectroscopy would greatly assist the analysis and mass spectroscopy on the out-flow would allow the identification of the etched (volatile) species. However, this equipment was not available during this project.

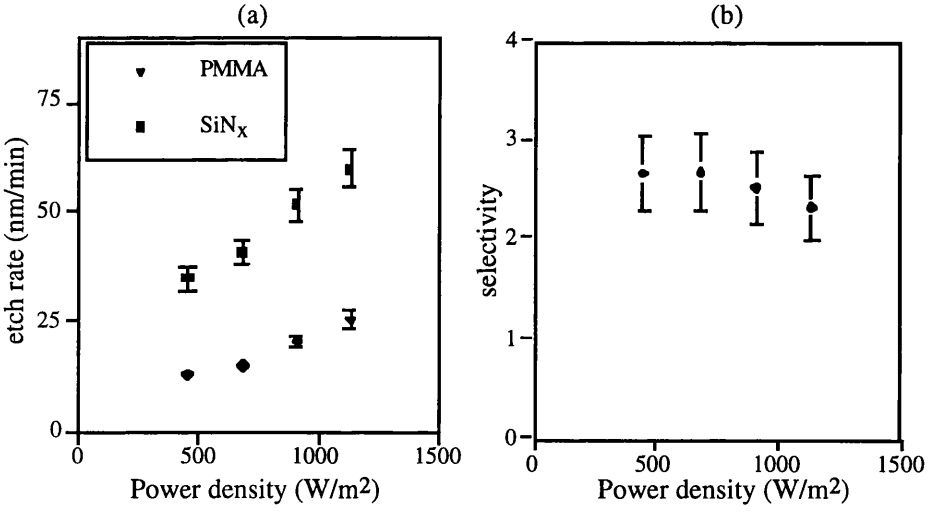

Fig. 4.5 a) Etch rate of unpatterned PMMA and SiN_x as a function of the RF power density in a CHF_3 plasma in the RIE80 machine; b) calculated selectivity of SiN_x to PMMA for the RIE80 machine.

4.1.5 Application of results to pattern transfer

The key result is that there is an optimum selectivity of SiN_x with respect to PMMA in the S100, at a power density of approximately 500 W/m^2. Fig. 4.6 shows a SEM micrograph of a 2D PBG structure in SiN_x where a 200 nm thick PMMA layer was used to etch a 330 nm thick SiN_x layer. The time of etching, 14 minutes, etched most of the PMMA mask, but the features still have very vertical sidewalls - the slight bowing at the bottom is due to the geometry of the features.

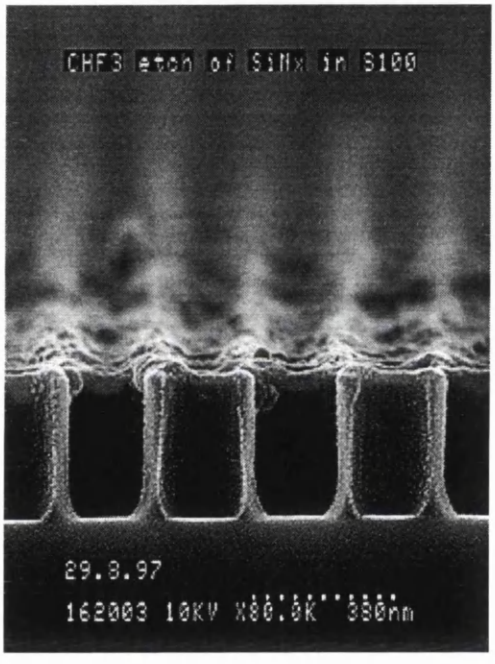

Fig. 4.6 SEM micrograph showing pattern transfer ability from PMMA to SiN_x.

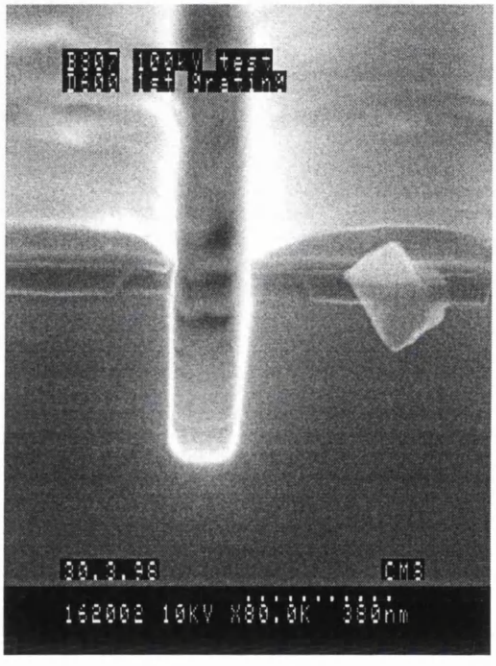

Fig. 4.7 SEM micrograph of part of a 1D grating in GaAs etched using $SiCl_4$ and a PMMA mask.

The reduction of the PMMA etch rate in $SiCl_4$ has meant that it has been possible to etch titanium directly using a PMMA mask [158]. Also, with the improved resilience, PMMA has been used to transfer features directly to GaAs to a depth of at least 400 nm (Fig. 4.7). As can be seen in the micrograph, not all the resist has been etched away and higher aspect ratio features could therefore be etched.

4.1.6 Conclusions

In conclusion, it has been shown that reductions in the etch rate of PMMA can be obtained when a RIE machine with a load-lock and a turbo pump is used. In particular, thin layers of PMMA can be used as a pattern transfer mask for shallow etching in $SiCl_4$, even at high R.F. powers. The etching of PMMA in fluorocarbon precursor gases has shown that the etching mechanism of PMMA is ion-assisted chemical etching. Specifically, in CHF_3 plasmas, a maximum in selectivity of SiN_x to PMMA etch rate in unpatterned samples is observed at a power density of approximately 500 W/m^2 for the machine with lower oxygen background levels. The improvement in selectivity has been used to improve the pattern transfer of PBG structures from PMMA to PECVD SiN_x, thus providing a better mask for subsequent reactive-ion etching in $SiCl_4$ based plasmas.

4.2 Modified AlAs layer as an intermediate pattern transfer layer

An alternative approach to the problem of pattern transfer is to seek another intermediate pattern transfer layer, where the PMMA does not limit the fabrication process. This strategy is particularly attractive as there are many disadvantages associated with the previous method, including the problems of reliable nanometre-scale lift-off and the need for deposition and etching of a dielectric film. One such possibility is the inclusion of the intermediate mask layer at the growth stage and its modification after growth to give improved masking properties. The example of an "in-situ" epitaxial layer that I have investigated is AlAs and its modification by wet thermal oxidation or treatment in a fluorine-based RIE plasma. These masks are compared with the more standard deposited dielectric layers in a $SiCl_4$ plasma and the steam oxidised layer is shown to possess excellent masking properties.

The MBE grown epitaxial structure used in these experiments consists of a thin 20 nm GaAs cap, a 75 nm AlAs layer which is to be modified to act as the intermediate pattern transfer layer, a 919 nm thick GaAs layer and an AlAs etch stop layer 20 nm thick (Fig. 4.8). A thickness of 75 nm for the top AlAs layer was chosen as the oxidation rate decreases rapidly for layers thinner than 50 nm [159].

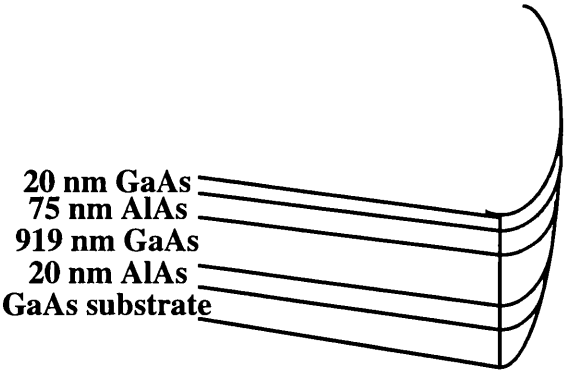

Fig. 4.8 Schematic of the MBE epitaxial structure used.

The wet thermal oxidation is carried out in a modified oxidation rig based on a commercial alloying furnace (Bio-Rad RC2400); Fig. 4.9 shows the furnace schematic.[13] The stage in the chamber incorporates a low-thermal-mass heater for rapid thermal cycling up to 750°C with the control unit, allowing accurately timed heating of the stage and digital temperature control. The furnace temperature used in this work is 380 °C, with a nitrogen carrier gas flow of 0.6 l/s flowing through a water bath at 90 °C, conditions that have been previously optimised for controllable sub-micron oxidation.

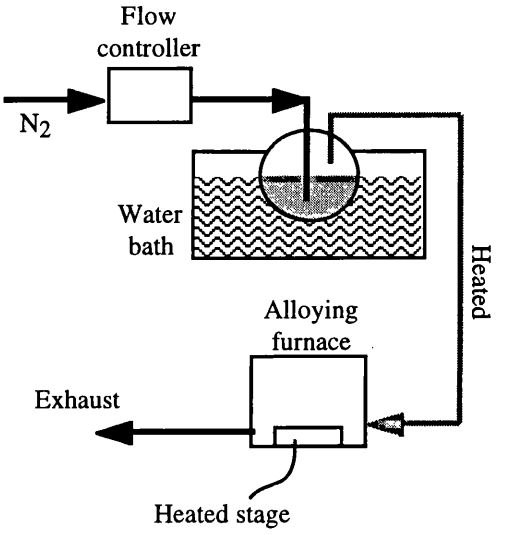

Fig. 4.9 Schematic of the oxidation rig used.

4.2.1 Wet, thermal oxidation of AlAs

The wet, thermal oxidation of AlGaAs layers (x>0.8) has been used widely in recent years [159] after Holonyak et al. [160] demonstrated that AlGaAs can be chemically changed at temperatures of approximately 400 °C into $(AlGa)_2O_3$; this porous oxide (AlOx) has approximately the same density as the original AlGaAs layer [161], but has a refractive index of around 1.6. This large reduction in effective index, while maintaining a similar physical volume, is the key to the use

[13] The oxidation rig was developed by Dr. M. Dawson at the Institute of Photonics, University of Strathclyde.

of this technology in devices. In particular, this technique has been used very effectively in Vertical Cavity Surface Emitting Lasers (VCSELs) to increase both current and optical confinement as well as increasing the bandwidth of the DBR mirror stacks [159]. Steam oxidised AlGaAs has another potential application, however, namely for pattern transfer of sub-micron features into the GaAs/AlGaAs material system, as it is more robust when exposed to a reactive plasmas [108].

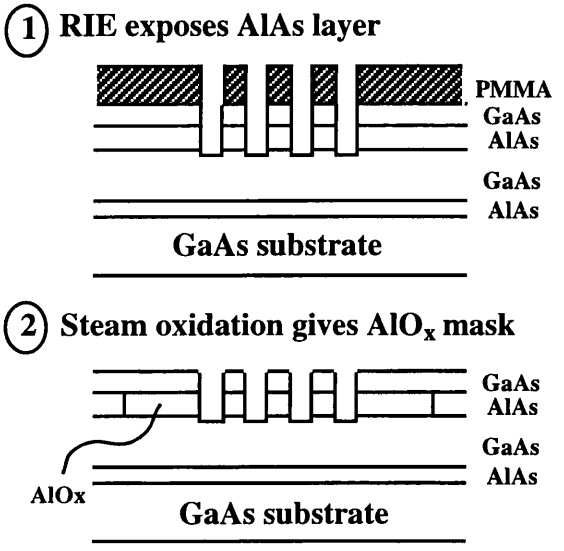

Fig. 4.10 Schematic of AlOx mask production process.

The fabrication process using a steam oxidised mask is shown in Fig. 4.10. In this particular case, one-dimensional gratings with periods varying from 150 to 250 nm with a 50% duty cycle were written. The resist features were then transferred into the top 100 nm of the epitaxial structure by $SiCl_4$ etching in the S100, which was sufficient to expose the AlAs layer. The samples were oxidised for a maximum of 5 minutes, which was sufficient to oxidise laterally between adjacent ridge edges; the colour change due to interference effects in the epitaxial material allows the oxidation front to be monitored in-situ via the optical microscope fitted above the furnace chamber. The sample was then etched in $SiCl_4/O_2$ using conditions optimised for the vertical transfer of sub-micron patterns into GaAs. The etch rate of the AlOx mask was determined by a calibration run to be on the order of 3 nm/min. An etch rate of 200 nm/min for GaAs results in a

selectivity of 70:1 between the mask and semiconductor. This high selectivity, when combined with highly anisotropic RIE, allows the fabrication of nanometre structures with high aspect-ratios (Fig. 4.11).

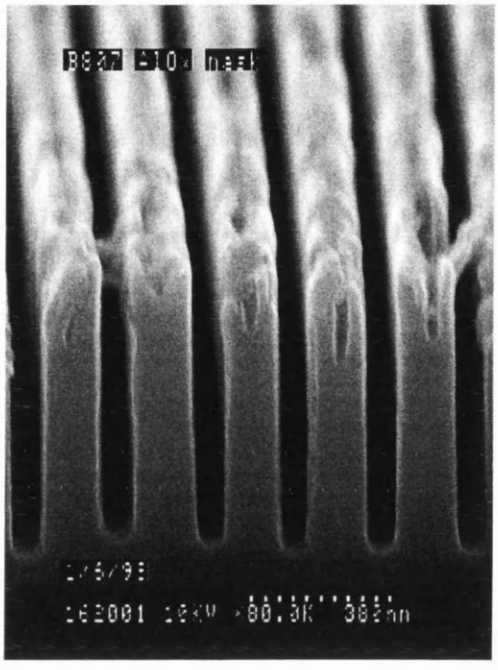

Fig. 4.11 Grating with nanometre sized features and an aspect ratio of 10 fabricated using an oxidised AlAs mask.

4.2.2 Problems with AlAs oxidation

The examination of the etched patterns after the initial RIE stage sometimes indicated that there were problems of spontaneous native oxide formation (Fig. 4.12); native oxide here means the oxide that results from the room temperature reaction of atmospheric gases with the Al in the epitaxial layer.

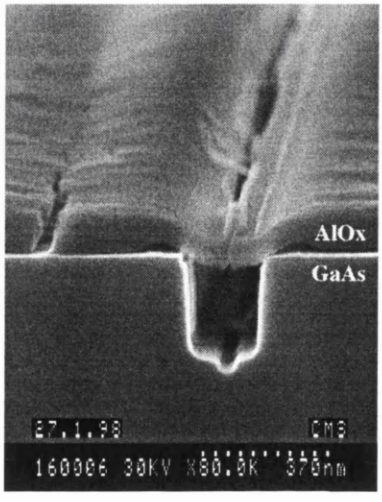

Fig. 4.12 SEM micrograph of spontaneous oxidation of AlAs layer after first RIE step.

The formation of a native oxide was expected, but the extent of the lateral oxidation in the short time between etching and examination could not be solely attributable to spontaneous oxidation. These effects were only observed on samples which had been through the initial pattern definition process more than once. Possible explanations for the rapid ambient oxidation could be exposure of the semiconductor to excessive thermal cycling or chemical attack by the developer or other solvents used in the stripping of resist. This problem was overcome by taking care not to process any piece of material more than once. Another possible cause could be the use of AlAs itself as it is more reactive than AlGaAs alloys. This problem, however, could be overcome by using a high Al molar fraction $Al_xGa_{1-x}As$ layer ($0.8<x<0.98$) rather than an AlAs layer. The oxidation rate of $Al_xGa_{1-x}As$ is an increasing exponential function of the Al molar fraction, which considering the small scale of the patterns would not be a problem here.

4.2.3 Comparison of masks

In comparison with SiO_2 and SiN_x the etch rate of the steam oxidised AlAs layer is approximately an order of magnitude smaller. As far as feature size is concerned no limitations of using the AlOx approach for pattern transfer purposes have been seen for features as small as 50 nm, so this technology can be used for a wide range of GaAs-based device structures.

Material	Etch rate (nm/min)	Selectivity
SiO_2 (PECVD)	19	10.5:1
SiN_x (PECVD)	21	9.5:1
AlOx	3	70:1

Table 4.4 Comparison of different masks in a $SiCl_4/O_2$ plasma; selectivity is for the mask material with respect to GaAs.

4.2.4 Plasma fluorination of AlAs

The treatment of AlAs in fluorine-based plasmas has not previously been reported to my knowledge, although fluorine addition to chlorine plasmas has already been shown to provide selective etching of GaAs over AlGaAs, by the formation of an AlO_xF_y film at the AlGaAs surface [148]. Sputtered metal halide films have also been used as electron-beam resists [162] and are used for IR coatings [163]. The use of plasma treatment to create an amorphous AlF_x layer seeks to extend these techniques.

Windows were firstly opened in Shipley S1818 resist. The GaAs cap was then removed using a selective RIE process [148]. The chamber was then purged with nitrogen for 20 minutes, while still under vacuum; after which, the exposed AlAs layer was exposed to an SF_6 plasma (23 sccm, 50 mT, 50 W) for 2 minutes. The process is shown in Fig. 4.13. The sample was then removed and the photoresist stripped in acetone. Thereafter, the sample was etched in the S100 machine in $SiCl_4/O_2$. Initial inspection revealed that the process did produce a negative mask and reproduced the general outline of the resist features (Fig. 4.14), but closer inspection showed that the mask was not uniform (Fig. 4.15).

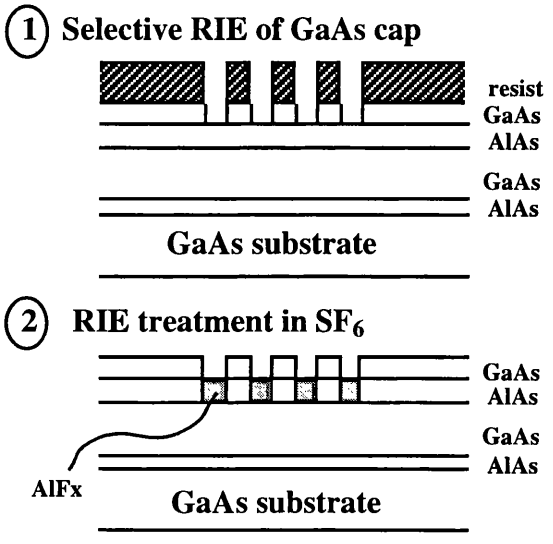

Fig. 4.13 Schematic of AlAs fluorination process.

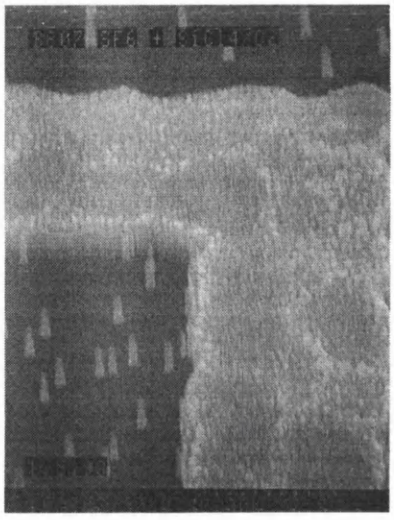

Fig. 4.14 SEM micrograph of a fluorinated AlAs layer used as a pattern transfer mask in $SiCl_4/O_2$ in the S100 machine. The general features of the original photoresist mask can still be seen.

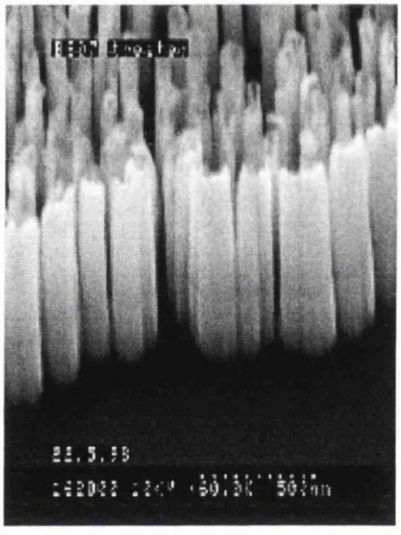

Fig. 4.15 Closer examination reveals non-uniformity of the fluorinated AlAs layer.

At present the mechanism which modifies the AlAs layer is not clear but a possible explanation is the chemical reaction of the surface arsenic with the fluorine dissociated from the plasma, to produce AsF_3, which is volatile. This reaction would leave behind Al to react with the F and form AlF_3, a dielectric, and then oxidise on exposure to the atmosphere after the sample is removed from the RIE chamber. In order to investigate this possible mechanism secondary ion mass spectrometry (SIMS) measurements were performed to determine the elements present at the surface.[14]

[14] SIMS measurements were carried out by Loughborough Consultants.

Four samples were prepared, the first three of which had the GaAs cap removed, and then the AlAs layer had been exposed to an SF_6 plasma for 2, 8 and 20 minutes. In the final sample, the GaAs cap was not removed and the sample was exposed to an SF_6 plasma for 8 minutes under the same conditions as above. The analysis was performed by Cs^+ primary ion bombardment and negative secondary ion detection to optimise the sensitivity to oxygen, fluorine and sulphur.

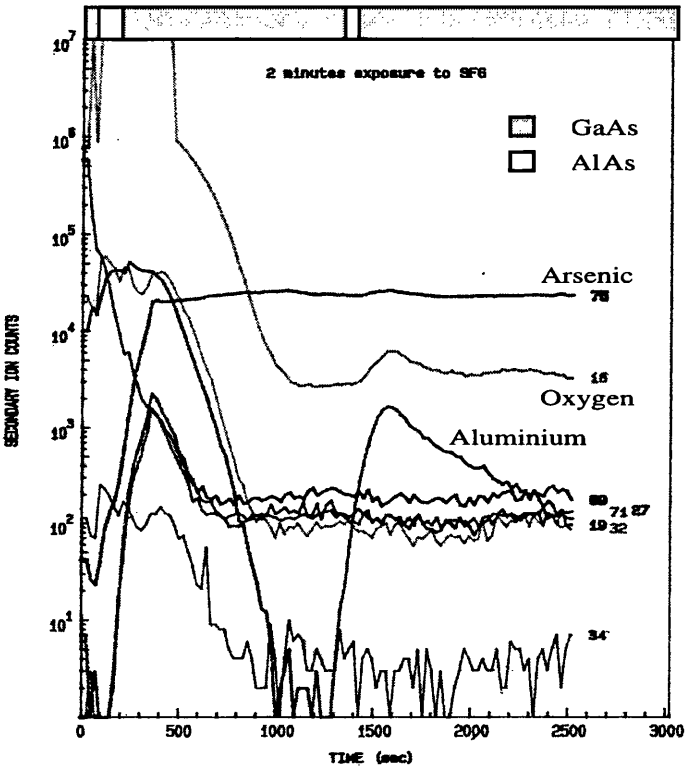

Fig. 4.16 SIMS spectra for a sample exposed to SF_6 for 2 minutes after the removal of the GaAs cap; numbers are atomic masses.

Fig. 4.16 shows the depth profile obtained for the sample exposed for 2 minutes; similar spectra are obtained for both the 8 and 20 minute samples. In comparison to the control sample (Fig. 4.17) there is evidence of a large fraction of oxygen and fluorine at the surface, along with a depletion in arsenic. Even in the sample in which the GaAs cap was not removed, there is evidence of some fluorination and

arsenic deficiency at the surface. These results suggest that there is a mechanism which is depleting the surface region of arsenic and allowing the incorporation of fluorine and oxygen. This technique, if developed further, could potentially provide an alternative form of negative lithography, which does not involve a lift-off process. Any future work in this area would be best focused on modelling to determine the viability of this technique.

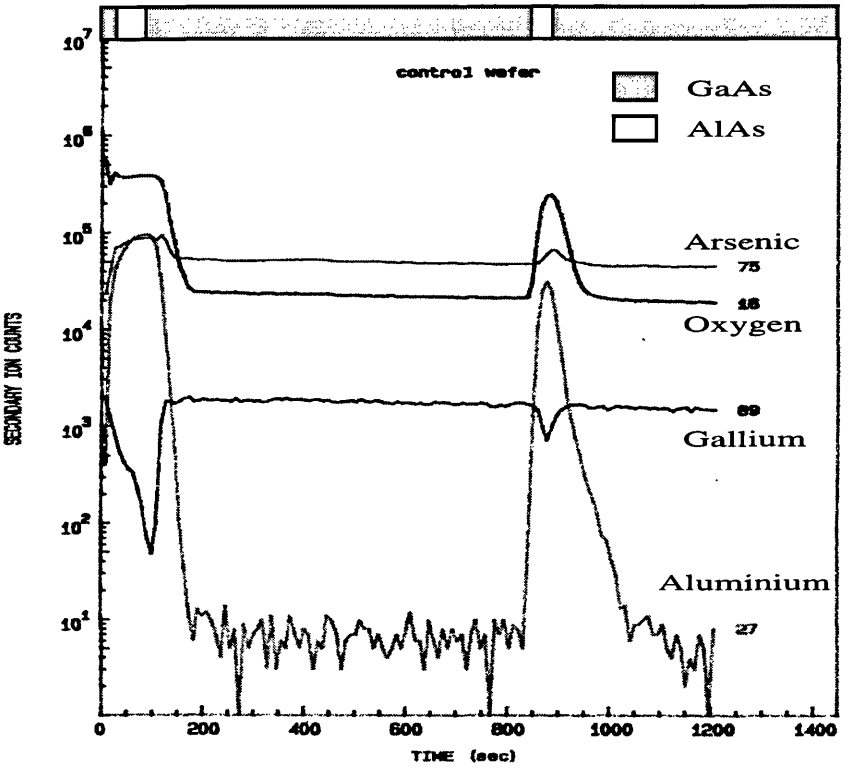

Fig. 4.17 SIMS spectra of control sample, which had not been etched.

4.3 Conclusion

The detailed examination of the complete fabrication process has brought improvements in the fabrication of PBG structures in AlGaAs. Unfortunately, it has still not allowed the fabrication of InP-based PBG structures. Alternative strategies for pattern transfer to AlGaAs heterostructures have been developed and have shown very encouraging results.

5. Photonic bandgap structures : design considerations and characterisation

The realisation of devices incorporating photonic microstructures is difficult due to the complicated relationship between the various design parameters. In this chapter, the complicated issues associated with PBG device design will be discussed in reference to actual devices. Thereafter, the characterisation of the PBG structures carried out as part of this project will be presented.

5.1 Optical waveguide design

The key consideration in designing a waveguide is the degree of optical confinement of the mode. Ideally, for 2D PBG structures an infinitely wide mode would be desirable, namely a plane wave, but this approach is not practically feasible. The alternative approach is to provide the maximum possible confinement. The highest degree of optical confinement is provided by a membrane waveguide [103], where the waveguide core is surrounded by air or low index dielectric on both sides. Unfortunately, the methods to fabricate such membrane waveguides in III-V semiconductors has only recently been applied to this domain [164]. The most obvious strategy, therefore, was to use conventional heterostructure waveguides and determine whether 2D PBG structures could be realised in such an optical guide.

The key limitation here is the loss that occurs at the multiple semiconductor/air interfaces found in PBG structures. At such interfaces, light is diffracted out of the optical waveguide, thus constituting a loss.[15] The magnitude of this loss can be minimised in two extreme cases: the first when only the evanescent tail of the mode

[15] It is possible to design periodic semiconductor/air interfaces in which there is no diffraction out of the guiding plane. These designs generally require the use of single moded guides and sub first order grating structures.

interacts with the periodic structure (Fig. 5.1a) as used in DFB lasers or secondly, when the whole mode interacts with the periodic structure (Fig. 5.1b). Strong interactions between the material and the mode mean that the second option is the logical choice. In order that the whole guided mode interact with the periodic structure, however, the guided mode must have a vertical extent less than the maximum possible etch depth. In the case of an AlGaAs/GaAs heterostructure and for periods of approximately 200 nm, this maximum etch depth is between 0.8 and 1.0 μm.

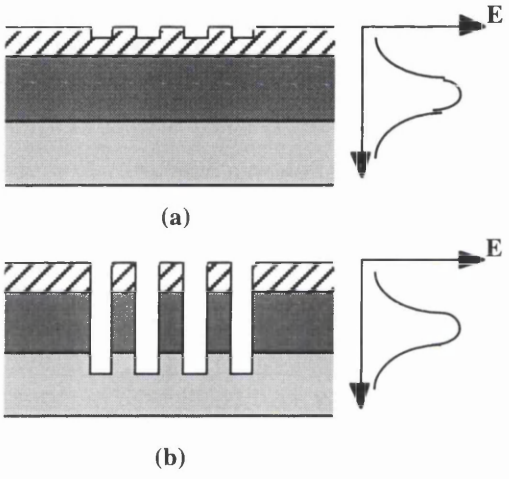

Fig. 5.1 a) Weak periodic refractive index modulation interacting with evanescent field and b) strong periodic refractive index modulation interacting with the whole mode.

This requirement on the optical confinement means that large refractive index differences in the heterostructure are desirable. This requirement needs to be considered simultaneously with the cut-off wavelength for the waveguide. The GaAs/AlGaAs material system will be specifically addressed as it is a typical example of III-V semiconductor-based guides. In $Al_xGa_{1-x}As$, as the molar fraction x increases the refractive index and the cut-off wavelength decrease [165]. Since the refractive index of GaAs is higher than that of any AlGaAs alloy, it is

necessary to include a buffer layer between the substrate and the waveguide in order to avoid leakage into the substrate.

Fig. 5.2 shows the heterostructure used for a passive PBG experiment, which satisfies all these criteria [93]. The mode profile was calculated using the program Fwave,[16] Fig. 5.3 shows the plot for the fundamental mode. The AlGaAs core is used to ensure transparency from 800 nm upwards, which corresponds to the lower wavelength of the Ti:Al_2O_3 laser tuning range. The thickness was chosen to ensure single mode operation and minimum spread into the cladding.

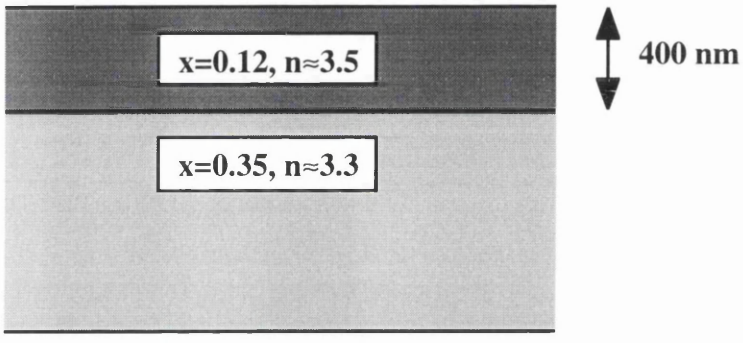

Fig. 5.2 AlGaAs surface waveguide.

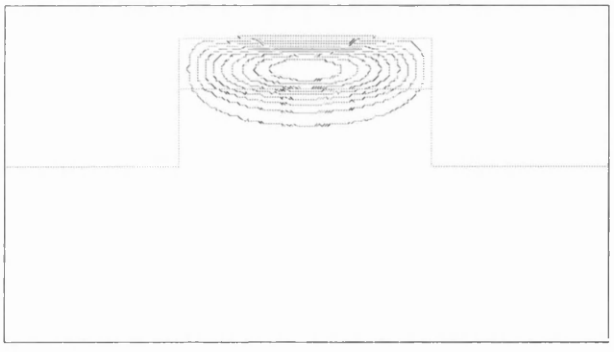

Fig. 5.3 FWave plot of electric field for fundamental mode; lines are 10% gradients.

[16] Fwave is a Macintosh freeware program developed by M. Taylor at Glasgow University, which solves for the field in an user-defined waveguide structure.

An alternative heterostructure which was used for characterisation of PBG structures is shown in Fig. 5.4 [111]. In this instance three layers of self-organised InAs quantum dots (QD) with a natural luminescence greater than the asborption edge of GaAs are embedded in the guide. GaAs is, therefore, used in the waveguide core since it provides the maximum possible confinement. The $Al_{0.8}Ga_{0.2}As$ (80% AlGaAs) layers are included for electron confinement.

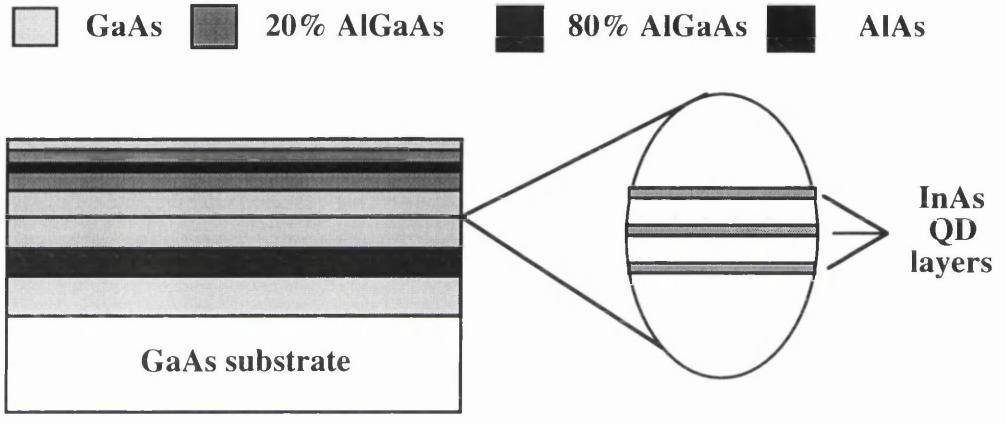

Layer	Material	Thickness (nm)
1	GaAs	500
2	$Al_{0.8}Ga_{0.2}As$	400
3	GaAs	100
4	InAs/GaAs x3	1/10
5	GaAs	100
6	$Al_{0.2}Ga_{0.8}As$	150
7	AlAs	10
8	$Al_{0.2}Ga_{0.8}As$	150
9	GaAs	10

Fig. 5.4 Heterostructure used to probe PBG structures.

Already, the complicated trade-offs in design have been shown and some of the interdependences have been highlighted, principally the need to design the limitations of the fabrication technology into the heterostructure.

5.2 Photonic bandgap structure design

The design of PBG structures is best done by using the various methods of calculation discussed in Chapter 2, but one quick method for designing PBG structures is the use of gap-maps (Fig. 5.5). This method is approximate because the index may be different, but even with accurate calculations there will be an experimental error in the spectral position of the band-edge. For our discussions we shall consider a 2D array of holes arranged in a triangular lattice.

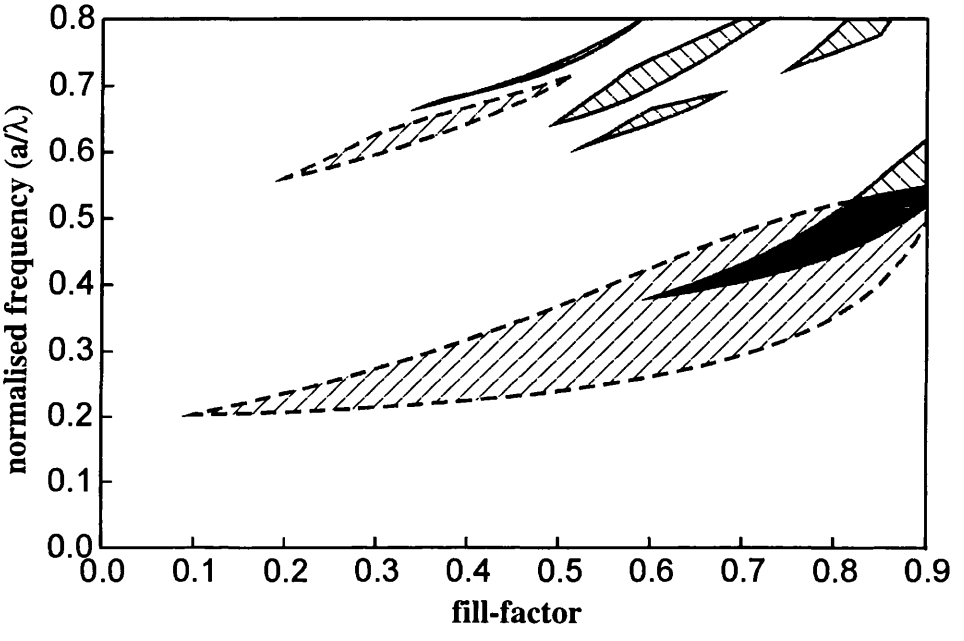

Fig. 5.5 Gap-map for triangular lattice of air holes in AlGaAs, ε=11.0 (calculations performed by D. Cassagne at Université de Montpellier II, France).

As shown in Fig. 5.5 the largest bandgap for both polarisations is obtained when the fill-factor is approximately 0.8.[17] In this ideal case where the PBG structure has infinite extent in the plane perpendicular to the direction of propagation, a complete 2D PBG would be obtained. However, in all the applications considered in this project, the PBG structures were fabricated in an optical waveguide, where

[17] This value of fill-factor corresponds approximately to the quarter-wavelength condition.

plane waves are not used. In order to minimise the scattering out-of-plane discussed in §5.1, it is necessary to reduce the radius of the holes. I have used a typical fill-factor of 0.32 [93]. A consequence of this reduction in the normalised radius is that only a bandgap in TE polarisation is obtainable. This bandgap for one polarisation, however, has many potential applications due to the preferential emission of TE polarised light from many of the different quantum well materials used in light emitting devices, e.g. VCSELs.

Once the normalised radius has been chosen, the period is determined for a particular stop-band position. Once again other external factors, such as the optical waveguide and the experimental set-up, however, affect the implementation of the PBG structures; the absorption edge of the guide core may only allow a fraction of the bandgap to be probed, whereas the experimental set-up could have a limited detection range. It is frequently required, therefore, that several periods with the same normalised radius are fabricated simultaneously in order to probe the full range of PBG properties, i.e. both band-edges and features in the stopband [93].

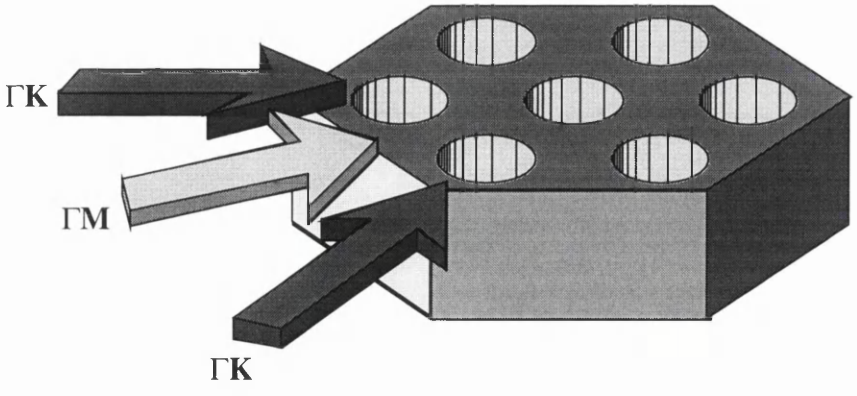

Fig. 5.6 The most distinct directions in a triangular lattice - ΓK and ΓM.

The policy adopted in this project was that of Krauss et al. [93] in which only the principal symmetry directions were investigated. Fig. 5.6 illustrates this approach for the triangular lattice in which ΓK (the principal symmetry direction) and ΓM are chosen. The philosophy is that if there is a photonic bandgap for both of these most distinct crystal orientations then a complete stopband will exist for that polarisation [99].

5.3 Experimental set-up

All the characterisation results have been obtained using the set-up demonstrated by Labilloy et al. [166], which was specially designed for the characterisation of PBG structures and devices.

The experimental principle is shown in Fig. 5.7 and Fig. 5.8, whereby the spontaneous emission from either InGaAs quantum wells or InAs quantum dots is optically excited using a red laser diode (λ=678 nm). Some of the excited light is confined within the optical waveguide due to total internal reflection at the interfaces and this guided light can then be used to probe the microstructure under investigation. The guided light is subsequently collected at the cleaved facet using a microscope objective, coupled into a fibre and the spectral analysis of the collected light is finally carried out using an optical multichannel analyser.

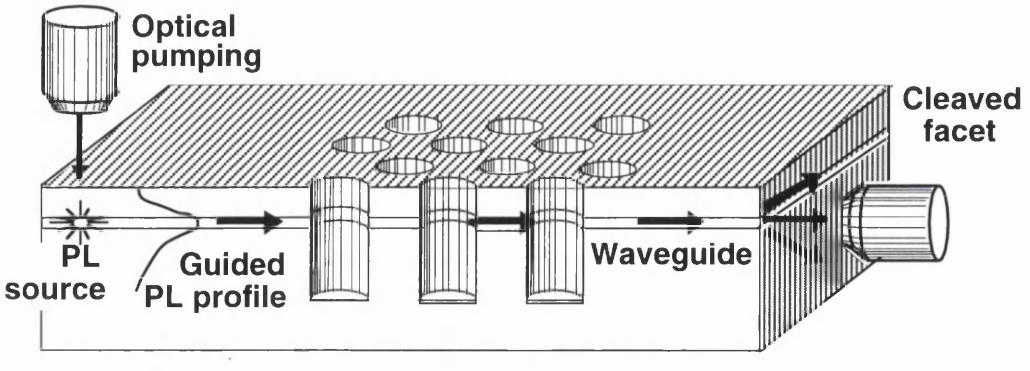

Fig. 5.7 Schematic of experimental principle (courtesy of D. Labilloy).

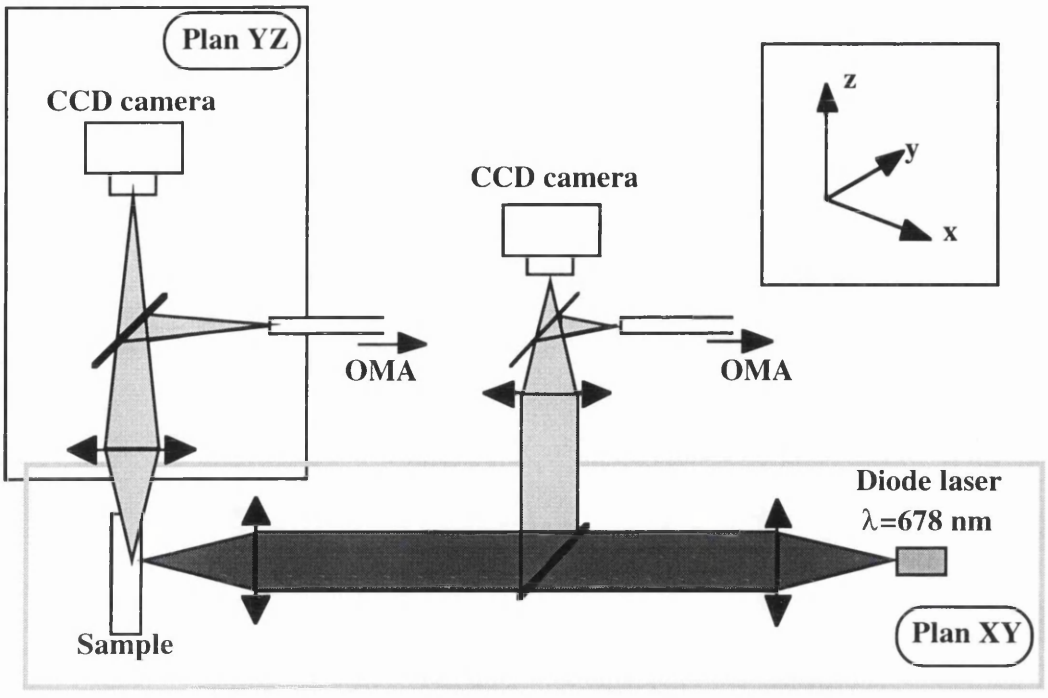

Fig. 5.8 Experimental set-up used to characterise PBG structures.

The use of quantum wells and quantum dots produces an internal source with which to probe the PBG structures. However, and more importantly the heterostructure incorporating the QWs and QDs is almost identical to a heterostructure that would be used for electroluminescence [110]. Quantum dots provide 3D electron confinement and, therefore, are more efficient at localising electron-hole pairs. Moreover, reactive-ion etching induced damage does not degrade the photoluminescence intensity as significantly in QDs as in QWs. The InAs quantum dots used in these experiments were grown by the Stranski-Krastanov method [167], which is the self-organisation of islands due to carefully chosen growth conditions. In these experiments the growth conditions have been optimised for a large variation in dot sizes. At room temperature, this produces a broad spectrum with which to probe the photonic microstructures (Fig. 5.9). One disadvantage of using QDs is that unpumped dots absorb at the emission wavelengths, which means that the distance over which the photoluminescence signal can travel is limited by the absorption, $\alpha \approx 40\ cm^{-1}$. This signal attenuation

affects the maximum distance of travel and, therefore, affects the layout design, as will be shown in the next section.

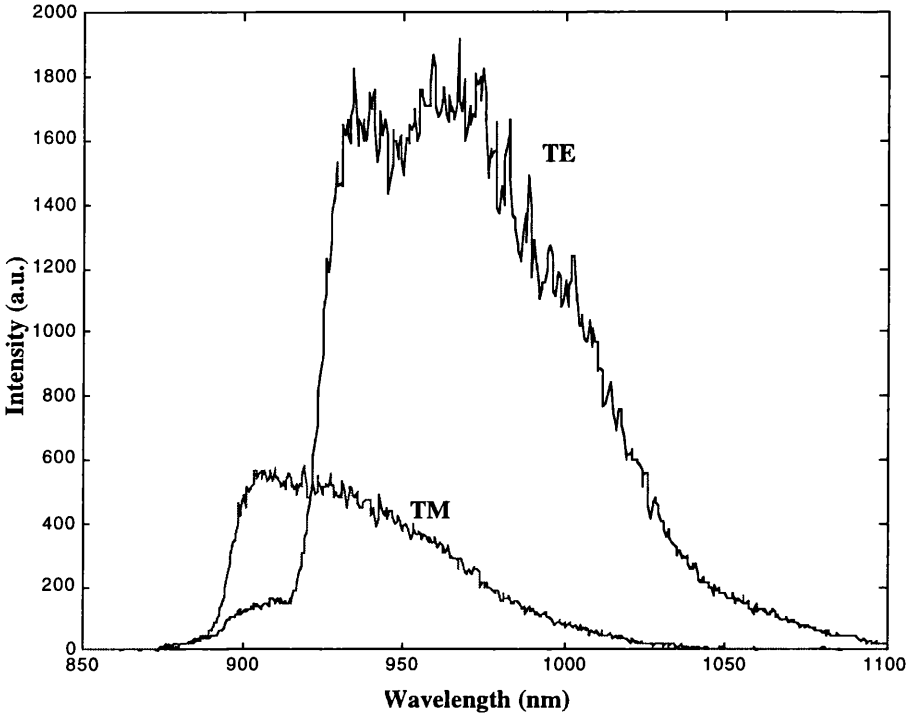

Fig. 5.9 Quantum dot photoluminescence spectra for TE and TM polarisations.

The measurement technique allows highly spatially resolved measurements which is of particular importance as it allows many patterns to be spaced closely together. The close packing of patterns is important as it ensures that any difference in PL intensity across the wafer, due to local variations in the material properties, does not affect the quantitative measurement of the PBG properties. The last limitation of the experimental apparatus is the CCD detector in the OMA. The detector is made of silicon and so has an upper detection edge of approximately 1.1 μm. This measurement technique has, however, proven to be very successful in probing the interaction of guided optical modes with PBG structures.

5.4 Final sample design

The final design of photonic microstructures and their arrangement on the sample is dictated by several factors, some of which relate to the experimental set-up and others which relate to necessary restrictions of the fabrication process. The principal experimental factors are the maximum travel of the translation stage and the absorption of the active material. The limited travel of the stage means that the length of the sample should not exceed 7 mm, whereas the absorption in the guide means that the microstructure patterns should be located as close to the edge as possible, typically less than 50 μm. This requirement is closely related to one of the fabrication limits, namely the resolution with which a semiconductor sample can be cleaved, which is typically around 50 μm. In order to ensure that there are microstructures sufficiently close to the edge, however, it is necessary that several copies of the same pattern are written, but which are offset vertically with respect to each other (Fig. 5.10).

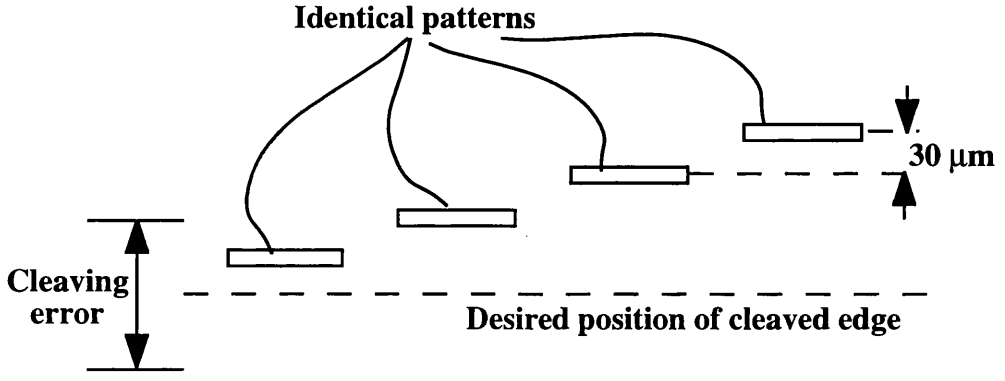

Fig. 5.10 Schematic showing the necessary vertical offset of identical patterns near the desired cleaved edge.

Experimental limitations, as explained in §5.2, meant that the approach developed by Krauss et al. [93] of using several periods is used. This approach of using various periods to scan the photonic bandgap depends on the ability to maintain the

normalised radius as the period is varied. In order to accomplish this in reality it is necessary that two identical but spatially separated patterns are written with different doses. The two different doses are also required as there can be small fluctuations in the resist thickness, the sample height and the developer strength and temperature, all of which can affect the fill-factor of the microstructures eventually realised.

A schematic of a typical layout for patterns to probe a photonic bandgap is shown in Fig. 5.11. Due to the need for multiple doses, multiple pattern copies and structures with different crystallographic orientations the complexity of the pattern layout on the sample is considerable. However, this approach is still an effective method to characterise photonic bandgap structures, due to the limitations of all experimental measurement techniques.

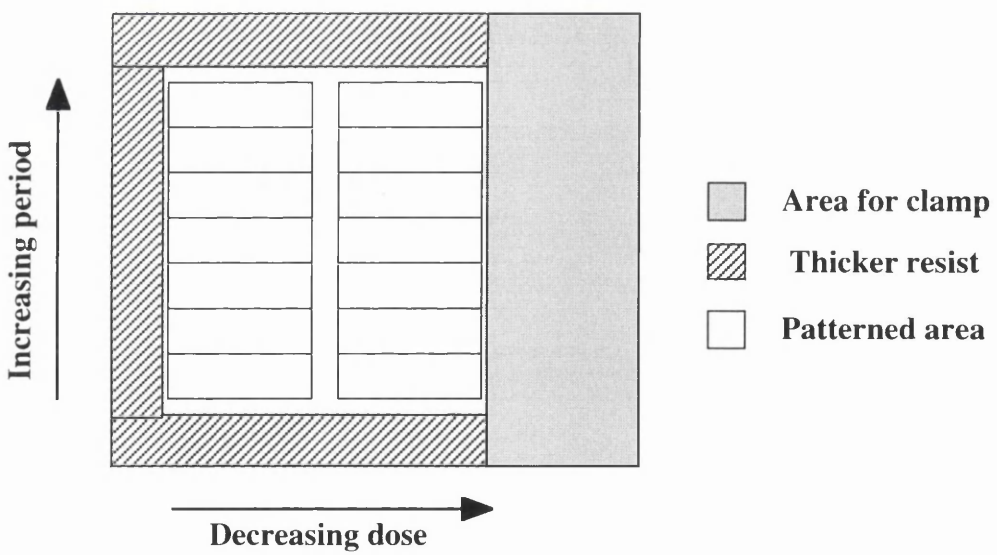

Fig. 5.11 Schematic of pattern layout on wafer section.

5.5 PBG structure characterisation

Once the experiment has been designed, the samples are fabricated as described in Chapter 3. The epitaxial heterostructure material used in these experiments was grown by U. Oesterle and R. Houdré at the Ecole Polytechnique Fédéral de Lausanne, Switzerland using the MBE growth technique. Self-organised quantum dots were used in these experiment due to their wider natural photoluminescence at room temperature. Fig. 5.12 is a SEM micrograph of a plan view of a PBG structure, which was characterised by Dominique Labilloy at Ecole Polytechnique, Palaiseau in France using the above-explained experimental set-up .

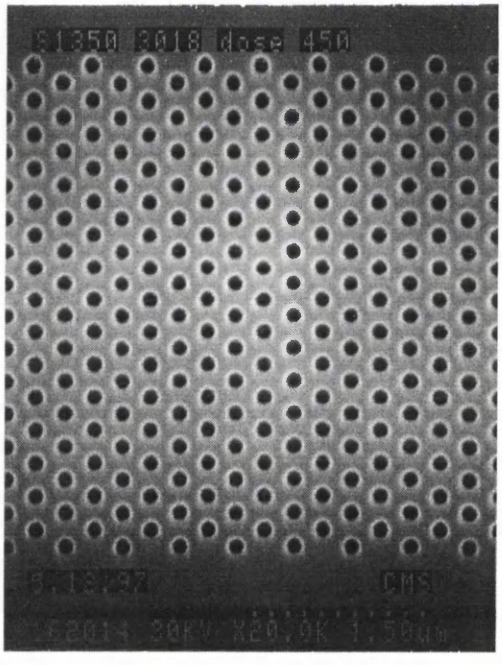

Fig. 5.12 SEM micrograph showing plan view of a PBG structure.

The measured results are shown in Fig. 5.13 in the next four pages along with calculated transmisison curves calculated by David Cassagne at Université de Montpellier II. The theoretical transmission values are shown underneath the corresponding measured values.

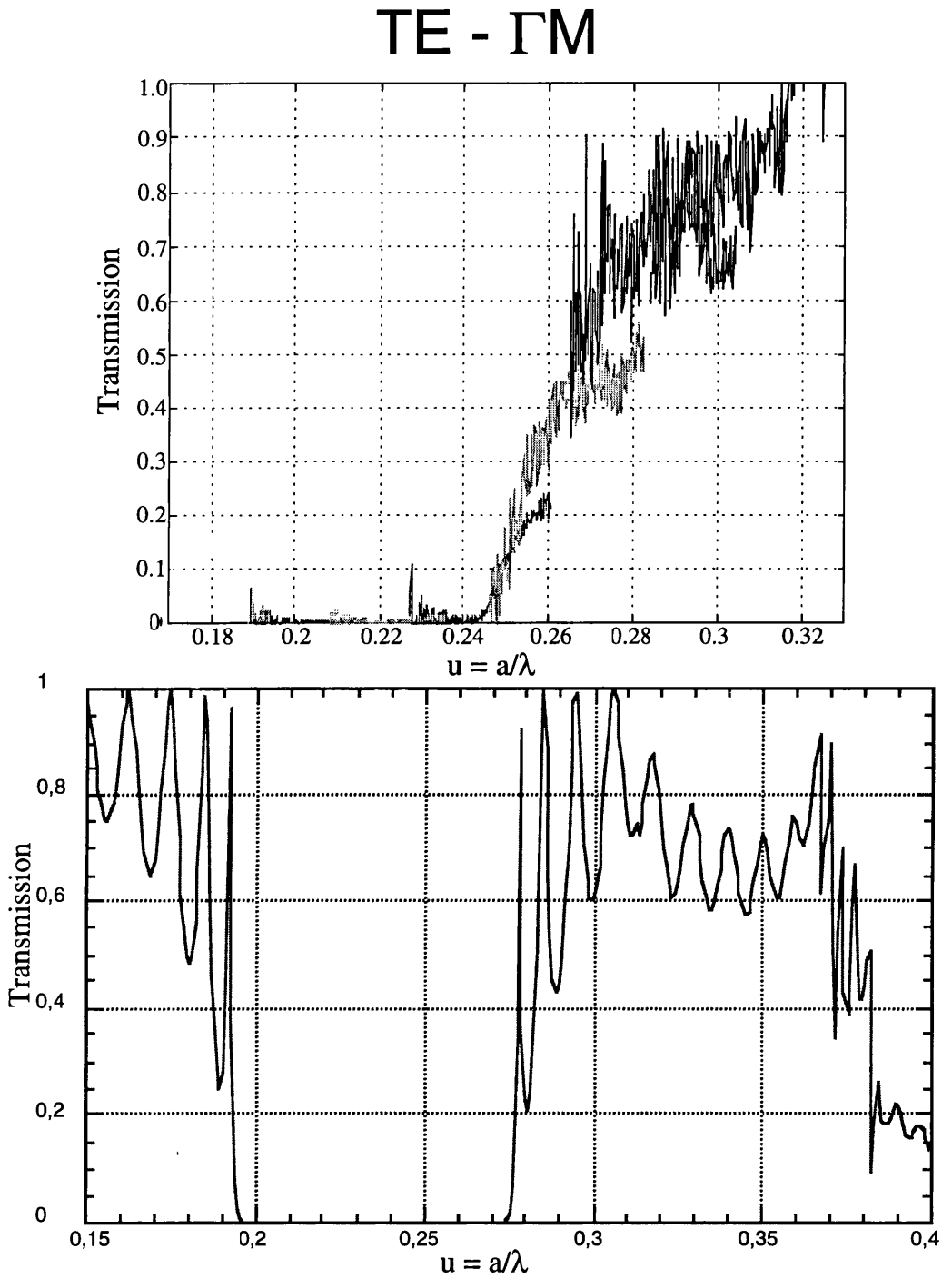

Fig 5.13a Transmission measurements (top) for samples with periods ranging from 180 nm to 260 nm with a constant fill-factor, shown by different grey-scales, and theoretical calculations (bottom) for comparison. Figure courtesy of D. Labilloy.

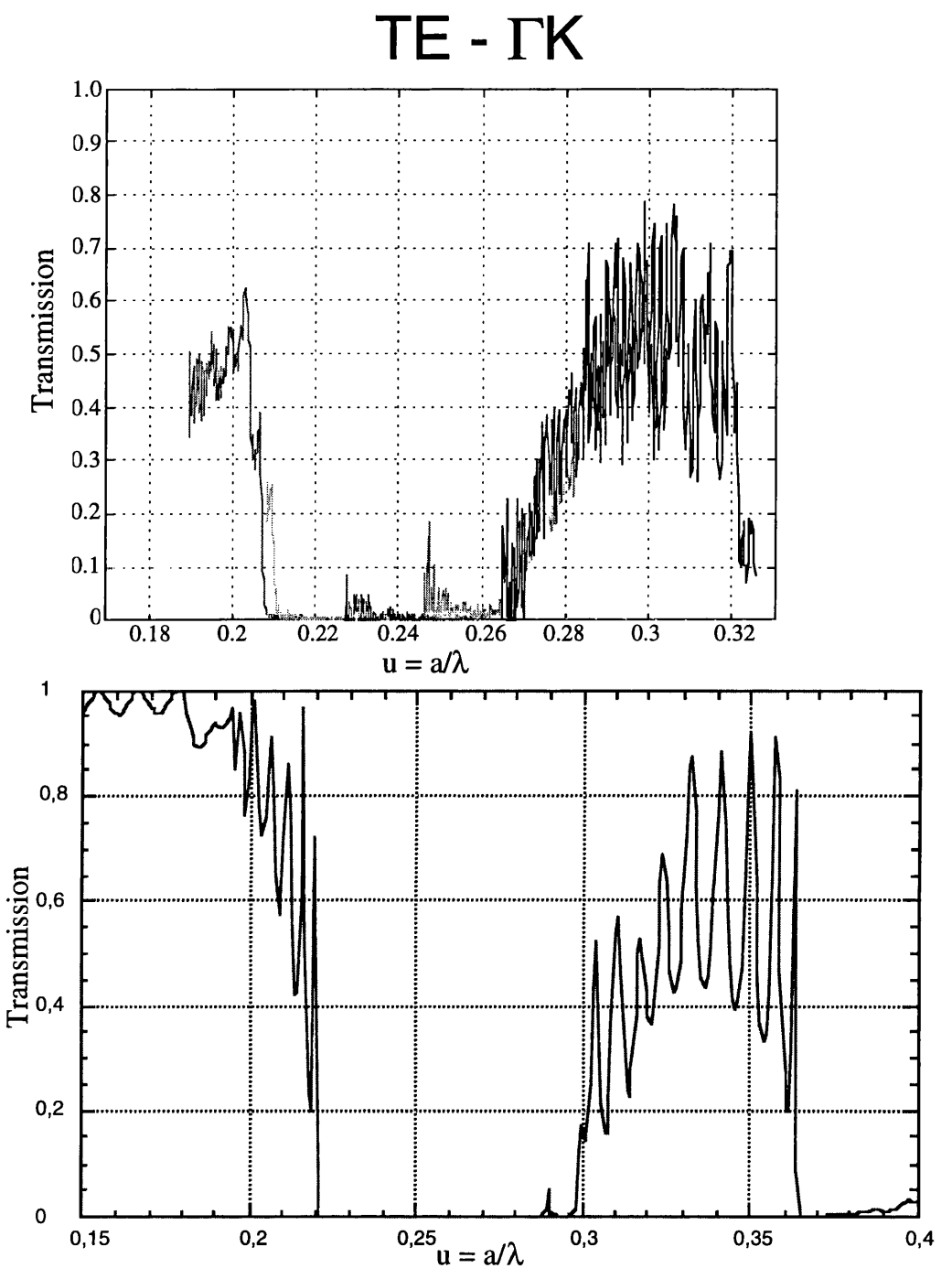

Fig 5.13b Transmission measurements (top) for samples with periods ranging from 180 nm to 260 nm with a constant fill-factor, shown by different grey-scales, and theoretical calculations (bottom) for comparison. Figure courtesy of D. Labilloy.

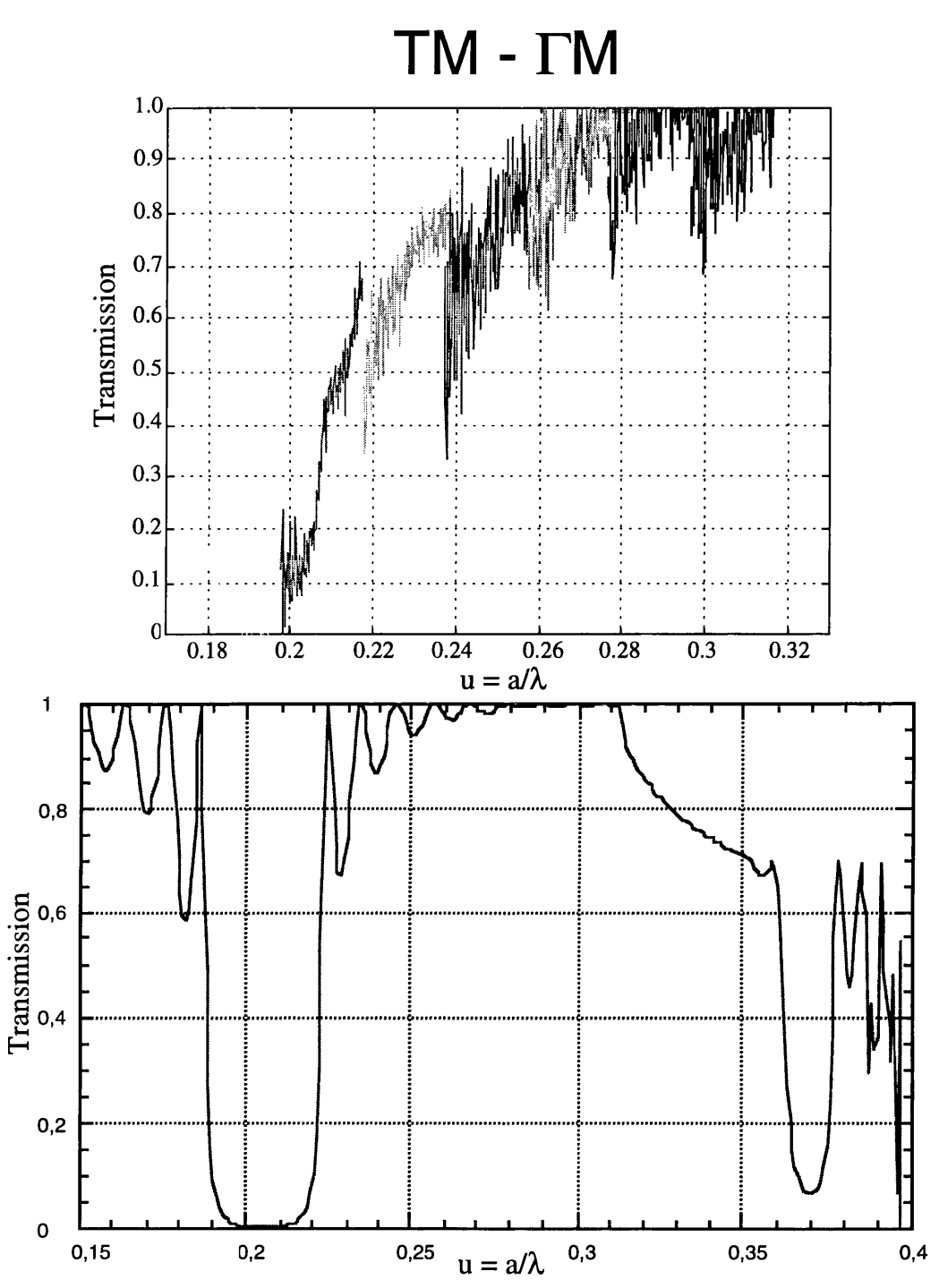

Fig 5.13c Transmission measurements (top) for samples with periods ranging from 180 nm to 260 nm with a constant fill-factor, shown by different grey-scales, and theoretical calculations (bottom) for comparison. Figure courtesy of D. Labilloy.

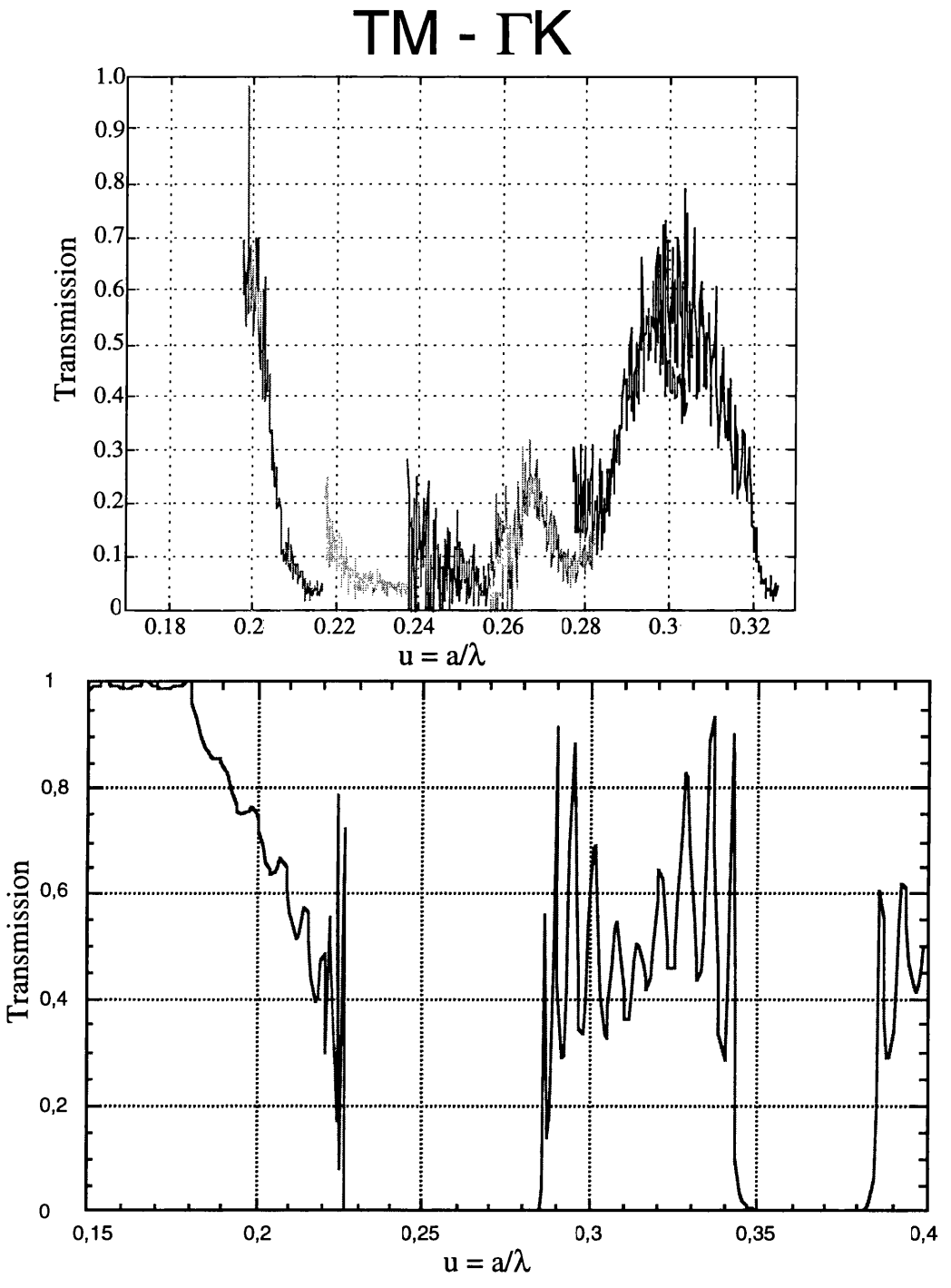

Fig. 5.13 Comparison of experimental measurements on PBG structures and calculations (courtesy of D. Labilloy). The experimental results show the overlap of the measurements from different periods.

The wide spectral range of the QDs as compared with the QWs, that have already been mentioned, allows the complete stopband to be measured since spectra from

different periods overlap with each other. The above figures show that there is a full photonic bandgap for TE polarisation, i.e. an overlap of the stopbands for both ΓK and ΓM. In TM polarisation there are measured stopbands in both ΓK and ΓM, but they do not overlap so there is not a photonic bandgap for this polarisation. It should be noted that the stopband for ΓK in TM polarisation is not predicted from bandstructure calculations and the observed low in transmission results from the problems of coupling from waveguide modes to higher order lattice modes, as previously reported [99].

Fig. 5.14 shows a better comparison between theory and experiment for a 15 row PBG structure and TE polarisation in the form of the band-diagram. There is good agreement between the theoretical calculations and the experimental results for the calculated parameters of a relative permittivity of 11.3 and a fill-factor of 0.25. The relative permittivity corresponds to the effective index of the waveguide of 3.36, and the fill-factor was fitted to represents the experimentally measured value.

In conclusion, it can be seen that PBG structures can be designed, fabricated and implemented in heterostructures. These results in particular provide a solid base from which to apply PBG technology to devices.

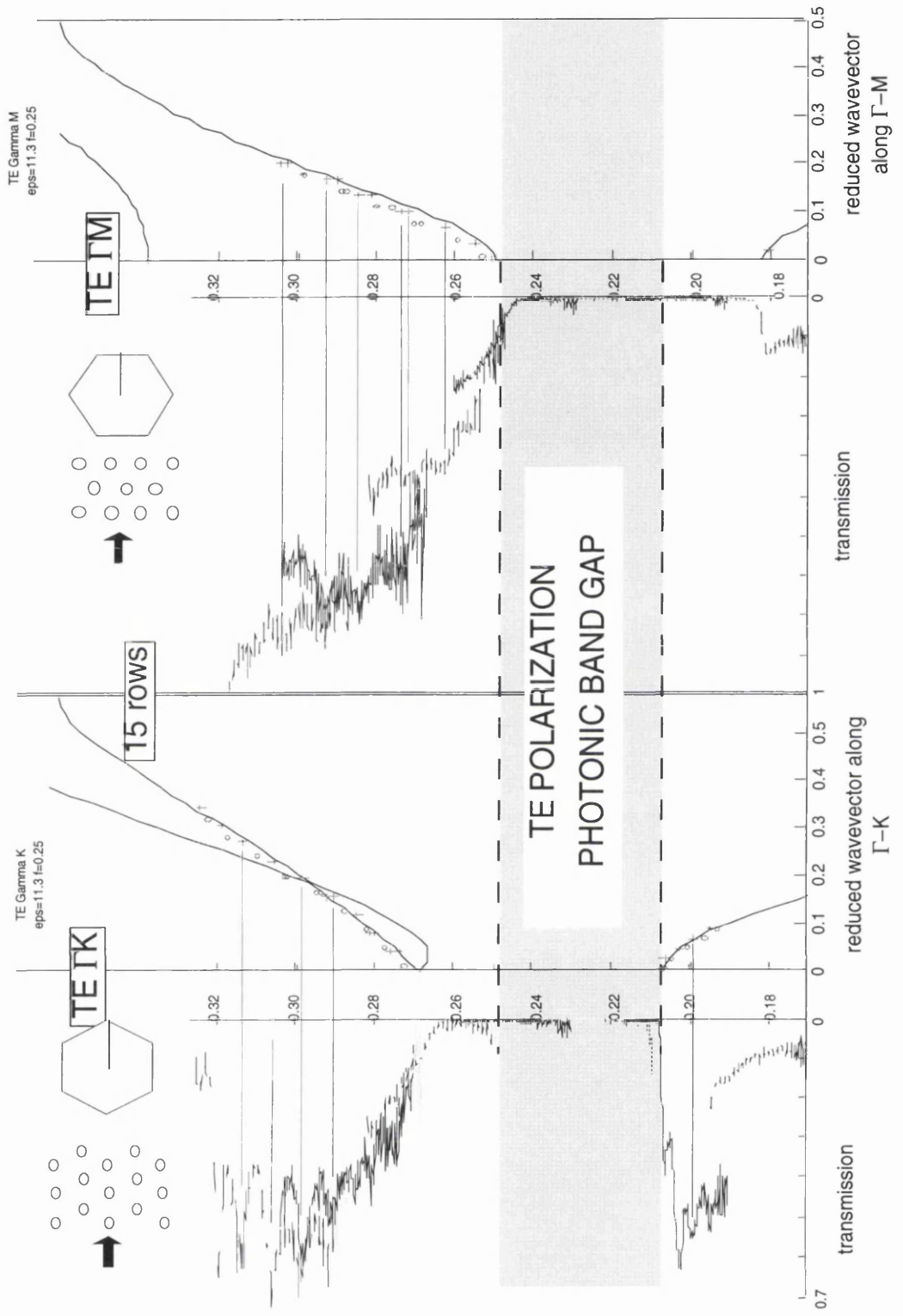

Fig. 5.14 Dispersion diagram for TE polarisation showing the high degree of agreement between theoretical and experimental values (courtesy of D. Labilloy and H. Bensity).

6. Photonic bandgap structures and microcavities

In the previous chapter it was shown that the measurements on waveguide-based photonic microstructures agree well with theoretical calculations. This chapter will deal with the application of this technology to planar microcavities. The general concept of a microcavity is introduced along with the principal motivation for work in this field, then the characterisation of cavity microstructures is shown. Finally, I will discuss the potential of PBG structures for applications in device structures.

6.1 Microcavities

An optical microcavity, as it name suggests, is a cavity with at least one characteristic dimension on the micrometre-size scale. Specifically, it is a resonator with 1-, 2- or 3-degrees of confinement. These degrees of photon confinement are analogous to the confinement of the electron wavefunction in quantum nanostructures. In fact, the terminology of electronic nanostructures can be used to describe their optical equivalent, namely photonic wells, photonic wires and photonic boxes. It is not only the terminology, however, that is communal - just as nanostructures have introduced exciting, new areas of device physics, microcavities offer a similar potential for optical device physics [15].

One principal motivation for reduced dimensional optical structures is the desire to modify the atom and vacuum field coupling, which produces spontaneous emission [11]. The ability to modify the spontaneous emission rate introduces an interesting new area of semiconductor physics in which the efficiency of LEDs can be greatly increased and in which a laser can have almost zero threshold current density. The key to altering the free-space spontaneous emission rate is to change the coupling between the atom and optical field. One possible method of accomplishing this aim is to place the emitter in an environment which alters the

density of electromagnetic modes [11, 168]. In particular, by placing the emitter in a cavity with dimensions on the size of the wavelength of the emission, spontaneous emission can be either enhanced or inhibited. It can be shown that the enhancement of spontaneous emission over the free space value is given by [169] :

$$f = \frac{3Q}{4\pi^2}\left(\frac{\lambda^3}{V}\right) \tag{6.1}$$

where f is commonly called the Purcell factor, Q is the quality factor of the cavity, λ is the wavelength and V is the volume of the cavity. One obvious manner in which to enhance the spontaneous emission is to have a small cavity - a microcavity. In order to obtain significant enhancements, however, a high-Q microcavity will also have to be used. A GaAs cavity with a volume of 1 μm^3 in which the active material emits at 1 μm needs Q≥565 for f>1; such a value of Q requires R>90%.

These two requirements have driven much of the research into microcavities in the last ten years [15]. The most common examples of semiconductor microcavities that have been investigated have been the Fabry-Perot microresonator (Fig. 6.1) and the microdisk laser (Fig. 6.2).

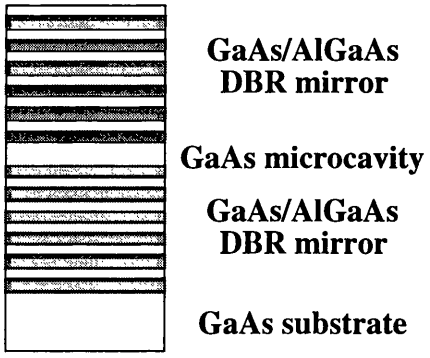

Fig. 6.1 Fabry-Perot microcavity.

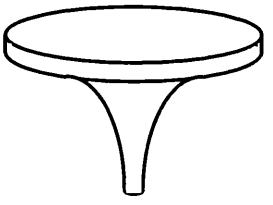

Fig. 6.2 Semiconductor microdisk.

The Fabry-Perot microcavity is simply a cavity of size λ/n with high reflectivity Bragg stack mirrors, typically R~99%. The high value of reflectivity gives a high Q cavity (see the section on Fabry-Perot theory in Chapter 2). Calculations have shown that the normalised spontaneous emission rate can be increased threefold in such a cavity for a specific polarisation [170]. However, the confinement on the length scale of the emission wavelength is only in one direction and, in order to obtain higher Purcell factors a device geometry needs to be found where there is confinement in two or three possible directions. It is highly likely that both epitaxial growth and nanolithographic techniques will be required in order to realise this goal. One possible candidate to provide confinement in the other two directions is the use of photonic bandgap structures, as these can incorporate 3-D cavities with high Q values and a volume on the order of several cubic half-wavelengths. Unfortunately, fabrication difficulties have so far inhibited the experimental demonstration of such a cavity.

Another candidate is a microdisk laser where the inhibition of spontaneous emission is more the key feature desired here [171]. These structures once again are very thin (typically of the order of $\lambda/2n$), but they do not use Bragg reflectors to confine the mode. The predominant modes in a microdisk structure are whispering gallery modes - modes which are confined by total internal reflection at the rim of the disk (Fig. 6.3). High values of Q can be obtained from microdisk lasers [172] and they have already demonstrated the control of spontaneous emission [173, 174].

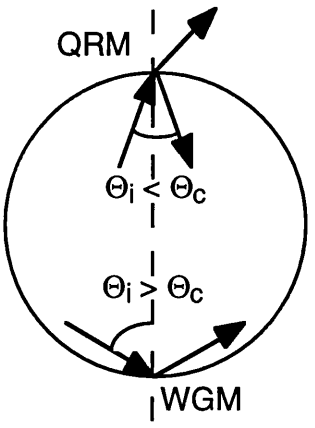

Fig. 6.3 Schematic showing whispering gallery modes (WGM) and quasi-radial modes (QRM) and the relation of these modes to the wavevectors in the disk; Θ_c is the critical angle.

The following microcavity experiments have been carried out in collaboration with D. Labilloy, H. Benisty and C. Weisbuch at the Ecole Polytéchnique, Palaiseau, France.

6.2 Disk-like microcavity with Bragg reflectors

In order to maximise any control of the emission process, cavities with smaller volumes are required. In increasingly smaller cavities, however, the Q-factor of the modes decreases and so the benefit of smaller cavities is lost. It is, therefore, important to consider methods by which the confinement can be increased. The particular example considered here is to surround an all-solid circular microcavity by a Bragg reflector based on PBG principles (Fig. 6.4). The Bragg reflector has a large κ value due to the interaction of the whole mode with the periodic structure as opposed to the shallow surface gratings that are commonly used to couple light out of circular semiconductor DBR lasers [175]. This additional confinement does not affect greatly the whispering gallery modes, but it will affect those modes which have a radial dependence (Fig. 6.5).

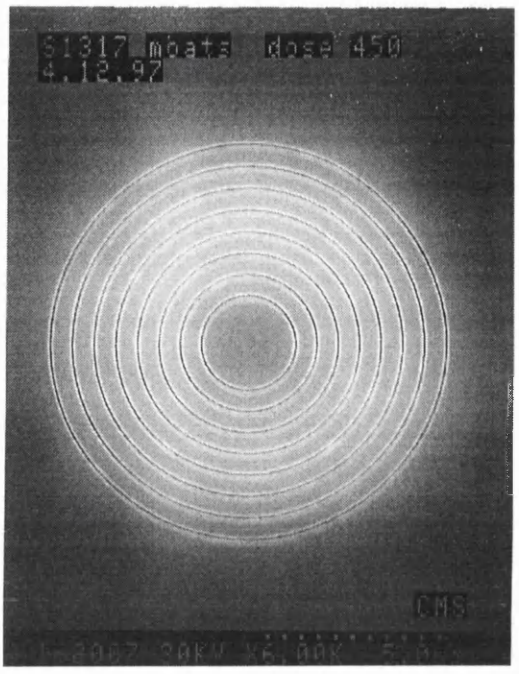

Fig. 6.4 SEM micrograph of circular microcavity with circular PBG mirrors.

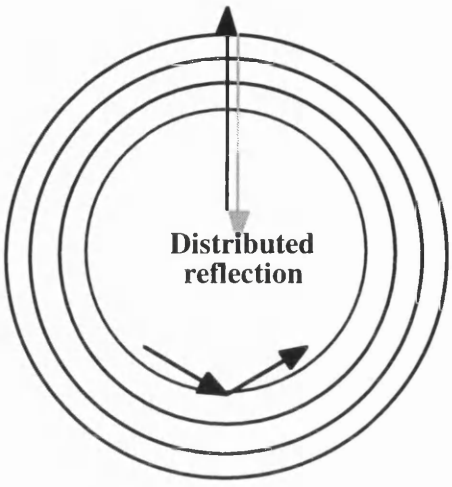

Fig. 6.5 Schematic indicating that the circular Bragg reflector will principally affect the radial modes.

Firstly, the theory of cylindrical cavities is introduced. The design and fabrication of actual cylindrical microcavities is then described followed by the experimental results and their analysis. Finally, conclusions about the possible application of these devices are made.

6.2.1 Cylindrical cavities - theory

In order to fully understand the mode structure of a cylindrical cavity, let us consider the cavity shown in Fig. 6.6. The allowed modes are found by solving the wave equation, taking into account the relevant boundary conditions; for this example it is assumed that the field is zero at the cavity walls as this represents a reasonable approximation. This is only a reasonable approximation for large cavities, but it represents the simplest mathematical case.

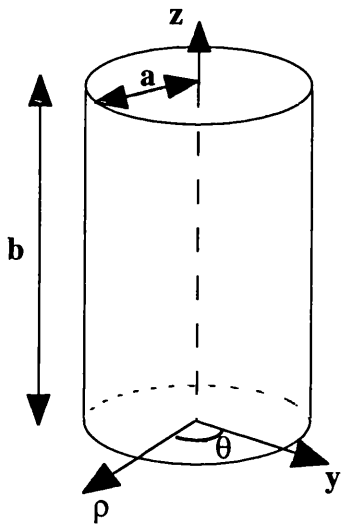

Fig. 6.6 Schematic of cylindrical cavity.

It is more sensible here to work in cylindrical rather than Cartesian co-ordinates, so the wave equation changes to :

$$\left(\frac{\partial^2}{\partial z^2}+\frac{1}{\rho^2}\frac{\partial^2}{\partial \vartheta^2}+\frac{1}{\rho}\frac{\partial}{\partial \rho}+\frac{\partial^2}{\partial \rho^2}+k^2\right)E=0 \tag{6.2}$$

The general solution is given by [115, 176]:

$$E=\sin(\alpha_1 z)J_m(\alpha_2 \rho)\cos(m\vartheta) \tag{6.3}$$

where $\alpha_1^2+\alpha_2^2=k^2$, $J_m(\alpha_2\rho)$ is the Bessel function of the mth order. The specific solution is determined by the application of the boundary conditions, which for TE waves are :

$$\begin{aligned} H_z|_{z=0} &= 0 \\ H_z|_{z=b} &= 0 \\ H_\rho|_{\rho=a} &= 0 \end{aligned} \tag{6.4}$$

These conditions give the following results:

$$\alpha_1=p\pi/b; \qquad \alpha_2=\chi_{mn}/a$$

where p is an arbitrary integer and $\chi_{m,n}$ represents the zeros of the Bessel function with the notation for the argument means the nth zero of the mth Bessel function.

Therefore, the values for the components of the electromagnetic field are:

$$\begin{aligned} E_z &= 0, \\ E_\rho &= ik\left(\frac{\mu}{\varepsilon}\right)^{1/2}\frac{m}{\rho}\sin(\alpha_1 z)J_m(\alpha_2\rho)\sin(m\vartheta), \\ E_\vartheta &= ik\left(\frac{\mu}{\varepsilon}\right)^{1/2}\alpha_2\sin(\alpha_1 z)J_m'(\alpha_2\rho)\cos(m\vartheta), \\ H_z &= -\alpha_2^2\sin(\alpha_1 z)J_m(\alpha_2\rho)\cos(m\vartheta), \\ H_\rho &= -\alpha_1\alpha_2\cos(\alpha_1 z)J_m'(\alpha_2\rho)\cos(m\vartheta), \\ H_\vartheta &= \frac{m\alpha_1}{\rho}\cos(\alpha_1 z)J_m(\alpha_2\rho)\sin(m\vartheta) \end{aligned} \tag{6.5}$$

The eigenvalues are given by the zeros of the Bessel function. Therefore, the cut-off wavelengths for each mode are given by:

$$\lambda_{mn} = 2\pi na/\chi_{m,n} \tag{6.6}$$

Similar expressions for the electromagnetic field components are obtained for TM polarisation also.

6.2.2 Design and implementation

The principal design of the circular microstructure follows that of a Bragg grating. The experimental measurement technique must also be considered in the design of the structure, since the excitation spot has an area of approximately 9 μm^2.

The circular Bragg grating acts both to provide distributed reflection and also to couple light coherently out of the waveguide. In order to coherently couple light out of the wavguide the wavevectors in the grating region and the emitted (or incident) beam must be matched. The phase matching condition leads to the following formula:

$$k_a \sin\vartheta = \beta_0 + \left(\frac{2m\pi}{\Lambda}\right) \tag{6.7}$$

where k_a is the wavevector in air, θ is the emission angle, β_0 is the propagation constant, m is the grating order and Λ is the period. For normal incidence, $\theta=0°$, and the equation reduces to:

$$\Lambda = m\lambda_0 / n_{eff} \tag{6.8}$$

In the case under question, $\lambda=1$ μm and $n_{eff}=3.4$, so the solutions are $\Lambda=m*0.294$ μm. We chose m=2, as it corresponds to a fourth order in-plane grating, which provides the necessary optical confinement. Once again, we use narrow gaps following the arguments outlined in §5.1. The inner diameter of the disks was chosen to be equal to 5Λ, where Λ is the grating period (Λ= 580, 600, 620 and 640 nm). This diameter represents the smallest focal spot that can be obtained with the experimental set-up and also ensures that the PL signal from the quantum dots is not destroyed by the etch damage.

The circular microcavities were fabricated by myself and Dr. T. Krauss using the process outlined in Chapter 3, namely electron-beam generated patterns were

transferred into a thin film of silica and finally into the GaAs/AlGaAs heterostructure to a depth of 0.8 μm. The heterostructure used in these experiments was identical to that used in the previous chapter (Fig. 5.4). The measurement probes the cavity resonances by the photoexcitation of InAs quantum dots inside the microcavity as described previously. These measurements were carried out by D. Labilloy at the Ecole Polytechnique, Palaiseau, France.

6.2.3 Results

The principal result is the observation of several sharp peaks with a spectral width in the range $\Delta\lambda$=1.5-5 nm (Fig. 6.7), corresponding to Q factors between 200 and 650. These sharp spectral features are in contrast to the broad features that are observed in disks of 3 μm radius with no Bragg reflector (inset in Fig. 6.7). These sharp peaks are, therefore, attributable to the addition of the Bragg reflector to the resonator.

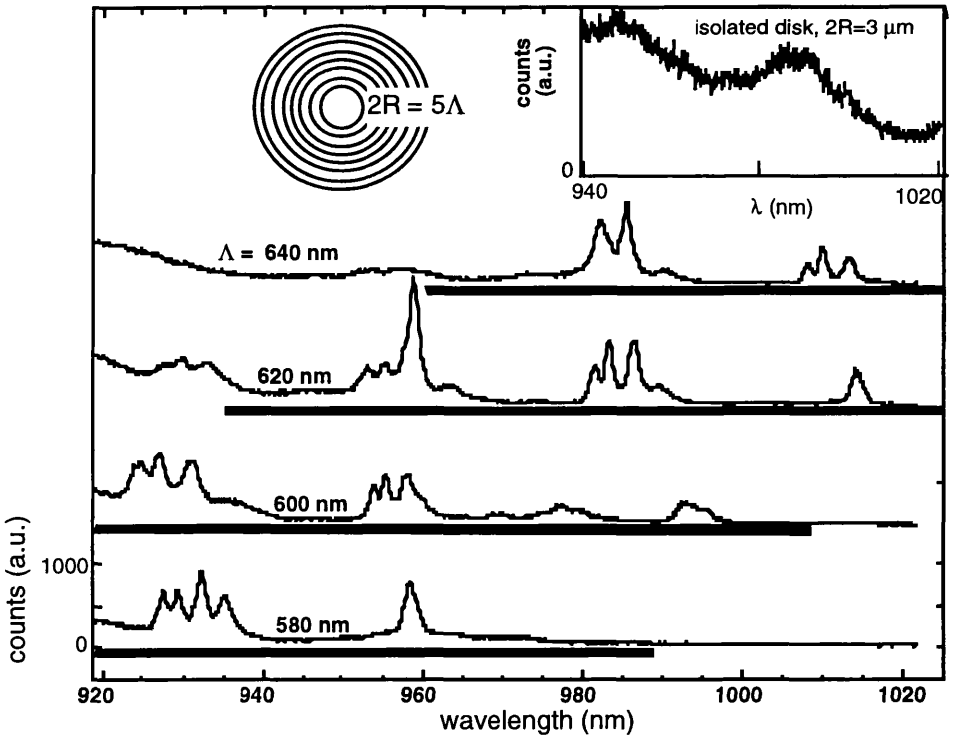

Fig. 6.7 Spectra for different disk diameters; inset shows signal collected from a circular cavity without the Bragg reflectors.

If a cross-section is taken through the disk then the circular Bragg resonator can be approximated as a multilayer stack (Fig. 6.8) and the appropriate theory can be used to calculate the stopband. This approach assumes normal incidence at the disk boundaries, the trench refractive index is that of air and the refractive index of the semiconductor ridges is equal to the effective index, n_{eff}. The resulting stopbands as calculated by H. Benisty are shown in Fig. 6.7 by the dark lines. This analysis shows that sharp peaks are only observed in the grating stopband, as the peaks disappear at short wavelength for a grating period of 640 nm and also at higher wavelengths for Λ=580 nm, namely outside the stop-bands. It is clear, therefore, that the addition of a Bragg reflector, which gives higher cavity mirror reflectivities, produces well defined modes.

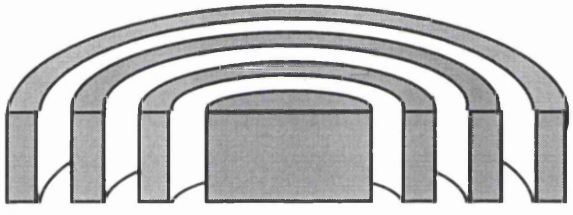

Fig. 6.8 Microdisk with circular Bragg reflector viewed in perspective.

Another interesting observation is that the peaks occur in groups, which are spaced by between 27 and 33 nm. This spectral distance corresponds to the free-spectral range of a disk of approximately 3 μm diameter. The analysis of the spectral features is based on the theory in §6.2.1 and the specific details of these microdisks have already been reported [111]. The calculated spectrum is shown in Fig. 6.9 along with an experimentally measured spectrum indicating the good agreement obtained.

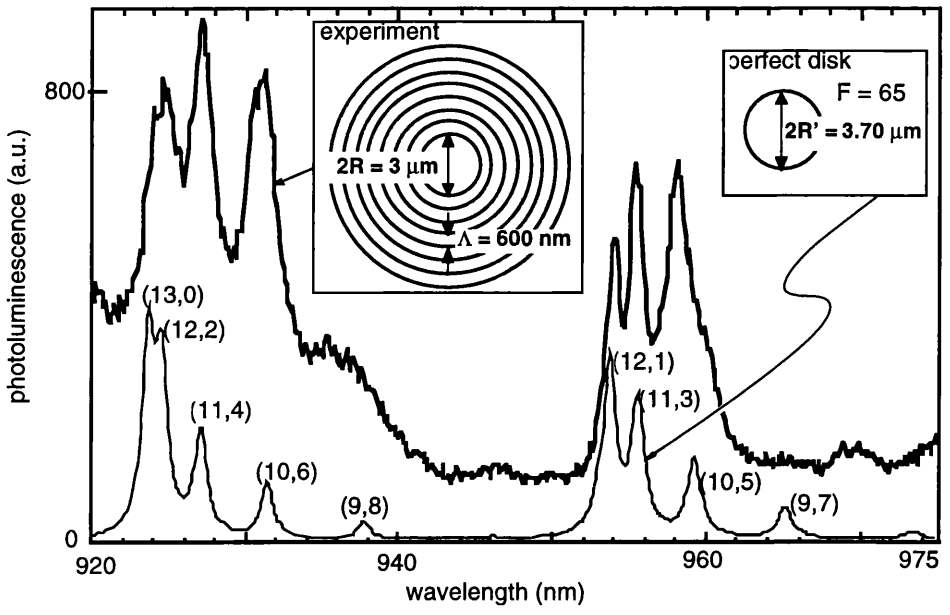

Fig. 6.9 Calculated cavity mode peaks and the experimentally measured peaks for R=3 μm and Λ=600 nm.

We can therefore conclude that circular Bragg reflectors can be used to confine in-plane quasiradial modes in cylindrical cavities of approximately 3 μm diameter. The grating reflectivity is calculated to be greater than 90%, leading to modal linewidths as high as 650. An analytical model of the cavities has been developed by colleagues and a good agreement has been observed between this model and the measured results. This geometry is an interesting solution to lateral light confinement with the potential for spontaneous emission control.

6.3 One dimensional microcavity defined by 2-D PBG mirrors

Fabry-Perot microcavities have already been shown to produce modified spontaneous emission behaviour, even with confinement in just one direction [170]. Recent results, however, on three-dimensional pillar microcavities have produced Purcell factors of up to 5 by using quantum dot emission at cryogenic temperatures [177]. However, future devices based on pillar microcavities will possess some intrinsic disadvantages including difficulties in fabrication, the problem of achieving room temperature electroluminescence, increased surface recombination at the etched surfaces and lack of confinement in the guiding plane. One possible method to address this last problem is to use photonic microstructures [111] with 1D in-plane microcavities with photonic bandgap mirrors having already been demonstrated [93, 101, 102].

In addition to being important in future devices, microcavities offers an elegant way to measure the optical properties of PBG structures. In particular, the reflectivity, transmission and losses of a PBG mirror can be determined easily. This ease in quantification is in contrast to the difficulty in directly evaluating the reflectivity, R, and transmission, T, for such a structure as either R or T tend to be close to unity or very small. A planar Fabry-Perot microcavity also allows the losses, both of the mirror and the cavity, to be determined. The accurate determination of the losses is important as they ultimately determine the number of bends and functionalities that can be cascaded for a given power budget.

The design, fabrication and method of characterisation will be first introduced followed by the results and their analysis. The results will raise some problems with these microcavities, particularly the 30% cavity losses, but the key conclusion is that they still offer great potential for increased optical confinement in future devices.

6.3.1 Design and implementation

The basic principles of using a Fabry-Perot cavity with 2D PBG boundaries have already been demonstrated for 3 μm long cavities in previous experiments [101]. In these experiments, light propagation was along the ΓK direction. The problem with propagation along ΓK is in-plane diffraction which leads to a limited reflectivity of 80% [104]. Here, the lattice constant, denoted a, was chosen as 220 nm and the air filling factor as 30%. These parameters yield a complete gap in the TE polarisation for the wavelength range 890 - 1120 nm [104]. The ΓM orientation was chosen (Fig. 6.10) because it does not lead to in-plane diffraction in the chosen range of lattice parameters. The cavity spacings, L_c, were calculated with a one-dimensional multilayer model assuming alternating layers of air and semiconductor ($n = n_{eff} = 3.32$), with 30% air filling-factor.

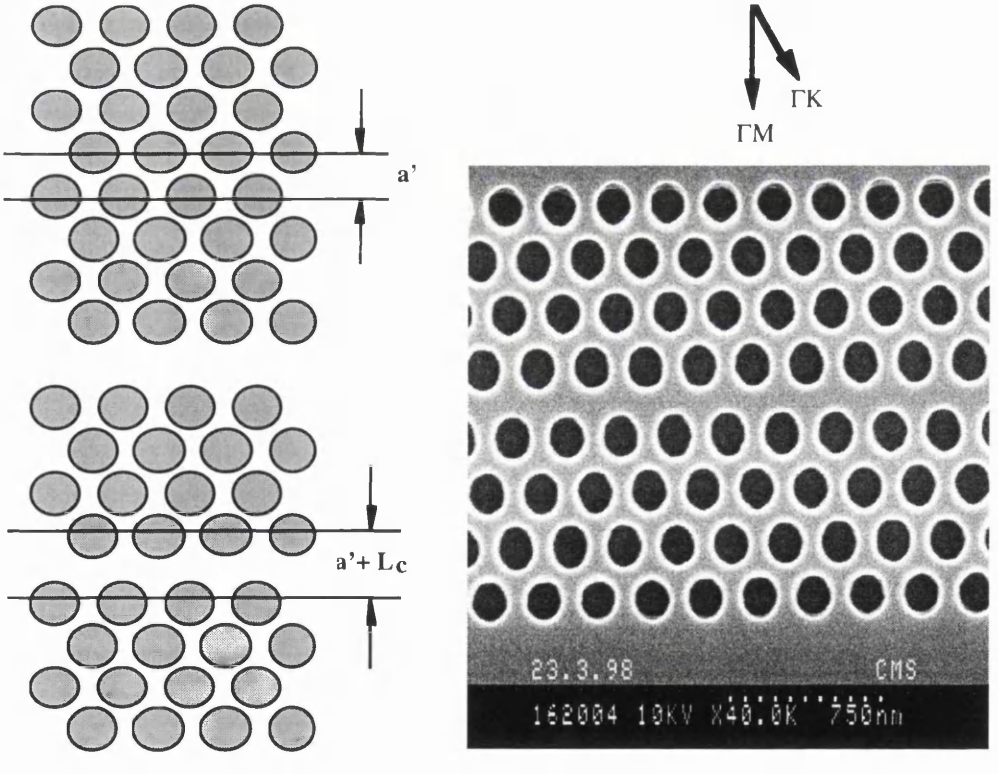

Fig. 6.10 Sketch and SEM micrograph of 1D Fabry-Perot microcavity defined by 2D PBG mirrors; a is the period and L_c the cavity length (spacing).

The calculations gave the first mode in the middle of the stop-band for $L_c = 70nm$, the second for $L_c = 190$ nm and the third for $L_c = 340$ nm. Notice that these are not the usual "quarter wave" multiples that are found in DBR mirror stacks. Notice also that the first of these modes already has an order $m > 1$ due to the penetration depth of the cavity field into the PBG mirrors. Several cavity spacings, ranging from 40 nm to 400 nm, in 10 - 20 nm steps were used to measure this dependence. Each of the PBG mirrors had 4 rows of air holes. Single patterns of 4 and 8 rows were also included so as to compare the transmission of one of the in-plane "mirrors" with that of the cavities.

The PBG defined microcavities were fabricated using the techniques outlined in Chapter 3 in a heterostructure identical to that used in the other experiments (Fig. 5.4) using the experimental set-up outlined in the previous chapter.

6.3.2 Results and discussion

The dependence of the resonance wavelength on the cavity spacing was examined first. Fig. 6.11 shows the results for cavity spacings of 320, 340, 360 and 380 nm with corresponding peak transmission values at 930, 955, 980 and 1005 nm; results for the shorter cavities do not exhibit this constant spectral shift with increase in cavity spacing, indicative of a change in the penetration depth for small cavity spacings. The oscillations in the spectra are due to the much larger cavity (20–100 μm) formed between one of the mirrors and the cleaved edge. The constant shift in the resonance wavelength for the different cavity lengths suggests a constant penetration depth into the PBG mirrors, an effect expected in the middle of the photonic bandgap. The 30% normalised transmission for all cavity lengths is a clear indication of cavity effects. These results take account of the absorption in the cavity, α, which must in part be the reason for the less than 100% transmission at resonance.

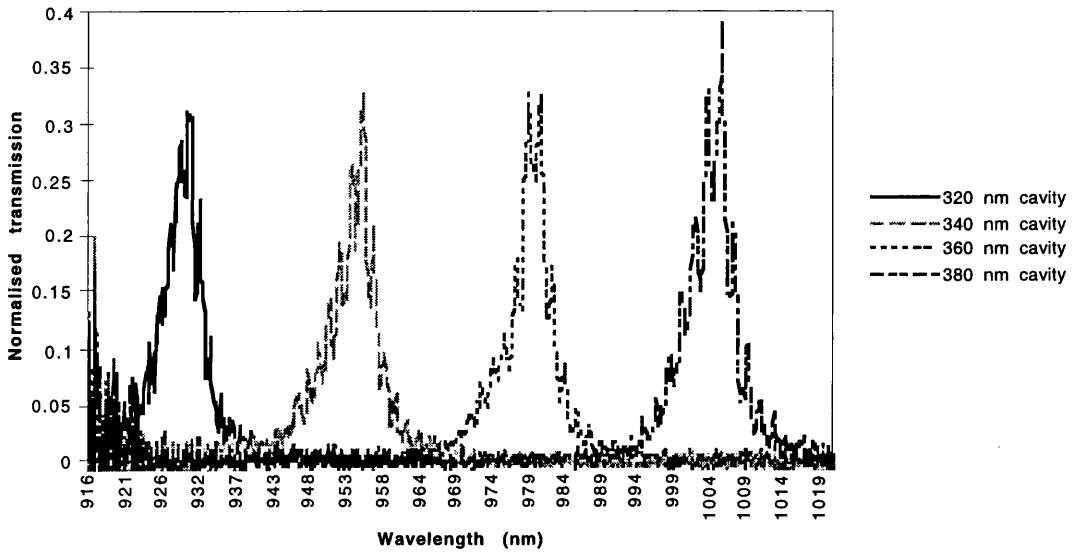

Fig. 6.11 Constant shift in spectral position of cavities' resonance for a constant change in cavity length.

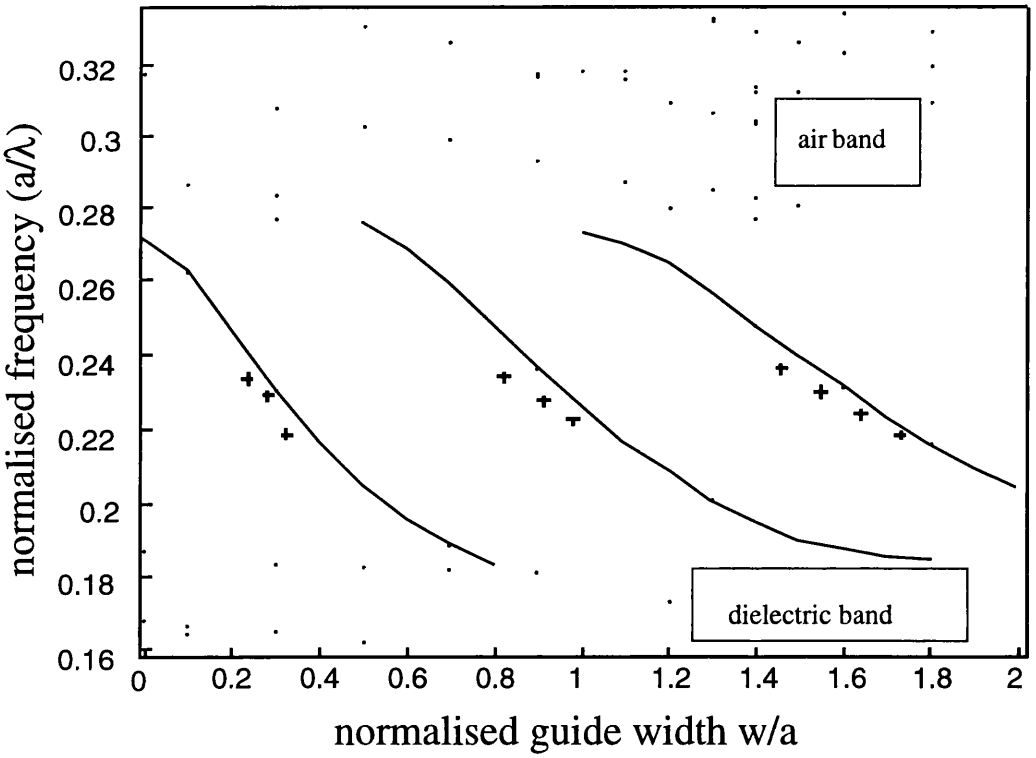

Fig. 6.12 Calculated bandstructure indicating spectral position of defect modes. The experimental points (+) agree well with the calculated values.

These experimental results were compared with a theoretical estimate of cavity mode frequencies and eigenmodes using a supercell ansatz of the plane-wave method [124]. The calculations are made for a dielectric permittivity of 11.0 and an air filling factor of 28.5%. As can be seen from Fig. 6.12, the calculated values for the spectral position of the mode agree well with those observed experimentally.[18] The examination of the eigenmodes (two-dimensional field maps) allow the magnitude of the penetration depth to be calculated from field plots (Fig. 6.13). The penetration depth is estimated to be about 0.25 μm from the 1/e points of the mode, which means that the lowest possible order of cavity is two. This is illustrated in Fig. 6.13 for the case of a spacing of L_c = 70 nm (normalised guide width = L_c / a = 0.318). The topographical images of the electric flux density, **D**, (top) graphically represent the distribution of the field in the PBG lattice. The bottom plot represents a corresponding one-dimensional average of the field along the cavity. These plots clearly demonstrate how light is distributed at different frequencies. More specifically, the left-hand field plot is associated with the dielectric band, as shown in Fig. 6.12, as the electric field tends to overlap with the dielectric as much as possible, whereas the right-hand figure is the air band, the electric field being mainly in the air. This redistribution of light between high and low material is a sign of bandgap behaviour. The middle figure represent the case of a defect mode whose normalised frequency (a/λ) lies in the middle of the photonic bandgap and so represents a non-propagating mode or a bound state. Therefore the defect (cavity) mode forms a standing wave pattern, which is shown in the plot by the field distribution which is strongly peaked in the cavity centre, with little light found in the PBG lattice, and the periodic decay of the field into the PBG lattice.

[18] Only 270 plane waves were used in the calculation resulting in a limited spatial resolution and overestimated frequencies as seen in Fig 6.12.

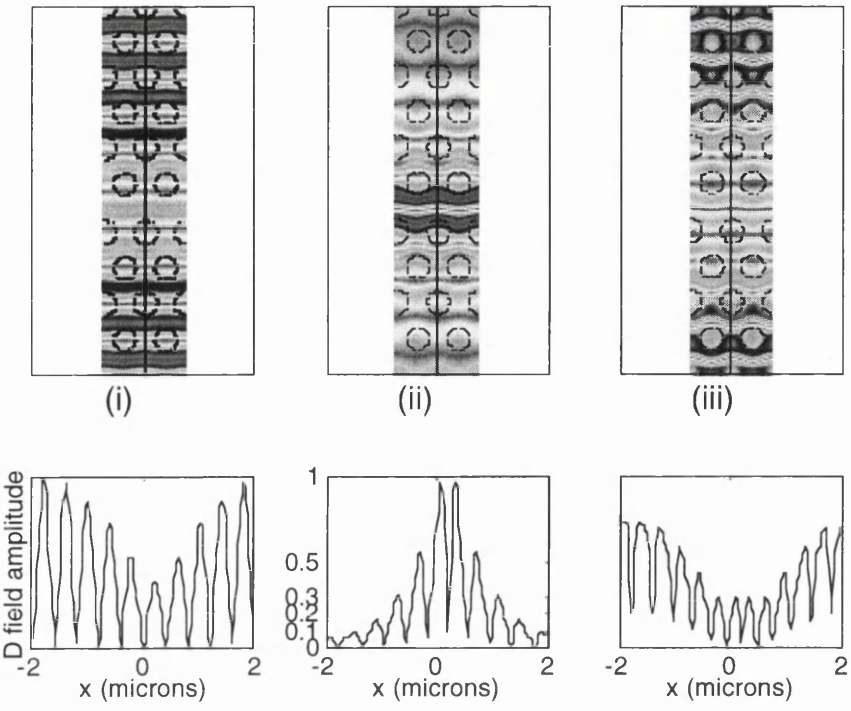

Fig. 6.13 Topographical representation of the electric flux density, D, (top) and a plot of the field modulus across the cavity (below), as indicated by the vertical line in the top figures for three normalised frequencies and a constant normalised guide width of 0.318: (i) field in dielectric band (L_c/a=0.1829), (ii) field in the confined cavity mode (L_c/a=0.2274) and (iii) field distribution in the air band (L_c/a=0.2767).

The minimum in-plane cavity order, as defined above, has been calculated to be m=2 due to the finite penetration depth of the field into the PBG mirrors. The calculated value from experimental data for cavity lengths between 40 and 90 nm, assuming a refractive index of 3.2, is between 2.7 and 3.4. The effective index, however, is slightly smaller due to the finite penetration of the field into the air holes. Fig. 6.14 shows the transmission of a cavity of only 70 nm spacing. It has an 8 nm half-width, which gives a quality factor of 125. This quality factor translates into an effective finesse of 63 and to a mirror reflectivity of 95%, so the losses are less than 5%. The individual factors contributing to this loss have not

been identified, but principal causes will be radiation into the substrate and absorption in the active layer. This value for the loss is low but could be further improved by providing greater optical confinement in the vertical direction by means of a vertical mirror stack or by using a lower index cladding.

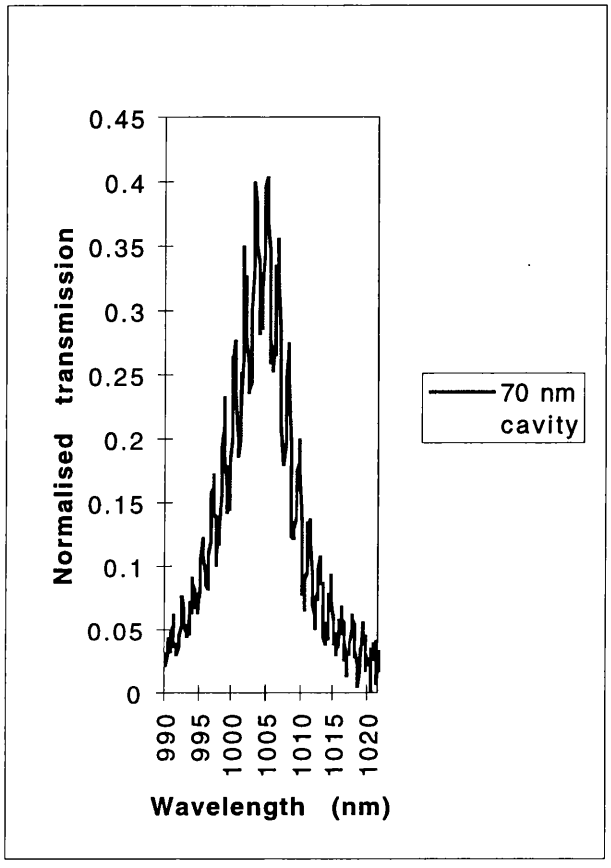

Fig. 6.14 Cavity mode for a 70 nm cavity spacing for 4 row PBG mirrors, which have a 220 nm period. The half-width is 8 nm which yields an estimated reflectivity of 95%.

In conclusion, one dimensional microcavities with a 2 μm cavity length, bounded by 4 rows of 2D PBG mirrors, have been realised down to 40 - 70 nm cavity spacings and have shown excellent resonant properties. Estimated reflectivities in excess of 90% have been calculated for cavity spacings as small as 40 nm, with a resonance half-width as small as 8 nm. At the same time, the weak but non-zero

losses indicated by the results show that the issue of losses still needs to be addressed. Constant shifts in cavity position for constant change in cavity length have been shown, indicating the good properties of the PBG mirrors in the region of constant penetration depth and indicating that the deterministic placement of a cavity mode is a reasonable task for applications, such as narrowband filters. A large variety of useful defect configurations remains to be explored. Future work on defects with strongly directional behaviour as well as frequency selectivity and specific polarisation characteristics will highlight the much richer possibilities provided within a 2D PBG structure environment, as compared with 1D structures.

6.4 Two-dimensional microcavities with 2D photonic bandgap structures

The logical progression from the previous experiments was to look at two-dimensional resonators with 2D photonic bandgap boundaries. The geometry of the resonator is somewhat dictated by the photonic lattice chosen, as shown in Fig. 6.15 whereby a triangular lattice naturally produces a hexagonal cavity and a square lattice produces a square resonator. All of the previous experiments were performed on triangular lattice structures, as they offer the largest absolute bandgap for holes in semiconductor and so they are more fully characterised and understood. Also, a hexagon represents the polygon with the most number of sides that can be perfectly tiled on a planar surface. Therefore, 2D hexagonal cavities with a 2D array of triangular holes were chosen for this investigation.

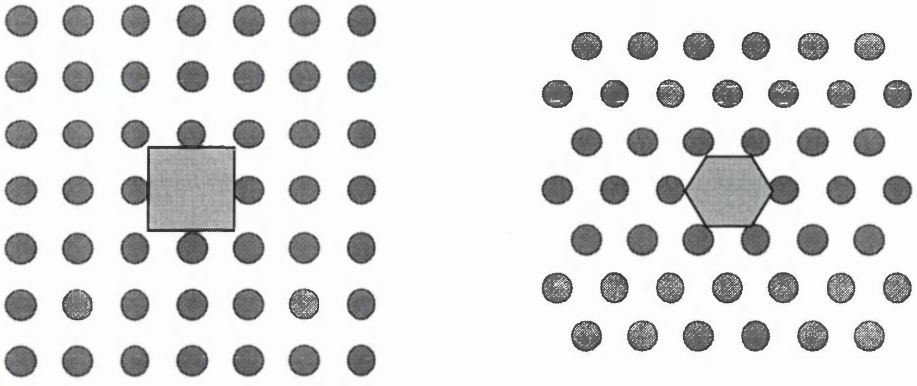

Fig. 6.15 Connection between lattice and cavity geometry.

First, I will discuss the cavity layout and then show some preliminary results. Some simulations are shown, which attempt to explain the observed results.

6.4.1 Cavity layout and implementation

Different sized cavities were examined, the smallest of which was formed by removing 19 holes from the centre of a uniform PBG structure and the largest cavity had 126 missing holes (Fig. 6.16). As with the experiments of the circular microcavities, grating couplers were included to scatter the light coherently into the air towards the detector. Two different couplers were used, one of which was orientated along the ΓK symmetry direction, 2R, (Fig. 6.17a) and the other along the ΓM symmetry direction, 3R, (Fig. 6.17b). Each cavity was surrounded by 12 rows of holes since this number of rows is sufficient to ensure highly reflective boundaries and thus a high Q cavity (Fig. 6.16). It should be noted that not all the cavities were perfect hexagons, but all cavities had six-fold rotational symmetry. The usual strategy of using different periods for the PBG structure was also utilised in this experiment in order to examine the effect of the position of the grating stopband on the mode resonances. In this instance, three different periods were used, Λ=220, 240 and 260 nm, these periods giving a TE stopband for a normalised radius of r=0.3Λ at the emission wavelengths used here.

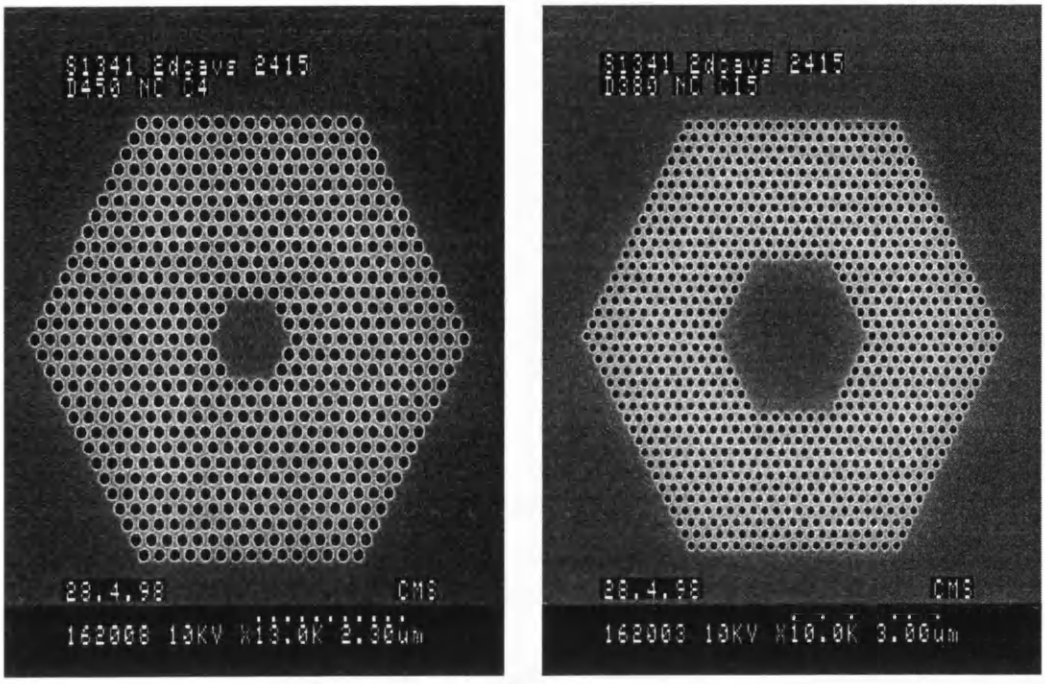

Fig. 6.16 SEM micrographs of a) smallest and b) largest hexagonal cavities.

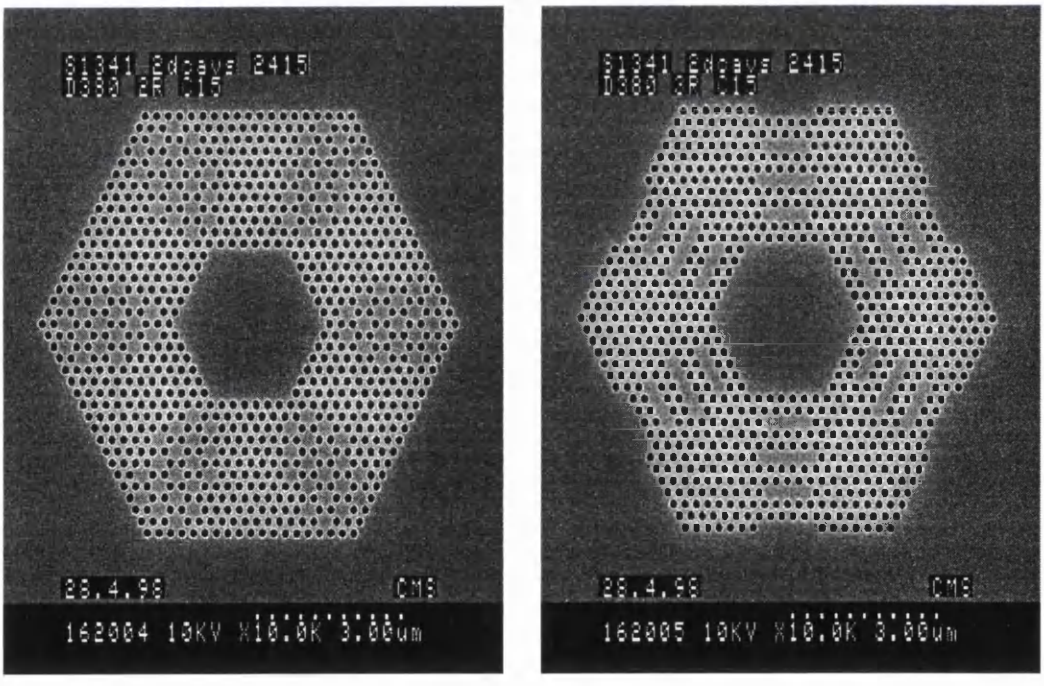

Fig. 6.17 2D grating coupler along a) GK and b) GM crystallographic directions.

These microcavities were fabricated in a similar GaAs/AlGaAs waveguide structure as used previously. Quantum dots were preferred to quantum wells in this application because of the increased localisation of the carriers and a reduced surface recombination rate, which is the main reason for the degradation of the PL signal near the etched surfaces. In quantum well devices the high surface recombination rate, due to the ease of carrier migration to the etched surfaces and the short diffusion distances involved, would result in a very low PL signal. The devices were fabricated and measured using the methods described earlier.

6.4.2 Results and discussion

The collation of all the results for a PBG period of 220 nm is shown in Fig. 6.18; Fig. 6.19 shows the variety of cavities used in these experiments. It is apparent that there are no obvious clusters of sharp peaks separated by a constant spectral distance as was the case for the circular microcavities [111]. However, there are some interesting features. The first important features are the sharp peaks in some of the spectra, particularly for the larger cavities, $\Delta\lambda \approx 1\text{-}2$ nm ($Q \approx 500\text{-}1000$). These spectral widths are indicative of high reflectivities, certainly greater than 90%, which shows that the 2D PBG structure is confining the field just as well as the circular microcavity.

Another feature is the progression of some of the resonance wavelengths to higher wavelengths as the size of the cavities is increased, as would be intuitively expected. Therefore, some of the general features that were observed in circular microcavities may also be present in the hexagonal cavities currently under study.

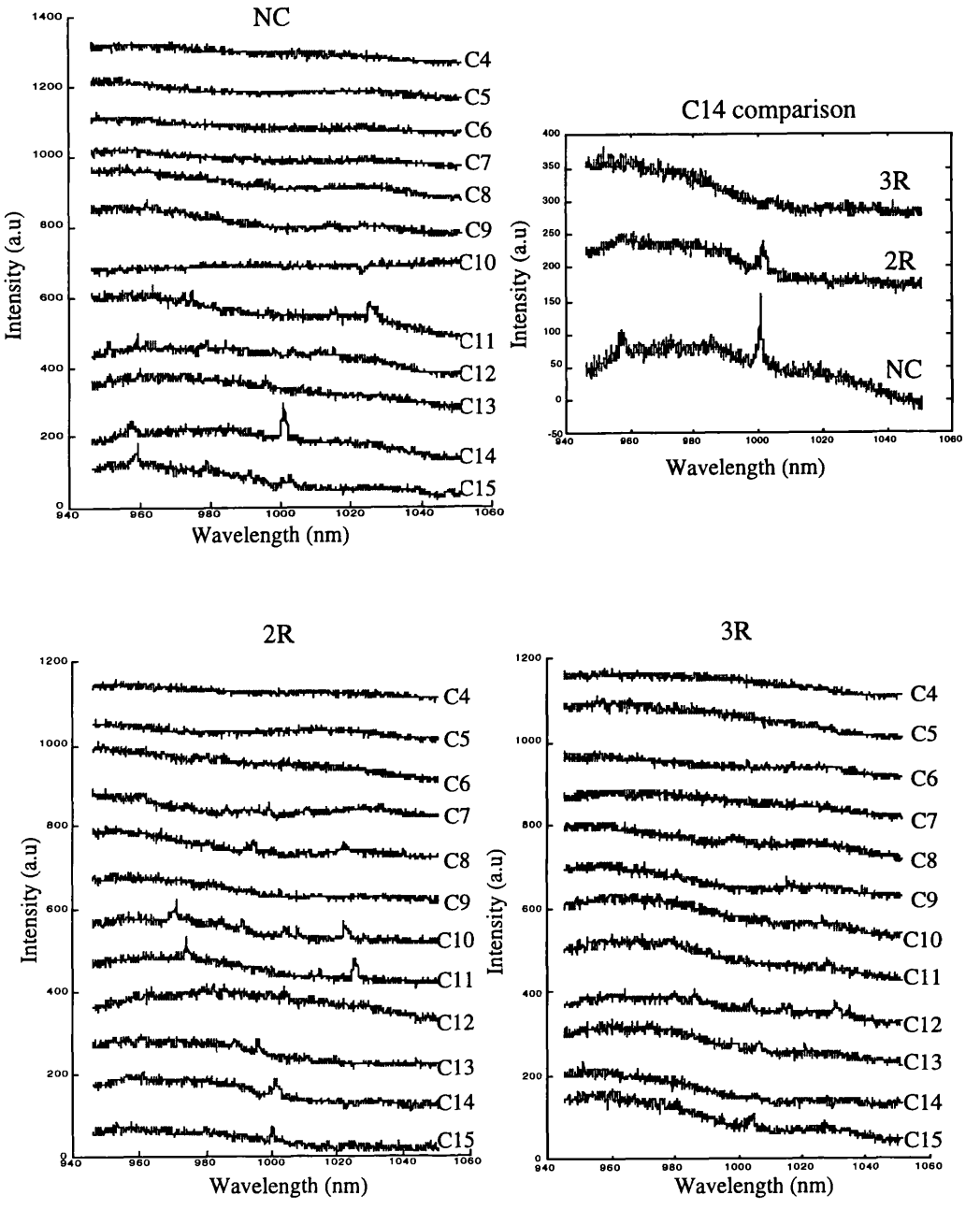

Fig. 6.18 Collation of spectra for different cavities and couplers for 220 nm PBG period. The top right figure is an expanded comparison of the different couplers for the cavity C14 (NC=no coupler, 2R=ΓK coupler, 3R=ΓM coupler).

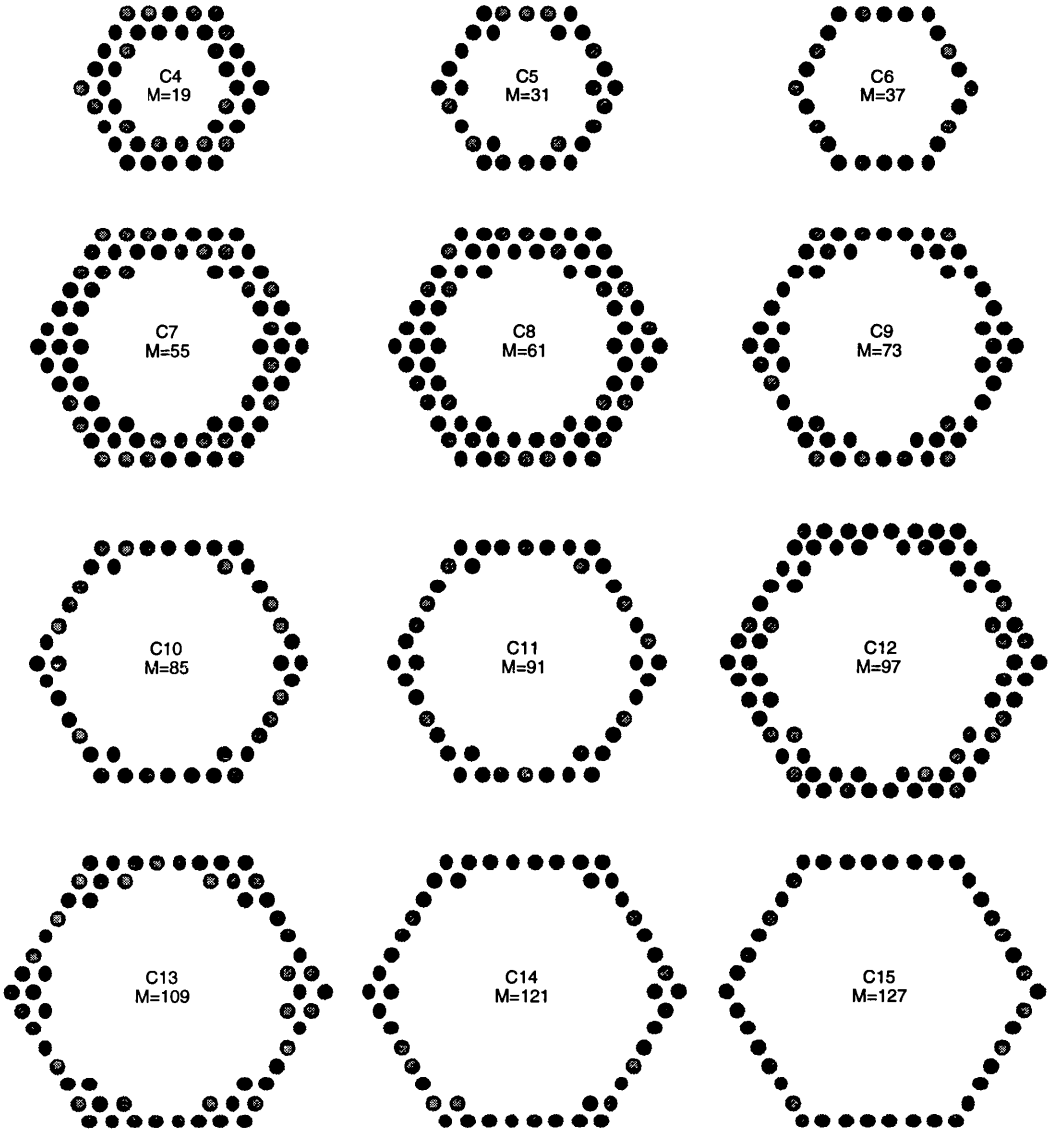

Fig. 6.19 Schematic demonstrating the nomenclature used in Fig. 6.18.

The fidelity of the measurement technique is born out by the fact that many of the spectral features are reproduced for two different boundaries, namely PBG boundaries with and without grating couplers. However, this observation does raise the significant question of how the light was scattered into air from the cavity with only a PBG structure mirror, i.e. no grating coupler. One possible explanation is that the scattering generated by the PBG structure itself was capable of scattering light out of the guiding plane into the air. This hypothesis once again raises the important issue of losses at PBG interfaces and may in part explain why

no sharp spectral features are observed for smaller cavities where the losses become more significant.

Clearer results are obtained for a PBG period of 240 nm (Fig. 6.20). This period corresponds to the middle of the photonic bandgap for TE polarisation and a period where there exists a stopband in TM polarisation for ΓK . The spectral features are clearer and the spectral widths vary in the range $\Delta\lambda \approx 1$-5 nm, which gives Q values up to 1000. All the features discussed above are also observed for this period, but the background is significantly lower for all cavities above C8. It is not clear why the background should be lower for this period, but it could be that the increased confinement provided by having a TM bandgap for the ΓK symmetry direction has a profound effect on confining the cavity modes. This observation is substantiated by the similarity between the NC and 2R spectra - 2R being the coupler along the ΓK direction. It could be that the out-of-plane scattering arises solely from the ΓK symmetry direction but this hypothesis still remains to be tested.

The analysis of hexagonal cavities is difficult to perform analytically as the natural axes of these cavities are non-orthogonal, which complicates the problem. However, the field distributions can be solved numerically. Initial simulations[19] have shown that the field patterns for a hexagonal cavity are more complicated than for the circular case (Fig. 6.21). There is evidence for some form of whispering gallery modes, but some of the mode shapes clearly reflect the hexagonal symmetry of the cavity. At present, there are many unanswered questions about these cavities and further work is required. Specifically, it would be beneficial to look at cavity resonances through lateral detection, i.e. use the cleaved edge detection method. This work will require a redesign of the sample layout and further measurements. Also, a theoretical model will need to be developed with

[19] Simluations have been carried out by H. Benisty at Ecole Polytéchnique, Palaiseau, France.

which to analyse these results, so that design models for future devices can be constructed.

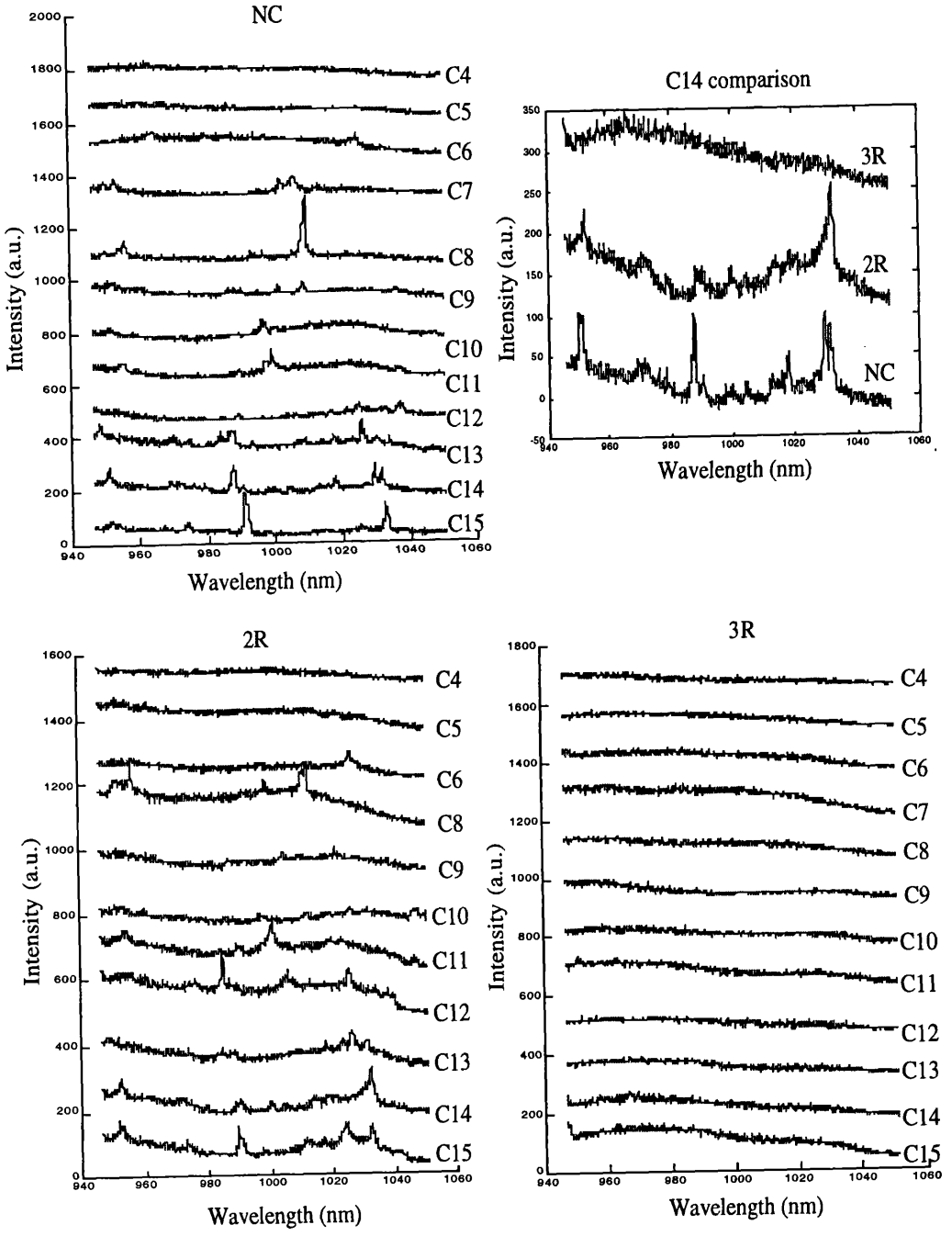

Fig. 6.20 Collation of results for 240 nm PBG period cavities. The top right figure is an expanded comparison of the different couplers for the cavity C14 (NC=no coupler, 2R=ΓK coupler, 3R=ΓM coupler).

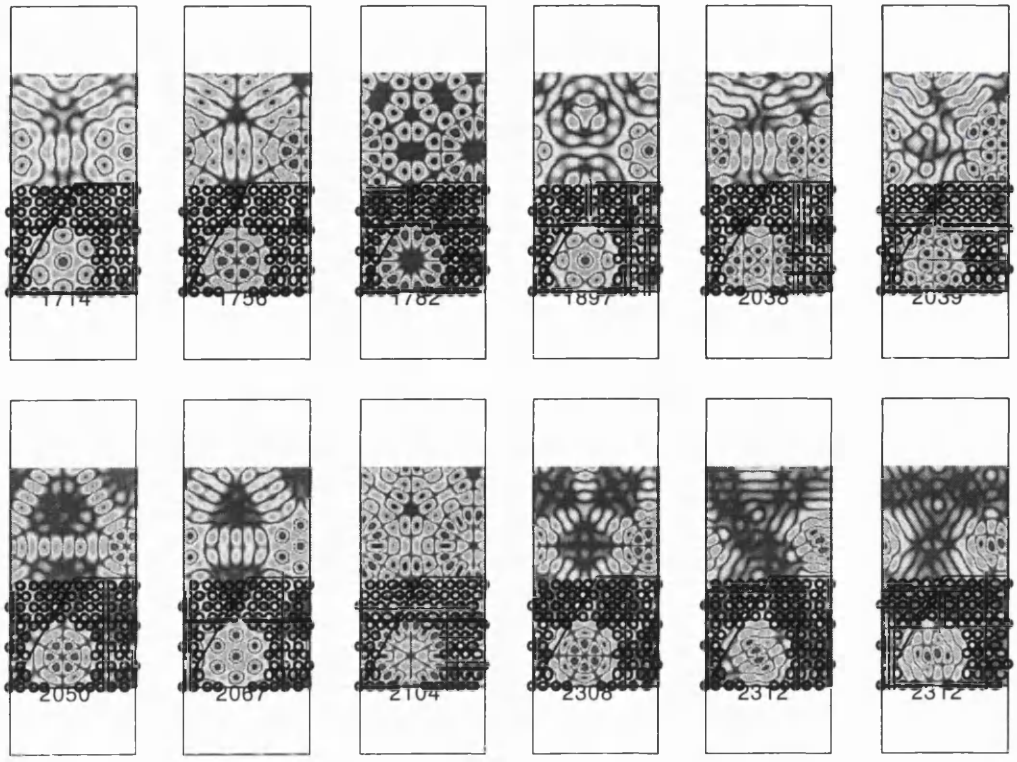

Fig. 6.21 Calculated magnetic field distribution in a hexagonal cavity for various frequencies (courtesy of H. Benisty).

In conclusion, hexagonal microcavities as small as 2.3 μm^2 with boundaries consisting of 12 rows of triangular holes have been fabricated and tested. Sharp spectral features are observed with spectral widths, $1nm \leq \Delta\lambda \leq 5$ nm ($1000 \geq Q \geq 200$), consistent with estimated reflectivities of over 90%. Some similarities between these hexagonal cavities and circular cavities are observed, but the 2D PBG boundaries and the cavity symmetry complicate the analysis of experimental results. Further research to investigate these structures in more detail is currently being planned.

6.5 Conclusions

The motivation for investigating microcavities is clear. The desire to control the emission process and to design more efficient and novel light emitting sources could bring great advances in many fields of application. Two versions of lateral confinement have been investigated and both of these approaches have shown high reflectivity and high Q values in cavities with lengths as small as 40 nm. These results indicate that photonic crystals can provide the necessary reflectivities for microcavities to control the emission process. To date, however, no results have yet been obtained which show a modification of the spontaneous emission rate. The failure to demonstrate the desired effects is due largely to the significant engineering problems associated with the application of photonic bandgap structures as high-reflectivity mirrors in microcavities. Further experiments will, therefore, be required to address these problems.

7. Future Work

This project has raised many issues over diverse fields of research. However, these matters can be classified into two general categories - fabrication and device physics. The key fabrication issues are the production of more uniform, deeper structures with greater ease. Improvements could be made in the electron-beam lithography process, for example replacing dose tests with simulations and applying correction algorithms to patterns. Another important issue is the throughput of the machine and the machine time issue could be overcome by using resists that are more sensitive.

In the GaAs/AlGaAs material system, future work should be concerned principally with investigating the limits of steam oxidised AlAs masks. However, for the InP-based material system, the key aim is to establish reliable etching technology which is capable of producing PBG structures in all possible InP-based materials.

The developments in device physics that are required relate primarily to a more detailed investigation of the loss mechanisms in microcavities bounded by PBG structures and the application of this knowledge to improved cavity design. Alternative confinement ideas, however, will be examined with particular reference to controlling the out-of-plane emission. Moreover, alternative characterisation methods with higher resolution, to characterise small cavities, will also be explored. The most important task, however, remains the production of electroluminscent devices. Some of the several serious problems associated with electroluminscence will be detailed.

7.1 Electron-beam lithography

The current method for determining the correct dose for any particular pattern is based on linear interpolation of experimental results. Generally, the experimental data takes the form of a dose test, i.e. an approach where the pattern is written several times at different doses with all the patterns being developed at the same time for a defined period of time. This method is both time consuming from the point of view of machine time and also because this technique often requires SEM examination of the patterns after development, as the features are typically smaller than the resolution of optical microscopes. An extremely useful addition to the current laboratory set-up would be an exposure and development simulation package. Such software would eliminate the need for most dose tests and improve the accuracy with which the patterns are produced. Moreover, it would allow a smaller dose range to be selected when actual devices are being fabricated, which would allow greater reproducibility between different samples. The addition of modelling software, however, would not remove the need completely for dose tests, as the model does not eliminate errors such as variable resist thickness and variable development conditions.

The accurate and reproducible generation of feature sizes is particularly important in photonic bandgap structures as any fluctuations translate directly into measurable variations in the photonic bandgap. One particular problem that is commonly observed in electron-beam generated patterns is a variation of the feature size across a pattern (Fig. 7.1). This variation arises because of back-scattered electrons from the substrate during writing, which results in the indirect exposure of areas onto which the electron beam was not directly incident. The indirect exposure of the PMMA erodes the pattern resolution since it reduces the contrast between the exposed and unexposed areas of the resist. The background level is not constant across patterns, however, and is a function of the pattern

density. The background level decreases towards the edges of the patterns, as there are progressively fewer features which can contribute to the indirect exposure of the resist.

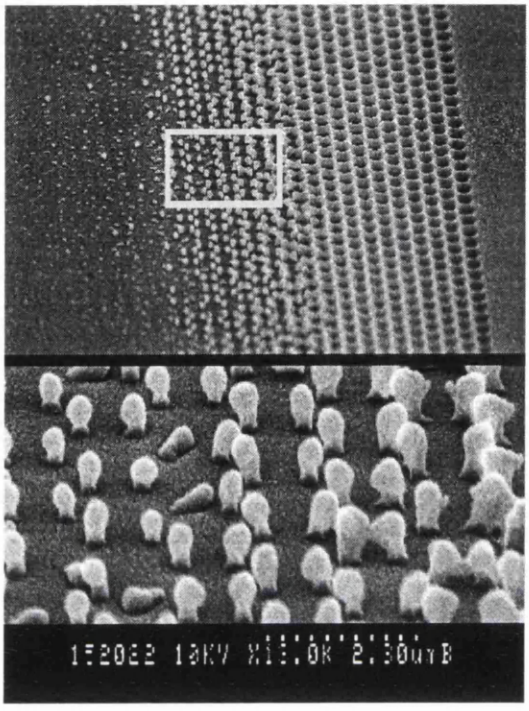

Fig. 7.1 SEM micrograph showing dose variation across a pattern. The original pattern had uniform sized holes across the whole area.

There are many possible strategies to overcome this problem, which include dose-correction, shape-correction, low kV exposure and the use of membranes [178]. These techniques have many disadvantages, which include the need for time-consuming pre-processing of the pattern file and the increase in the complexity of fabrication. Another approach which requires less preprocessing of the pattern file is a technique called ghosting. This technique equalises the back-scattered electron energy dose at all points in the pattern [178]. Analytical formulae exist to determine both the spot size and dose necessary to accurately correct the background dose level. Therefore, this approach has many advantages over the other techniques and it can be easily implemented on the existing machine. The only disadvantage is that this correction algorithm requires a negative image of the original pattern to be written over the same area as the original pattern. Potentially,

with long job times, this correction algorithm could cause problems due to pattern misalignments.

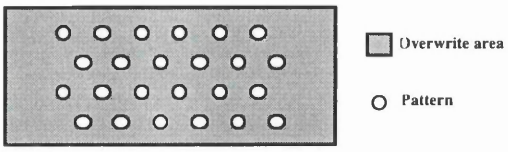

Fig. 7.2 Schematic of overwrite strategy used in preliminary experiments.

An approximate approach that I have tried in an attempt to equalise the background level was to overwrite the pattern with a non-pattern related feature at a fraction of the clearing dose. Specifically, 2D photonic bandgap structures were overwritten by an oversized rectangle with various doses ranging from 35 to 60 $\mu C/cm^2$ with an 80 nm spot size (Fig. 7.2). These initial results show the inadequacies of this technique as the differences in background exposure have been increased (Fig. 7.3). The next iteration of this technique would be to grade the dose over the pattern in a manner which would more accurately compensate for the variation in the background dose levels. It is intended that this approach be examined and its accuracy compared to the GHOST correction algorithm as back-scatter correction may be required on future work in which I will be involved.

The problem of the long writing times required, especially for device structures, as mentioned above restricts the use of the GHOST correction mechanism. The job time, however, is a function of many parameters including the resist sensitivity, so the writing time could be decreased by the use of a more sensitive resist. Some current resists have a sensitivity which is an order of magnitude higher than that of PMMA and would therefore reduce the writing time to minutes rather than hours. A more sensitive resist would also have the benefit that drift in the stage position would be less over the writing time, which reduce pattern misalignments.

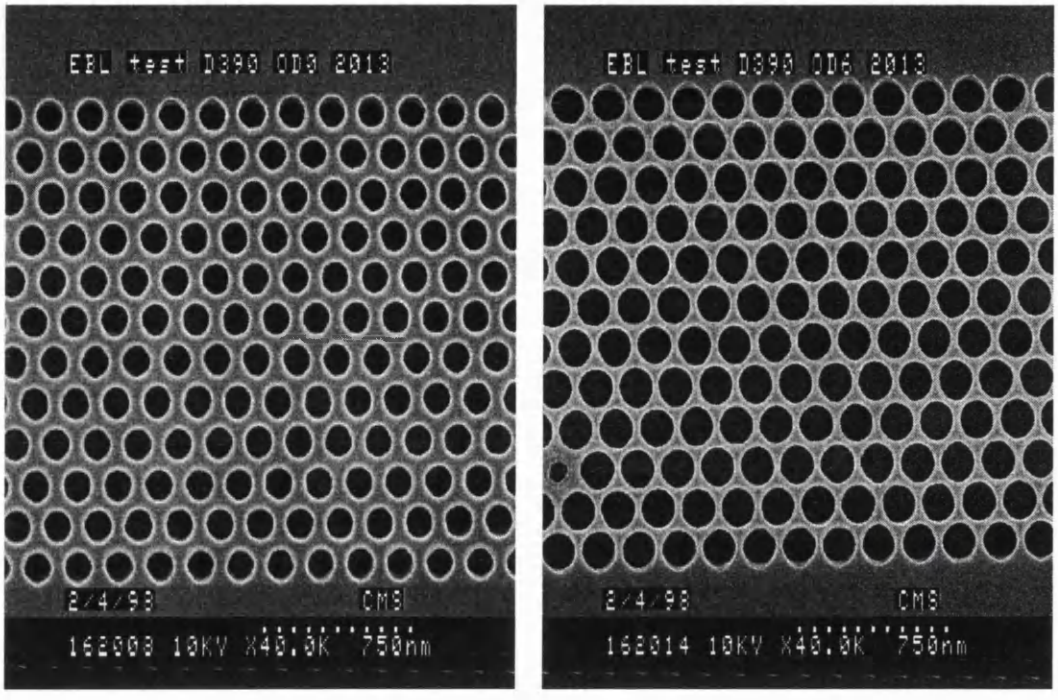

Fig. 7.3 SEM micrograph of pattern with no overwriting (left) and overwriting at 60 $\mu C/cm^2$ (right).

Some preliminary experiments have been carried out using UVIII - a positive, chemically amplified DUV resist. 2D PBG patterns were written at an acceleration voltage of 50 kV with doses ranging from 15 to 100 $\mu C/cm^2$. The results were encouraging, as the PBG patterns have been generated with reasonable accuracy and there was a reasonable uniformity in the feature size for a period of 290 nm (Fig. 7.4a). However, when similar structures with smaller periods (185 nm) were written, the problems of uniformity became more evident (Fig. 7.4b). The problems of uniformity possibly relate to the lower number of electrons that are used to write these holes and so electron noise fluctuations will have a more pronounced affect on feature definition. This problem could be overcome by using an acceleration voltage of 100 kV where higher doses are required and, therefore, the problems of uniformity are expected to reduce. I plan to carry out further experiments to assess the feasibility of using higher sensitivity resists for generation of PBG structures.

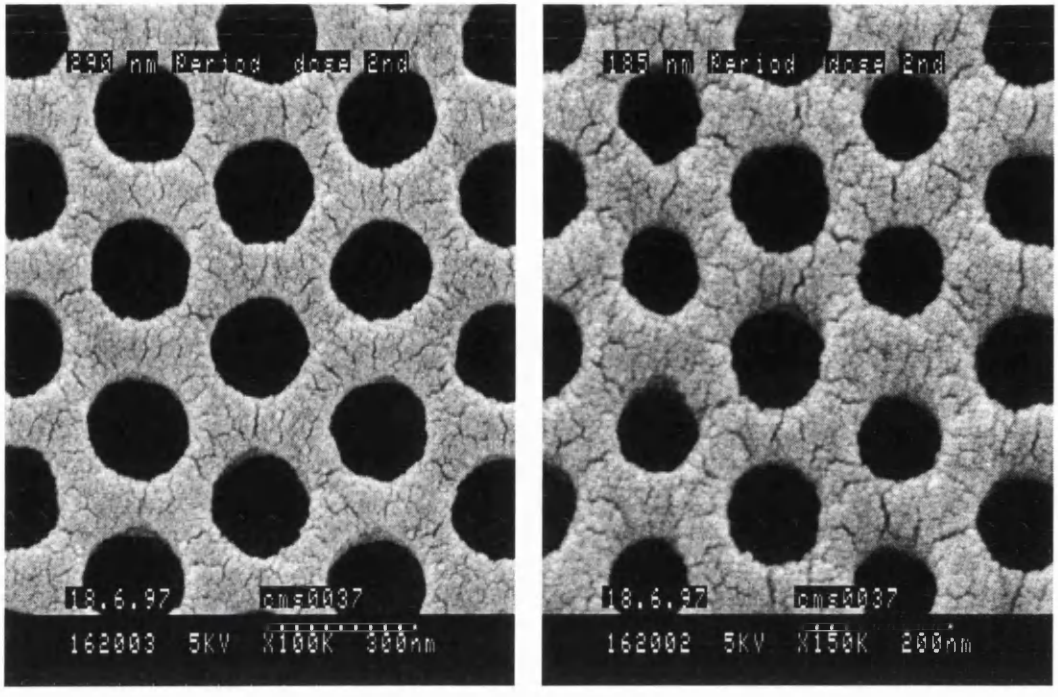

(a) **(b)**

Fig. 7.4 SEM micrograph of 2D PBG structure exposed at 50 kV for (a) 290 nm period and (b) 185 nm period.

The results in previous chapters indicate that the pattern generation can be carried out with good reproducibility. However, there is much that could be done to improve the definition of PBG structures, for example a better proximity effect correction scheme and more sensitive resists.

7.2 Wet, thermal oxidation of AlAs in optoelectronic devices

There are many potential uses of wet, thermal oxidation of AlGaAs layer, some of which have already been discussed. The use of aluminium oxide as a pattern transfer mask has been demonstrated during this project [108, 113] but the limits of this technique have not been explored. In addition to highlighting the further work that should be done in this area, other potential uses of oxidation technology is discussed.

7.2.1 Intermediate pattern transfer mask

It has already been demonstrated that the wet, thermal oxidation of an AlAs layer produces a robust mask for pattern transfer to GaAs. Selectivities of the oxidised mask to GaAs as high as 70:1 have been demonstrated for high power etching in $SiCl_4/O_2$. The robustness of the mask is a significant improvement over current deposited masks. However, more work is required to investigate the capabilities of this technique for the fabrication of nanometre sized features with very high aspect ratios (>10:1). Intrinsic to these studies would be an investigation of the ability to subsequently pattern the oxide and the ability to remove it without inducing damage in the underlying heterostructure. The combination of all these properties and the robustness of these oxide layers could simplify the fabrication of optoelectronic devices, particularly those fabricated on semi-insulating substrates, where lateral current injection is required.

7.2.2 Increased out-of-plane confinement

One of the original uses of steam oxidised AlGaAs layers was to provide increased optical confinement in VCSELs. The increased optical confinement was a direct consequence of the decrease in refractive index that results when AlGaAs ($n \approx 3.1$) is steam oxidised to form Al_2O_3 ($n \approx 1.6$). The reduction in refractive index means that the reflectivity of the Bragg stacks (alternating $\lambda/4n$ layers of GaAs and AlGaAs) is greatly increased for a constant number of layers. A consequence of the increase in the reflectivity is that the optical waveguiding in the cavity plane is increased. A simpler version of this increased guiding can be used in photonic bandgap structures, whereby an optical waveguide is placed on an AlGaAs layer, which is subsequently steam oxidised (Fig. 7.5). This approach produces a similar configuration to that of silicon on silica, which has already been used to demonstrate high Q cavities with PBG structures [102]. The great benefit of this approach is that it greatly reduces the diffractive scattering losses into the substrate, which can be potential major cause of loss in some periodic structures. The initial attempt at using an Al_2O_3 cladding layer was not successful, due to problems with the oxidation rig. These problems have now been solved and another set of photonic bandgap structures using this approach will be fabricated and tested shortly.

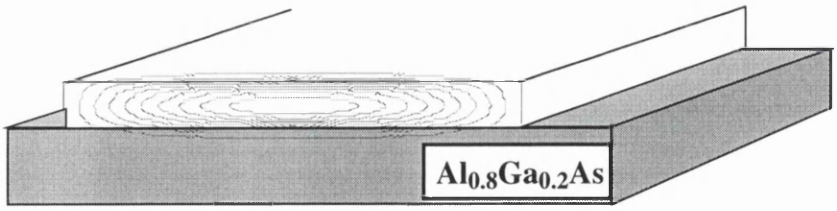

Fig. 7.5 Use of wet, thermal oxidation to create an optical membrane waveguide. The mode profile, as calculated by FWave is shown also.

7.3 Etching of InP-based materials

The fabrication of PBG structures in InP-based materials is important, particularly because of the importance of InP-based materials at telecommunications wavelengths. However, I have encountered problems in attempts to fabricate PBG structures with small periods in these materials using CH_4/H_2 (see section 3.2.4).

An alternative chemistry to CH_4/H_2 for etching of InP-based materials is based on chlorine [144]. However, the use of chlorine-based chemistry in RIE plasmas requires elevated substrate temperatures, >150 °C. Unfortunately, no investigation of this chemistry has been possible throughout this project, but I intend to evaluate this chemistry at the first available opportunity as other groups have obtained excellent results.

Reactive-ion etching machines are extremely useful in the fabrication of sub-micron features in many material systems. However, most of the high resolution results in InP have been obtained using other techniques, such as reactive-ion beam etching, electron cyclotron resonance (ECR) etching and inductively coupled plasma (ICP) etching. It may, therefore, be necessary to explore these technologies further, should no process be developed using RIE. These other techniques, particularly ECR and ICP etching offer many advantages over RIE as they allow the separate generation of the plasma species and the extraction of the plasma species towards the sample. This separation of the tasks of plasma generation and species extraction allows much more control over etching. However, ECR and ICP etching techniques are inherently more complicated due to the increased parameter set and the best solution could still be to develop a process using RIE.

Reactive-ion etching is not the only possible avenue of research I could explore in the quest to fabricate InP-based PBG structures. One technology that would be interesting to explore would be photoelectricalchemical etching or laser-assisted photochemical etching [179]. Laser illumination can generate electrons and holes, essential for electrochemical etching, and potentially could provide vertical etching at the sub-micron level. This technique has already been used in the fabrication of structures in InP [180], but there is not much information on related ternary and quaternaries. It would be interesting to explore this technology in conjunction with the other techniques in the hope that a reliable and reproducible method of fabricating sub-micron densely packed features in InP-based materials can be developed.

7.4 Loss mechanisms in microcavities with 2D PBG boundaries

Extremely encouraging results on microcavities with 2D PBG boundaries have been obtained during the course of this project. Principally, the transmission and reflection of PBG mirrors has been assessed and small mirror losses have been estimated. However, further characterisation on the 1D cavities mentioned in §6.3 indicate that the cavity losses are of the order of 30%.[20] Such a high value for the cavity losses might prevent the realisation of microcavities which could really control spontaneous emission. It is critical, therefore, for future devices that the loss mechanisms be investigated more carefully.

An investigation of losses could use existing designs and the existing experimental set-up. As explained previously, a Fabry-Perot (FP) resonator is a good device for investigating the properties of PBG structures. A series of FP cavities with

[20] These measurements have been carried out by M. Rattier at Ecole Polytéchnique, Palaiseau, France.

constant lengths, but with a varying number of rows in the PBG mirrors, will be fabricated in order to more clearly identify the contributions to the cavity losses. It is known that there will be substrate losses, so I intend to steam oxidise the $Al_{0.8}Ga_{0.2}As$ confinement layers to reduce the refractive index and this loss.

7.5 Photonic bandgap defects in GaAs materials

Microcavities in a photonic lattice can be considered as a form of defect structure. A defect is an intentionally introduced breaking of the local crystal symmetry. There are many possible defects in 2D PBG structures, which rely on adding material to or removing material from a completely symmetrical structure. In order to minimise the scattering losses into the substrate I intend to fabricate these structures on a thin membrane-like optical waveguide. This approach will also provide the smallest possible dimensions out-of-plane, thereby creating the smallest possible microcavities. The necessary confinement for such a thin waveguide could be provided by placing an appropriate waveguide structure on an $Al_{0.8}Ga_{0.2}As$ layer and steam oxidising this layer to reduce its refractive index to approximately 1.6, as described in section 7.2.2 above (Fig. 7.5).

There are various defect configurations to investigate, but my current interest is in defect structures created by increasing the area of the semiconductor bridge in the middle of three holes to form a circle [103].[21] This basic structure is then tiled to produce a structure with closely spaced defects. It is possible that the defects will couple, since there are semiconductor fins which link the defects and also the spacing between them is small enough for the confined field of the defect microcavity not to have completely decayed away. Coupled defect structures are of interest as they may show new and interesting effects. The first set of samples

[21] Discussions with Dr. T. Krauss on his return from his sabbatical at the California Institute of Technology have indicated that such a configuration is liable to provide the smallest possible dielectric defect structure.

has been fabricated (Fig. 7.6), but the oxidation to form the low index substrate was not successful. It should be noted from Fig. 7.6 that these structures will be probed using a tunable laser [93].

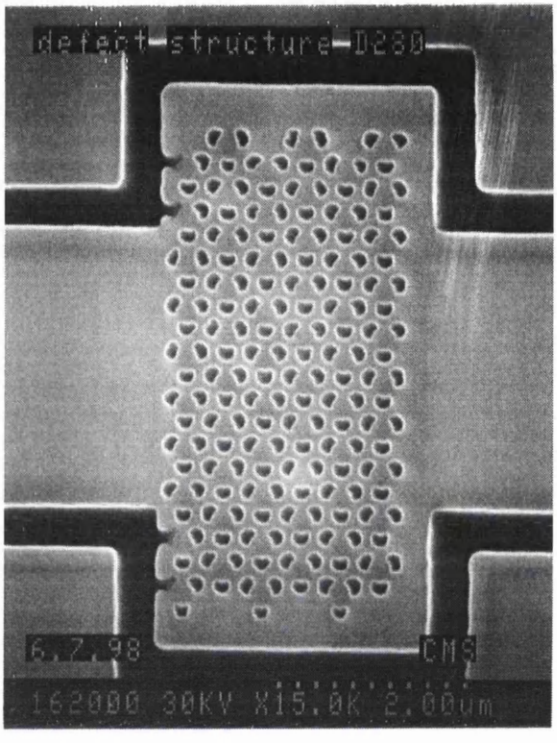

Fig. 7.6 SEM micrograph of first attempt at fabrication of defect structures on an low effective index substrate.

7.6 InP membrane waveguides

The use of thin optical waveguides will ease the fabrication difficulty of devices in the InP material system by removing the need for deep etching. Their use, however, does not remove the problem of etching sub-micron features, as discussed in §7.3. Thin optical waveguides can be fabricated in InP-based materials either by creating free standing membranes [181] or by the wet, thermal oxidation of InAlAs. The oxidation of InAlAs is not as easy as for AlGaAs as it requires higher temperatures (~500°C), which approach the desorption temperature of InP, and the oxide formed has indium oxide crystallites in it also [182].

Moreover, the refractive index of a steam oxidised InAlAs layer is only 2.4 [183], compared with 1.6 for an oxidised AlGaAs layer. This approach therefore does not appear promising.

The alternative of creating a 'free-standing' InP waveguide is more attractive, particularly as there are many selective wet etch chemistries that allow the selective etching of one InP-based alloy with respect to another [181]. Therefore, a sacrificial layer underneath the waveguide could be etched away to leave a waveguide surrounded by air. A very similar idea has already been tested, but it only removes the bottom cladding layer under the region containing the PBG structure [184]. This approach suffers from the disadvantage that there will be a large modal mismatch between the probe waveguide and the airbridge, which will cause additional reflection and make it difficult to measure both reflection and transmission. If these microstructures are to be used in devices then it will be necessary to minimise this loss, e.g. by designing a transition region which grades between the waveguide index and the lattice effective index. I intend to explore this approach more fully in the future.

7.7 Hexagonal cavities in a 2D PBG environment

The work on hexagonal cavities bounded by two-dimensional photonic bandgap structures has shown interesting results. Modes with high Q factors have been observed, but there is so far no clear picture as to why only certain modes are observed and why stronger luminescence signals are obtained for one particular period. Further investigation is required to explore these effects and to develop a theoretical model which is capable of explaining the observed effects. Once these larger cavities have been fully explained and an analytical design tool is in place, smaller cavities will be fabricated and characterised and a modification in the spontaneous emission should be observed.

7.8 Photonic crystal waveguides

The increased confinement provided by using photonic bandgap structures need not only be used in microcavity devices. This technology also has great potential in producing the lateral confinement necessary for ridge waveguides. In essence an optical waveguide can be viewed as a cavity in which either one or both of the walls have been extended to infinity and so the approach is similar to that explored already. The waveguide geometry that will be investigated is shown in Fig. 7.7, whereby a triangular array of holes is used to provide the lateral optical confinement required for thin waveguides. These structures have already been investigated theoretically and so their design is better understood [124]. Photonic crystal waveguides have already been fabricated (Fig. 7.8) but measurements were not possible as it was not possible to excite only the waveguide modes and so unguided light on either side of the photonic crystal waveguide made measurements impossible. I intend to rectify this design fault by etching trenches around the entrances to the guides, thereby ensuring only the guided light is incident at the cleaved edge.

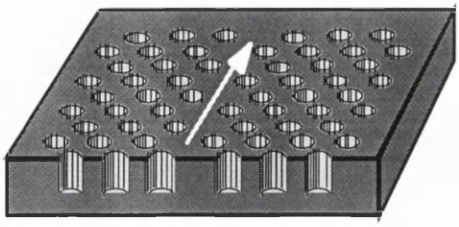

Fig. 7.7 Schematic of a photonic crystal waveguide.

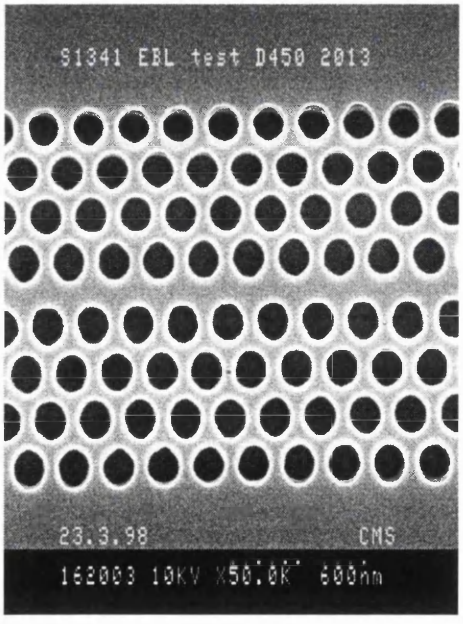

Fig. 7.8 SEM micrograph of a waveguide structure.

The characterisation of these photonic crystal waveguides is important as it may allow the development of sharp waveguide bends with minimal loss (Fig. 7.9) and large-angle Y-junctions (Fig. 7.10). However, an extensive characterisation of the waveguides is required first, with particular attention being paid to the propagation losses caused by the PBG boundaries. This assessment of PBG surface losses will be complimentary to the investigation of losses using Fabry-Perot microcavities discussed above. The ultimate aim is to develop elementary photonic integrated circuits using a combination of PBG and 'conventional' optoelectronics technology.

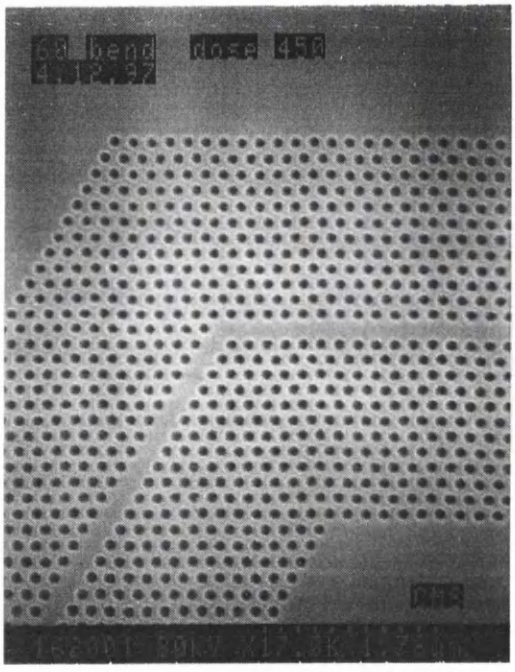

Fig. 7.9 SEM micrograph of a photonic crystal 60° bend.

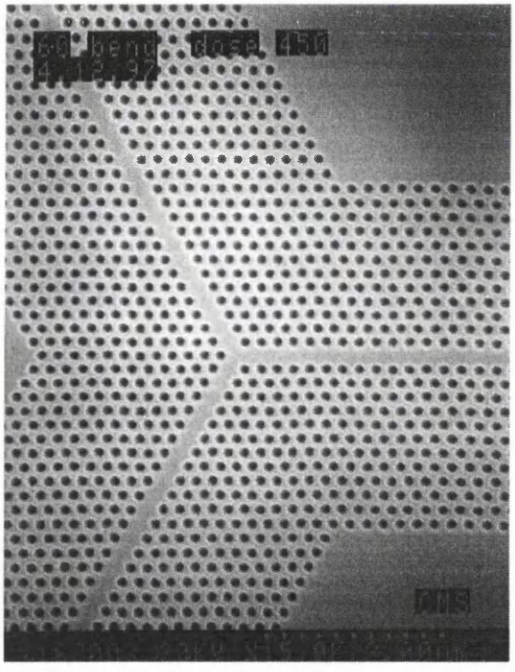

Fig. 7.10 SEM micrograph of a photonic crystal Y-junction.

7.9 Improved characterisation methods

The experimental set-up used in all the experiments reported here is extremely useful due to its high spatial resolution and versatility. However, the investigation of the hexagonal cavities is already pushing this apparatus to its limits. In particular, the focus of the excitation spot cannot be reduced much beyond the current limit due to the numerical aperture of the lens. In order to observe Purcell factors much greater than one, it will be necessary to progress to even smaller cavities than the smallest hexagonal cavity already fabricated which has an area of 2.3 μm^2 and it is highly likely that a new approach to experimental measurement will be required. One possible candidate is the use of cathodoluminescence or electron-beam pumping of devices. This technique is well established and many of the preliminary experiments in characterising semiconductor laser diodes were done using electron-beam pumping [185]. The potential advantage of this technique is that it uses electrons in vacuo as the pump source and a well collimated electron beam with a nanometre spot size can be produced. This extremely high resolution probe could be used to pump even the defect structures discussed in section 7.5 which have an area of 0.12 μm^2. The use of cathodoluminescence to characterise the smallest of the planar defect structures could lead to the observation of Purcell factors greater than one and demonstrate that planar 2D semiconductor microcavities can modify the spontaneous emission process significantly.

7.10 Electroluminescence

The ultimate aim of research into photonic bandgap structures is to apply the technology to light emitting devices, principally lasers and LEDs, which will require electrical injection of carriers. Achieving effective electrical injection into such small structures will be challenging, particularly if either vertical emission is

required or if optical membrane waveguides are used. The two key problems with such small structures are, firstly, to get the current to go where you want it and, secondly, providing the electrical contact in the first place as metal contacts are absorbing at optical frequencies. One possible solution to these many problems is the use of a transparent contact such as indium tin oxide (ITO). The use of ITO at Glasgow University, however, would require a lot of work to produce films of suitable properties, but the benefits would be extremely useful.

The other key problem for electroluminescence is the problem of surface recombination velocity (SRV), which potentially kills any benefits of microstructuring the emitter's environment. Methods of engineering the electronic bandstructure of these microcavities to reduce this drift velocity will also be required, therefore, if the true benefits of photonic crystal based microcavities are to be realised. This re-engineering has in part been demonstrated by the recent use of quantum dots, which are much more efficient at trapping electron-hole pairs. The drawback of QDs, however, is that their true benefits of narrow linewidth are only obtained at cryogenic temperatures. Much work needs to be done in this area if any of the potential benefits of microstructure emitters are to be realised.

8. Conclusions

The field of photonic microstructures was in its infancy at the start of this project with the ability to fabricate these complicated, sub-micron structures having only just been demonstrated. Much growth has taken place in the past three years and the research carried out as part of this project forms an important part in the most recent developments.

The ability to fabricate two-dimensional photonic crystals in GaAs/AlGaAs waveguides is now considered matter-of-fact since several successful demonstrations have been reported. Notwithstanding, this project has seen some improvements in the existing fabrication process as well as novel methods of pattern transfer. A similar realisation of photonic microstructures in InP waveguides, however, is still lacking and this situation needs to be rectified, particularly due to the importance of InP-based materials in light emitting devices for the telecommunications industry. The investigation of photonic crystals in InP-based materials is especially interesting as this material offers several advantages over the GaAs/AlGaAs system. The primary advantage is the lower surface recombination velocity of InP, a fact which will be essential for electroluminescent devices. There are, however, many disadvantages which include the greater difficulty of post-growth electronic bandgap engineering, the lack of suitable native oxide for increasing the optical confinement in waveguides and for increased heat-sinking ability. There still remains, therefore, much engineering and materials research to be done if the potential benefits of photonic microstructures are to be observed in InP-based materials.

The success of photonic microstructures in GaAs/AlGaAs waveguides, however, has enabled the fabrication of microcavities with photonic bandgap structure boundaries. These resonators have shown that PBG mirrors can increase the in-

plane confinement and produce modes with small linewidths (Q~1000) in micron-sized cavities. These microcavities have, however, not yet shown evidence of the modification of the emission process as the cavities either did not possess a small enough volume, the cavity Q was not large enough or the losses were too high. The ability for in-plane waveguide microcavities with PBG mirrors to modify the emission process, therefore, has still to be demonstrated, but the work carried out to date represents an important step towards this aim.

The measurements of the microcavities have highlighted the problems of PBG mirror loss and diffractive loss into the substrate that occurs in most semiconductor waveguide photonic microstructures. This problem appears to be particularly prevalent in small cavities and so this issue needs to be addressed more fully, even though some solutions have recently been suggested, as these losses could swamp any benefits to be obtained from microstructuring light-emitting devices.

Another potential killer in producing more efficient light-emitting devices is the problem of non-radiative recombination of carriers at etched surfaces. This factor by itself will prevent the realisation of devices with increased efficiency unless a suitable, cost-effective solution can be found. The related problem of carrier injection into microcavities is still a significant problem and is another reason why microstructured, electroluminescent light-emitting devices in semiconductors may not be demonstrated in the next few years.

The future of photonic microstructures is still not completely clear despite the excellent results that have been obtained to date. It appears that the benefits of photonic crystals will only be utilised in passive devices in the next few years as the efforts to overcome the substantial problems of electrical injection into microstructured semiconductor light-emitters are actively researched.

9. Publications arising from this work

9.1 Journal

1) C.J.M. Smith, S.K. Murad, T.K. Krauss, R.M. De La Rue and C.D.W. Wilkinson, "Use of polymethylmethacrylate as an initial pattern transfer mask in fluorine- and chlorine-based reactive-ion etching," to be published in J. Vac. Sci. Technol. B., Jan/Feb 1999.

2) C.J.M. Smith, T.F. Krauss, R.M. De La Rue, D. Labilloy, H. Benisty, C.Weisbuch, U. Oesterle, R. Houdré, "In-plane microcavity resonators with two dimensional photonic bandgap mirrors," to be published in IEE Proceedings J. Optoelectronics, Special Issue of Photonic Crystals, December 1998.

3) D. Labilloy, H. Benisty, C. Weisbuch, C. J. M. Smith, T. F. Krauss, R. Houdré, and U. Oesterle, "Fine structures in the near infrared transmission spectra of two-dimensional photonic band-gap crystals", accepted with minor revisions in Phys. Rev. B (Brief Report).

4) D. Labilloy, H. Benisty, C. Weisbuch, T. F. Krauss, C. J. M. Smith, R. Houdré and U. Oesterle, "High-finesse disk microcavity based on a circular Bragg reflector," Appl. Phys. Lett., **73**, 1314-1317 (1998).

5) D. Coquillat, S. K. Murad, A. Ribayrol, C. J. M. Smith, R. M. De La Rue, C. D. W.Wilkinson, O. Briot and R. L. Aulombard, "Nanometer scale reactive-ion etching of GaN epilayers," Materials Science Forum, **264-268**, 1403-1406 (1998).

6) T. K. Krauss, C. J. M. Smith, B. Vögele, S. K. Murad, C. D. W. Wilkinson, R. S. Grant, M. G. Burt and R. M. De La Rue, "Two-dimensional waveguide based photonic microstructures in GaAs and InP," Microelectronic Engineering, **35**, 29-32 (1997).

9.2 Conference

1) C.J.M. Smith, T.F. Krauss, R.M. De La Rue, D. Labilloy, H. Benisty, C.Weisbuch, U. Oesterle, R. Houdré, "Two dimensional photonic bandgap mirrors for in-plane microcavities," LEOS Annual Meeting, Orlando, USA, 1-4 Dec. 1998.

2) C.J.M. Smith, L. Hobbs, T.F. Krauss, R.M. De La Rue and M. Dawson, "1 μm scale oxide/semiconductor photonic lattice fabrication by wet oxidation methods," LEOS Annual Meeting, Orlando, USA, 1-4 Dec. 1998.

3) D. Labilloy, H. Benisty, C. Weisbuch, C.J.M. Smith, T.F. Krauss, R. Houdré and U. Oesterle, "Control of guided spontaneous emission by one and two-dimensional photonic bandgap structures," LEOS Annual Meeting, Orlando, USA, 1-4 Dec. 1998.

4) C.J.M. Smith, T.F. Krauss, S.K. Murad, C.D.W. Wilkinson, A. Boyd, C.R. Stanley, M. Dawson and R.M. De La Rue, "Modified AlAs epitaxial layers for use as pattern transfer masks," Micro- and Nano-Engineering, Leuven, Belgium 1998 to be published in special issue of Microelectronic Engineering, 1999.

5) D. Labilloy, H. Benisty, C. Weisbuch, T.F. Krauss, C.J.M. Smith, R. Houdré and U. Oesterle, "Microdisks with circular photonic bandgap boundaries exhibiting high-quality low-order modes," CLEO-Europe, Glasgow, Scotland, 14-18 Sept. 1998.

6) R.M. De La Rue, A. Ribayrol, D. Coquillat, S.K. Murad, C.J.M. Smith, C.D.W. Wilkinson, O. Briot, "Fabrication Process for Nanometer-Scale Structures by RIE in GaN Epilayers", International Topical Workshop on Contemporary Photonics Technologies, CPT '98, Tokyo, Japan, paper Pc-11-1, Digest pp.211-212, (1998).

7) R.M. De La Rue, J.S. Aitchison, B.D. Allan, J.M. Arnold, E.A. Avrutin, M.Izutsu, X. Liu, J.H. Marsh, P. Millar, S.K.Murad, C.J.M. Smith, C.D.W. Wilkinson and T.F. Krauss, "III-V Semiconductor Waveguide Photonic Microstructures Programmable for Nonlinear, Sub-Picosecond and TeraHertz Applications," NSNPS workshop in British Columbia (29th-30th March 1998).

8) R. M. De La Rue, T. F. Krauss, C. J. M. Smith, S. Thoms, L. Hobbs, J. H. Marsh, A. C. Bryce, A. Ribayrol, S. Aitchison, C. D. W. Wilkinson, C. R. Stanley, S. K. Murad, S. G. Romanov, N. P. Johnson, D. Coquillat, O. Painter, A. Shere, A. V. Fokin, V. Y. Butko, V. I. Aperovich, O. Briot, R. Aulombard, D. Cassagne, C. Jouanin, R. S. Grant, M. G. Burt, M. Dawson, M. E. Pemble, H. M. Yates, J. S. Roberts, H. Benisty, D. Labilloy, C. Weisbuch, R. Houdré, U. Oesterle, V. Bardinal, C. Sotomayor-Torres, S. Brand and B. Vögele, " New developments in research on photonic microstructures based in epitaxial III-V semiconductors, QE-13 (UK National Quantum Electronics Meeting) Cardiff, 1997. (pp.61-63 of the conference digest).

10. Bibliography

[1] T. H. Maiman, "Stimulated optical radiation in ruby lasers," *Nature*, **187**, pp. 493, 1960.

[2] K. C. Kao and G. A. Hockham, "Dielectric fibre surface waveguides for optical frequencies," *Proceedings IEE*, **133**, pp. 1151-1158, 1966.

[3] D. B. Anderson, "An integrated circuit approach to optical waveguide," presented at IEEE Microelectronics Symposium, St. Louis, Miss., USA, 1968.

[4] E. Hecht, *Optics*, 2nd ed: Addison-Wesley, 1987.

[5] J. Gowar, *Optical Communication Systems*, 2nd ed: Prentice Hall, 1993.

[6] J. Wilson and J. F. B. Hawkes, *Optoelectronics : An introduction*, 2nd ed: Prentice Hall, 1989.

[7] I. Schnitzer, E. Yablonovitch, R. Ranganathan, V. ArbetEngles, and A. Scherer, "Ultra-high external efficiency from surface textured thin-film LEDs," *LEOS Summer Topical Meeting*, pp. 3-4, 1994.

[8] P. S. Zory, *Quantum well lasers*. London: Academic Press, 1993.

[9] J.-M. Gérard, "Prospects of high-efficiency quantum boxes obtained by direct epitaxial growth," in *Confined Photons and Electrons : New Physics and Applications*, E. Burstein and C. Weisbuch, Eds. London: Plenum, 1995, pp. 357-381.

[10] J. Blondelle, H. DeNeve, G. Borghs, P. VanDaele, P. Demeester, and R. Baets, "High efficiency (20%) microcavity LEDs," *IEE Colloquium (Digest)*, pp. 12/1-12/4, 1996.

[11] E. Yablonovitch, "Inhibited Spontaneous Emission in Solid-State Physics and Electronics," *Physical Review Letters*, **58**, pp. 2059-2062, 1987.

[12] J. D. Joannopoulos, R. D. Meade, and J. N. Winn, *Photonic Crystals : Molding the Flow of Light*: Princeton University Press, 1995.

[13] C. M. Soukalis, "Photonic Band Gaps and Localization," , New York: Plenum Press, 1993.

[14] C. M. Soukalis, "Photonic Band Gap Materials," , Dordrecht: Kluwer Academic Publishers, 1996.

[15] J. Rarity and C. Weisbuch, "Microcavities and Photonic Bandgaps : Physics and Applications," , Dordrecht: Kluwer Academic Publishers, 1996.

[16] G. Morthier and P. Vankwiklberge, *Handbook of Distributed Feedback Laser Diodes*: Artech House, 1997.

[17] L. A. Coldren and S. W. Corzine, *Diode Lasers and Photonic Integrated Circuits*: John Wiley & Sons, Inc., 1995.

[18] J. A. R. Williams, I. Bennion, K. Sugden, and N. J. Doran, "Fiber Dispersion Compensation Using a Chirped in-Fiber Bragg Grating," *Electronics Letters*, **30**, pp. 985-987, 1994.

[19] J. A. R. Williams, I. Bennion, and L. Zhang, "The Compression of Optical Pulses Using Self-Phase-Modulation and Linearly Chirped Bragg-Gratings in Fibers," *IEEE Photonics Technology Letters*, **7**, pp. 491-493, 1995.

[20] J. A. R. Williams, I. Bennion, and N. J. Doran, "The Design of in-Fiber Bragg Grating Systems For Cubic and Quadratic Dispersion Compensation," *Optics Communications*, **116**, pp. 62-66, 1995.

[21] J. A. R. Williams, L. A. Everall, I. Bennion, and N. J. Doran, "Fiber Bragg grating fabrication for dispersion slope compensation," *IEEE Photonics Technology Letters*, **8**, pp. 1187-1189, 1996.

[22] H. Kogelnik and C. V. Shankn, "Coupled-Mode Theory of Distributed Feedback Lasers," *Journal of Applied Physics*, **43**, pp. 2327-2335, 1972.

[23] C. Kittel, *Introduction to Solid State Physics*, 7th ed: Wiley, 1996.

[24] E. Yablonovitch, T. J. Gmitter, and K. M. Leung, "Photonic Band-Structure - the Face-Centered-Cubic Case Employing Nonspherical Atoms," *Physical Review Letters*, **67**, pp. 2295-2298, 1991.

[25] K. M. Ho, C. T. Chan, and C. M. Soukoulis, "Existence of a Photonic Gap in Periodic Dielectric Structures," *Physical Review Letters*, **65**, pp. 3152-3155, 1990.

[26] Z. Zhang and S. Satpathy, "Electromagnetic-Wave Propagation in Periodic Structures - Bloch Wave Solution of Maxwell Equations," *Physical Review Letters*, **65**, pp. 2650-2653, 1990.

[27] K. M. Leung and Y. F. Liu, "Full Vector Wave Calculation of Photonic Band Structures in Face- Centered-Cubic Dielectric Media," *Physical Review Letters*, **65**, pp. 2646-2649, 1990.

[28] E. Yablonovitch, T. J. Gmitter, R. D. Meade, A. M. Rappe, K. D. Brommer, and J. D. Joannopoulos, "Donor and Acceptor Modes in Photonic Band-Structure," *Physical Review Letters*, **67**, pp. 3380-3383, 1991.

[29] E. Ozbay, E. Michel, G. Tuttle, R. Biswas, M. Sigalas, and K. M. Ho, "Micromachined millimeter-wave photonic band-gap crystals," *Applied Physics Letters*, **64**, pp. 2059-2061, 1994.

[30] E. Ozbay, E. Michel, G. Tuttle, R. Biswas, K. M. Ho, J. Bostak, and D. M. Bloom, "Teraherz Spectroscopy of 3-Dimensional Photonic Band-Gap Crystals," *Optics Letters*, **19**, pp. 1155-1157, 1994.

[31] E. Ozbay, A. Abeyta, G. Tuttle, M. Tringides, R. Biswas, C. T. Chan, C. M. Soukoulis, and K. M. Ho, "Measurement of a 3-Dimensional Photonic Band-Gap in a Crystal- Structure Made of Dielectric Rods," *Physical Review B-Condensed Matter*, **50**, pp. 1945-1948, 1994.

[32] E. Ozbay, "Layer-By-Layer Photonic Crystals From Microwave to Far-Infrared Frequencies," *Journal of the Optical Society of America B-Optical Physics*, **13**, pp. 1945-1955, 1996.

[33] K. E. Petersen, "Silicon as a mechanical material," *Proceedings IEEE*, **70**, pp. 420-457, 1982.

[34] K. R. Williams, "Ecth rates for micromachining processing," *Journal of Micromechanical Systems*, **5**, pp. 256-268, 1996.

[35] S. Y. Lin, J. G. Fleming, D. L. Hetherington, B. K. Smith, R. Biswas, K. M. Ho, M. M. Sigalas, W. Zubrzycki, S. R. Kurtz, and J. Bur, "A three-

dimensional photonic crystal operating at infrared wavelengths," *Nature*, **394**, pp. 251-253, 1998.

[36] K. Agi, E. R. Brown, O. B. McMahon, C. Dill, III, and K. J. Malloy, "Design of ultrawideband photonic crystals for broadband antenna applications," *Electronics Letters*, **30**, pp. 2166-2167, 1994.

[37] K. Agi, L. D. Moreland, E. Schamiloglu, M. Mojahedi, K. J. Malloy, and E. R. Brown, "Photonic Crystals - a New Quasi-Optical Component For High-Power Microwaves," *IEEE Transactions On Plasma Science*, **24**, pp. 1067-1071, 1996.

[38] E. R. Brown, C. D. Parker, and E. Yablonovitch, "Radiation Properties of a Planar Antenna On a Photonic-Crystal Substrate," *Journal of the Optical Society of America B-Optical Physics*, **10**, pp. 404-407, 1993.

[39] E. R. Brown, C. D. Parker, and O. B. McMahon, "Effect of surface composition on the radiation pattern from a photonic-crystal planar-dipole antenna," *Applied Physics Letters*, **64**, pp. 3345-3347, 1994.

[40] E. R. Brown and O. B. McMahon, "High Zenithal Directivity From a Dipole Antenna On a Photonic Crystal," *Applied Physics Letters*, **68**, pp. 1300-1302, 1996.

[41] S. D. Cheng, R. Biswas, E. Ozbay, S. McCalmont, G. Tuttle, and K. M. Ho, "Optimized Dipole Antennas On Photonic Band-Gap Crystals," *Applied Physics Letters*, **67**, pp. 3399-3401, 1995.

[42] J. S. Colburn and Y. Rahmat Samii, "Printed antenna pattern improvement through substrate perforation of high dielectric constant material: an FDTD evaluation," *Microwave and Optical Technology Letters*, **18**, pp. 27-32, 1998.

[43] T. J. Ellis and G. M. Rebeiz, "MM-wave tapered slot antennas on micromachined photonic bandgap dielectrics," *IEEE MTT-S International Microwave Symposium Digest*, **2**, pp. 1157-1160, 1996.

[44] M. P. Kesler, J. G. Maloney, B. L. Shirley, and G. S. Smith, "Antenna design with the use of photonic band-gap materials as all-dielectric planar reflectors," *Microwave and Optical Technology Letters*, **11**, pp. 169-174, 1996.

[45] W. Y. Leung, R. Biswas, S. D. Cheng, M. M. Sigalas, J. S. McCalmont, G. Tuttle, and K. M. Ho, "Slot antennas on photonic band gap crystals," *IEEE Transactions on Antennas and Propagation*, **45**, pp. 1569-1570, 1997.

[46] M. M. Sigalas, R. Biswas, and K. M. Ho, "Theoretical-Study of Dipole Antennas On Photonic Band-Gap Materials," *Microwave and Optical Technology Letters*, **13**, pp. 205-209, 1996.

[47] M. M. Sigalas, R. Biswas, Q. Li, D. Crouch, W. Leung, R. JacobsWoodbury, B. Lough, S. Nielsen, S. McCalmont, G. Tuttle, and K. M. Ho, "Dipole antennas on photonic band-gap crystals - experiment and simulation," *Microwave and Optical Technology Letters*, **15**, pp. 153-158, 1997.

[48] T. Suzuki, P. K. L. Yu, D. R. Smith, and S. Schultz, "Experimental and theoretical study of dipole emission in the two- dimensional photonic band structure of the square lattice with dielectric cylinders," *Journal of Applied Physics*, **79**, pp. 582-594, 1996.

[49] H. Y. D. Yang, N. G. Alexopoulos, and E. Yablonovitch, "Photonic band-gap materials for high-gain printed circuit antennas," *IEEE Transactions on Antennas and Propagation*, **45**, pp. 185-187, 1997.

[50] D. R. Smith, S. Schultz, S. L. McCall, and P. M. Platzmann, "Defect Studies in a 2-Dimensional Periodic Photonic Lattice," *Journal of Modern Optics*, **41**, pp. 395-404, 1994.

[51] D. R. Smith, S. Schultz, N. Kroll, M. Sigalas, K. M. Ho, and C. M. Soukoulis, "Experimental and Theoretical Results For a 2-Dimensional Metal Photonic Band-Gap Cavity," *Applied Physics Letters*, **65**, pp. 645-647, 1994.

[52] J. R. Wendt, G. A. Vawter, P. L. Gourley, T. M. Brennan, and B. E. Hammons, "Nanofabrication of Photonic Lattice Structures in GaAs/AlGaAs," *Journal of Vacuum Science & Technology B*, **11**, pp. 2637-2640, 1993.

[53] T. Krauss, Y. P. Song, S. Thoms, C. D. W. Wilkinson, and R. M. De La Rue, "Fabrication of 2-D Photonic Bandgap Structures in Gaas/Algaas," *Electronics Letters*, **30**, pp. 1444-1446, 1994.

[54] J. M. Gérard, A. Izrael, J. Y. Marzin, R. Padjen, and F. R. Ladan, "Photonic bandgap of two-dimensional dielectric crystals," *Solid-State Electronics*, **37**, pp. 1341-1344, 1994.

[55] R. M. De La Rue and T. F. Krauss, "Strategies for the fabrication of photonic microstructures in semiconductors," in *Microcavities and Photonic Bandgaps : Physics and Applications*, J. Rarity and C. Weisbuch, Eds. London: Plenum, 1995.

[56] V. N. Astratov, V. N. Bogomolov, A. A. Kaplyanskii, A. V. Prokofiev, L. A. Samoilovich, S. M. Samoilovich, and Y. A. Vlasov, "Optical spectroscopy of opal matrices with CdS embedded in its pores: Quantum confinement and photonic band gap effects," *Nuovo Cimento Della Societa Italiana Di Fisica D-Condensed Matter Atomic Molecular and Chemical Physics Fluids Plasmas Biophysics*, **17**, pp. 1349-1354, 1995.

[57] V. N. Astratov, Y. A. Vlasov, O. Z. Karimov, A. A. Kaplyanskii, Y. G. Musikhin, N. A. Bert, V. N. Bogomolov, and A. V. Prokofiev, "Photonic band gaps in 3D ordered fcc silica matrices," *Physics Letters A*, **222**, pp. 349-353, 1996.

[58] V. N. Astratov, Y. A. Vlasov, O. Z. Karimov, A. A. Kaplyanskii, Y. G. Musikhin, N. A. Bert, V. N. Bogomolov, and A. V. Prokofiev, "Photonic band structure of 3D ordered silica matrices," *Superlattices and Microstructures*, **22**, pp. 393-397, 1997.

[59] V. N. Astratov, Y. A. Vlasov, V. N. Bogomolov, A. A. Kaplyanskii, O. Z. Karimov, D. A. Kurdjukov, and A. V. Prokofiev, "Influence of refractive index contrast on photonic band gap in 3D periodic SiO_2 matrices filled with a semiconductor," *Institute of Physics Conference Series*, pp. 73-76, 1997.

[60] V. N. Bogomolov, S. V. Gaponenko, A. M. Kapitonov, A. V. Prokofiev, A. N. Ponyavina, N. I. Silvanovich, and S. M. Samoilovich, "Photonic band gap in the visible range in a three-dimensional solid state lattice," *Applied Physics A-Materials Science & Processing*, **63**, pp. 613-616, 1996.

[61] V. N. Bogomolov, D. A. Kurdyukov, A. V. Prokofev, and S. M. Samoilovich, "Effect of a photonic band gap in the optical range on solid-state SiO_2 cluster lattices - Opals," *JETP Letters*, **63**, pp. 520-525, 1996.

[62] V. N. Bogomolov, A. V. Prokofiev, S. M. Samoilovich, E. P. Petrov, A. M. Kapitonov, and S. V. Gaponenko, "Photonic band gap effect in a solid state cluster lattice," *Journal of Luminescence*, **72-4**, pp. 391-392, 1997.

[63] V. N. Bogomolov, S. V. Gaponenko, I. N. Germanenko, A. M. Kapitonov, E. P. Petrov, N. V. Gaponenko, A. V. Prokofiev, A. N. Ponyavina, N. I. Silvanovich, and S. M. Samoilovich, "Photonic band gap phenomenon and optical properties of artificial opals," *Physical Review E*, **55**, pp. 7619-7625, 1997.

[64] V. N. Bogomolov, A. V. Prokofev, and A. I. Shelykh, "Structural characterization of opal-based photonic crystals in the visible range," *Physics of the Solid State*, **40**, pp. 594-596, 1998.

[65] S. G. Romanov, A. V. Fokin, V. V. Tretijakov, V. Y. Butko, V. I. Alperovich, N. P. Johnson, and C. M. S. Torres, "Optical properties of ordered three-dimensional arrays of structurally confined semiconductors," *Journal of Crystal Growth*, **159**, pp. 857-860, 1996.

[66] S. G. Romanov, A. V. Fokin, V. I. Alperovich, N. P. Johnson, and R. M. De La Rue, "The effect of the photonic stop-band upon the photoluminescence of CdS in opal," *Physica Status Solidi a-Applied Research*, **164**, pp. 169-173, 1997.

[67] S. G. Romanov, N. P. Johnson, A. V. Fokin, V. Y. Butko, H. M. Yates, M. E. Pemble, and C. M. S. Torres, "Enhancement of the photonic gap of opal-

based three-dimensional gratings," *Applied Physics Letters*, **70**, pp. 2091-2093, 1997.

[68] S. G. Romanov, "3-dimensional photonic crystals at optical wavelengths," *Journal of Nonlinear Optical Physics & Materials*, **7**, pp. 181-200, 1998.

[69] H. Miguez, F. Meseguer, C. Lopez, A. Mifsud, J. S. Moya, and L. Vazquez, "Evidence of FCC crystallization of SiO_2 nanospheres," *Langmuir*, **13**, pp. 6009-6011, 1997.

[70] H. Miguez, F. Meseguer, C. Lopez, A. Blanco, J. S. Moya, J. Requena, A. Mifsud, and V. Fornes, "Control of the photonic crystal properties of fcc-packed submicrometer SiO_2 spheres by sintering," *Advanced Materials*, **10**, pp. 480, 1998.

[71] H. Miguez, C. Lopez, F. Meseguer, A. Blanco, L. Vazquez, R. Mayoral, M. Ocana, V. Fornes, and A. Mifsud, "Photonic crystal properties of packed submicrometric SiO_2 spheres," *Applied Physics Letters*, **71**, pp. 1148-1150, 1997.

[72] U. Gruening, V. Lehmann, and C. M. Engelhardt, "Two-dimensional infrared photonic band gap structure based on porous silicon," *Applied Physics Letters*, **66**, pp. 3254-3256, 1995.

[73] U. Gruening, V. Lehmann, S. Ottow, and K. Busch, "Macroporous silicon with a complete two-dimensional photonic band gap centered at 5 mum," *Applied Physics Letters*, **68**, pp. 747-749, 1996.

[74] U. Gruening and V. Lehmann, "Two-dimensional infrared photonic crystal based on macroporous silicon," *Thin Solid Films*, **276**, pp. 151-154, 1996.

[75] A. Birner, U. Gruning, S. Ottow, A. Schneider, F. Muller, V. Lehmann, H. Foll, and U. Gosele, "Macroporous silicon: A two-dimensional photonic bandgap material suitable for the near-infrared spectral range," *Physica Status Solidi A-Applied Research*, **165**, pp. 111-117, 1998.

[76] K. Inoue, M. Wada, K. Sakoda, A. Yamanaka, M. Hayashi, and J. W. Haus, "Fabrication of 2-Dimensional Photonic Band-Structure With Near- Infrared

Band-Gap," *Japanese Journal of Applied Physics Part 2-Letters*, **33**, pp. L1463-L1465, 1994.

[77] K. Inoue, M. Wada, K. Sakoda, M. Hayashi, T. Fukushima, and A. Yamanaka, "Near-Infrared Photonic Band-Gap of 2-Dimensional Triangular Air-Rod Lattices As Revealed By Transmittance Measurement," *Physical Review B-Condensed Matter*, **53**, pp. 1010-1013, 1996.

[78] K. Inoue, "Optical properties of 2D photonic crystals," *Pacific Rim Conference on Lasers and Electro-Optics, CLEO - Technical Digest*, pp. 40, 1997.

[79] J. C. Knight, T. A. Birks, D. M. Atkin, and P. S. J. Russell, "Two-dimensional photonic crystal material in fibre form," *Conference on Lasers and Electro-Optics Europe - Technical Digest*, pp. 75, 1996.

[80] J. C. Knight, T. A. Birks, P. S. J. Russell, and D. M. Atkin, "All-silica single-mode optical fiber with photonic crystal cladding," *Optics Letters*, **21**, pp. 1547-1549, 1996.

[81] J. C. Knight, T. A. Birks, P. S. J. Russell, and J. G. Rarity, "Bragg scattering studies of a photonic crystal fiber," *Conference Proceedings - Lasers and Electro-Optics Society Annual Meeting-CLEO*, **11**, pp. 527-528, 1997.

[82] J. C. Knight, T. A. Birks, P. S. J. Russell, and J. G. Rarity, "Bragg scattering from an obliquely illuminated photonic crystal fiber," *Applied Optics*, **37**, pp. 449-452, 1998.

[83] J. C. Knight, T. A. Birks, P. StJrussell, and J. P. deSandro, "Properties of photonic crystal fiber and the effective index model," *Journal of the Optical Society of America A: Optics and Image Science, and Vision*, **15**, pp. 748-752, 1998.

[84] K. Fukuda, H. Sun, S. Matsuo, and H. Misawa, "Self-organizing three-dimensional colloidal photonic crystal structure with augmented dielectric contrast," *Japanese Journal of Applied Physics Part 2-Letters*, **37**, pp. L508-L511, 1998.

[85] T. Konishi and N. Ise, "Ultra-Small-Angle X-Ray-Scattering Profile of Colloidal Silica Crystal of 4-Fold Symmetry," *Journal of the American Chemical Society*, **117**, pp. 8422-8424, 1995.

[86] T. Konishi and N. Ise, "Single crystal of colloidal silica particles in a dilute aqueous dispersion as studied by a two-dimensional ultrasmall-angle x-ray scattering," *Physical Review B-Condensed Matter*, **57**, pp. 2655-2658, 1998.

[87] Z. Y. Li, J. Wang, and B. Y. Gu, "Creation of partial band gaps in anisotropic photonic-band-gap structures," *Physical Review B-Condensed Matter*, **58**, pp. 3721-3729, 1998.

[88] D. F. Sievenpiper, M. E. Sickmiller, and E. Yablonovitch, "3-D metallic photonic bandgap structures," *Conference Proceedings - Lasers and Electro-Optics Society Annual Meeting*, pp. 387, 1996.

[89] D. F. Sievenpiper, E. Yablonovitch, J. N. Winn, S. Fan, P. R. Villeneuve, and J. D. Joannopoulos, "3D metallo-dielectric photonic crystals with strong capacitive coupling between metallic islands," *Physical Review Letters*, **80**, pp. 2829-2832, 1998.

[90] K. A. McIntosh, L. J. Mahoney, K. M. Molvar, O. B. McMahon, S. Verghese, M. Rothschild, and E. R. Brown, "Three-dimensional metallodielectric photonic crystals exhibiting resonant infrared stop bands," *Applied Physics Letters*, **70**, pp. 2937-2939, 1997.

[91] K. A. McIntosh, O. B. McMahon, and S. Verghese, "Three-dimensional metallodielectric photonic crystals incorporating flat metal elements," *Microwave and Optical Technology Letters*, **17**, pp. 153-156, 1998.

[92] M. Scalora, M. J. Bloemer, A. S. Pethel, J. P. Dowling, C. M. Bowden, and A. S. Manka, "Transparent, metallo-dielectric, one-dimensional, photonic band-gap structures," *Journal of Applied Physics*, **83**, pp. 2377-2383, 1998.

[93] T. F. Krauss and R. M. De La Rue, "Optical characterization of waveguide based photonic microstructures," *Applied Physics Letters*, **68**, pp. 1613-1615, 1996.

[94] D. Cassagne, C. Jouanin, and D. Bertho, "New Hexagonal Structures For 2-Dimensional Photonic Band-Gap Materials," *Nuovo Cimento Della Societa Italiana Di Fisica D-Condensed Matter Atomic Molecular and Chemical Physics Fluids Plasmas Biophysics*, **17**, pp. 1401-1405, 1995.

[95] D. Cassagne, C. Jouanin, and D. Bertho, "Hexagonal Photonic-Band-Gap Structures," *Physical Review B-Condensed Matter*, **53**, pp. 7134-7142, 1996.

[96] D. Cassagne, C. Jouanin, and D. Bertho, "Optical properties of two-dimensional photonic crystals with graphite structure," *Applied Physics Letters*, **70**, pp. 289-291, 1997.

[97] Y. Chen, G. Faini, H. Launois, and J. Etrillard, "Fabrication of two-dimensional photonic lattices in GaAs: the regular graphite structures," *Superlattices and Microstructures*, **22**, pp. 109-113, 1997.

[98] P. S. J. Russell, D. M. Atkin, T. A. Birks, and P. J. Roberts, "Bound modes of two-dimensional photonic crystals," in *Microcavities and Photonic Bandgaps: Physics and Applications*, J. R. Rarity and C. Weisbuch, Eds. London: Kluwer Academic Publishers, 1996.

[99] T. F. Krauss, R. M. De La Rue, and S. Brand, "2-Dimensional Photonic-Bandgap Structures Operating At Near-Infrared Wavelengths," *Nature*, **383**, pp. 699-702, 1996.

[100] T. F. Krauss, B. Vogele, C. R. Stanley, and R. M. De La Rue, "Waveguide microcavity based on photonic microstructures," *IEEE Photonics Technology Letters*, **9**, pp. 176-178, 1997.

[101] D. Labilloy, H. Benisty, C. Weisbuch, T. F. Krauss, V. Bardinal, and U. Oesterle, "Demonstration of cavity mode between two-dimensional photonic-crystal mirrors," *Electronics Letters*, **33**, pp. 1978-1980, 1997.

[102] J. S. Foresi, P. R. Villeneuve, J. Ferrera, E. R. Thoen, G. Steinmeyer, S. Fan, J. D. Joannopoulos, L. C. Kimerling, H. I. Smith, and E. P. Ippen, "Photonic-bandgap microcavities in optical waveguides," *Nature*, **390**, pp. 143-145, 1997.

[103] T. F. Krauss, M. Boroditsky, R. Cocciolo, O. Painter, A. Sherer, and E. Yablonovitch, "Photonic crystal microcavity enhanced LEDs," presented at Conference on Lasers and Electro-optics - Europe, Glasgow, Scotland, 1998.

[104] D. Labilloy, H. Benisty, C. Weisbuch, T. F. Krauss, R. M. De La Rue, V. Bardinal, R. Houdre, U. Oesterle, D. Cassagne, and C. Jouanin, "Quantitative measurement of transmission, reflection, and diffraction of two-dimensional photonic band gap structures at near-infrared wavelengths," *Physical Review Letters*, **79**, pp. 4147-4150, 1997.

[105] C. C. Cheng and A. Scherer, "Fabrication of Photonic Band-Gap Crystals," *Journal of Vacuum Science & Technology B*, **13**, pp. 2696-2700, 1995.

[106] C. C. Cheng, A. Scherer, V. ArbetEngels, and E. Yablonovitch, "Lithographic band gap tuning in photonic band gap crystals," *Journal of Vacuum Science & Technology B*, **14**, pp. 4110-4114, 1996.

[107] C. C. Cheng, V. ArbetEngels, A. Scherer, and E. Yablonovitch, "Nanofabricated three dimensional photonic crystals operating at optical wavelengths," *Physica Scripta T*, **T68**, pp. 17-20, 1996.

[108] C. C. Cheng, A. Scherer, R. C. Tyan, Y. Fainman, G. Witzgall, and E. Yablonovitch, "New fabrication techniques for high quality photonic crystals," *Journal of Vacuum Science & Technology B*, **15**, pp. 2764-2767, 1997.

[109] J. Obrien, O. Painter, R. Lee, C. C. Cheng, A. Yariv, and A. Scherer, "Lasers incorporating 2D photonic bandgap mirrors," *Electronics Letters*, **32**, pp. 2243-2244, 1996.

[110] T. F. Krauss, O. Painter, A. Scherer, J. S. Roberts, and R. M. De La Rue, "Photonic microstructures as laser mirrors," *Optical Engineering*, **37**, pp. 1143-1148, 1998.

[111] D. Labilloy, H. Benisty, C. Weisbuch, T. F. Krauss, C. J. M. Smith, R. Houdre, and U. Oesterle, "High-finesse disk microcavity based on a circular Bragg reflector," *Applied Physics Letters*, **73**, pp. 1314-1316, 1998.

[112] C. J. M. Smith, S. K. Murad, T. F. Krauss, R. M. De La Rue, and C. D. W. Wilkinson, "Use of polymethylmethacrylate as an initial pattern transfer layer in fluorine- and chlorine-based reactive-ion etching," *Journal of Vacuum Science and Technology B*, 1999.

[113] C. J. M. Smith, T. F. Krauss, S. K. Murad, C. D. W. Wilkinson, A. Boyd, C. R. Stanley, M. Dawson, and R. M. De La Rue, "Modified AlAs epitaxial layers for use as pattern transfer masks," presented at Micro- and Nano-Engineering 1998, Leuven, Belgium, 1998.

[114] C. J. M. Smith, T. F. Krauss, R. M. De La Rue, D. Labilloy, H. Benisty, C. Weisbuch, U. Oesterle, and R. Houdré, "In-plane microcavity resonators with two dimensional photonic bandgap mirrors," *IEE Proc. J - Optoelectronics*, 1998.

[115] D. K. Cheng, *Field and Wave Electromagnetics*, 2nd ed: Adison-Wesley Publishing Company, 1989.

[116] J. D. Kraus, *Electromagnetics*, 4th ed: McGraw-Hill, Inc., 1992.

[117] P. S. J. Russell, "Coupled wave versus modal theory in uniform dielectric gratings," *Optics Communications*, **48**, pp. 71-74, 1983.

[118] P. S. Russell, "Novel Thick-Grating Beam-Squeezing Device in Ta_2O_5 Corrugated Planar Waveguide," *Electronics Letters*, **20**, pp. 72-73, 1984.

[119] R. Zengerle, "Light propagation in singly and doubly periodic planar waveguides," *Journal of Modern Optics*, **34**, pp. 1589-1617, 1987.

[120] M. L. Cohen and J. R. Chelikowsky, *Electronic and Optical Properties of Semiconductors*. Berlin: Springer Verlag, 1987.

[121] J. W. Haus, "A Brief Review of Theoretical Results For Photonic Band Structures," *Journal of Modern Optics*, **41**, pp. 195-207, 1994.

[122] R. D. Meade, A. M. Rappe, K. D. Brommer, J. D. Joannopoulos, and O. L. Alerhand, "Accurate Theoretical-Analysis of Photonic Band-Gap Materials," *Physical Review B-Condensed Matter*, **48**, pp. 8434-8437, 1993.

[123] P. R. Villeneuve and M. Piche, "Photonic bandgaps in periodic dielectric structures," *Progress in Quantum Electronics*, **18**, pp. 153-200, 1994.

[124] H. Benisty, "Modal-Analysis of Optical Guides With 2-Dimensional Photonic Band-Gap Boundaries," *Journal of Applied Physics*, **79**, pp. 7483-7492, 1996.

[125] J. B. Pendry and A. Mackinnon, "Calculation of Photon Dispersion-Relations," *Physical Review Letters*, **69**, pp. 2772-2775, 1992.

[126] J. B. Pendry, "Photonic Band Structures," *Journal of Modern Optics*, **41**, pp. 209-229, 1994.

[127] V. Berger, "Les matériaux a bande interdite photonique," Thomson-CSF, Orsay 08/95 1995.

[128] A. Taflove and M. E. Brodwin, "Numerical solution of steady-state electromagnetic scattering problems using the time-dependent Maxwell's equations," *IEEE Trans. Microwave Theory and Techniques*, **23**, pp. 623, 1975.

[129] D. Felbacq, D. Maystre, and G. Tayeb, "Localization of Light By a Set of Parallel Cylinders," *Journal of Modern Optics*, **42**, pp. 473-482, 1995.

[130] A. Mekis, J. C. Chen, I. Kurland, S. H. Fan, P. R. Villeneuve, and J. D. Joannopoulos, "High transmission through sharp bends in photonic crystal waveguides," *Physical Review Letters*, **77**, pp. 3787-3790, 1996.

[131] T. Tamir, "Integrated Optics," in *Topics in Applied Physics*, Berlin: Springer Verlag, 1975.

[132] O. Graydon, "Nature's nanostructures colour wings and stones," in *Opto and Laser Europe*, 1998, pp. 31-36.

[133] H. I. Smith and M. L. Schattenburg, "X-ray lithography, from 500 to 30 nm : X-ray nanolithography," *IBM Journal of Research and Development*, **37**, pp. 319-327, 1993.

[134] V. Berger, O. GauthierLafaye, and E. Costard, "Fabrication of a 2D photonic bandgap by a holographic method," *Electronics Letters*, **33**, pp. 425-426, 1997.

[135] J. A. Liddle, S. D. Berger, C. J. Biddick, M. I. Blakey, K. J. Bolan, S. W. Bowler, K. Brady, R. M. Camarda, W. F. Connelly, A. Crorken, J. Custy,

R. C. Farrow, J. A. Felker, L. A. Fetter, B. Freeman, L. R. Harriott, L. Hopkins, H. A. Huggins, C. S. Knurek, J. S. Kraus, D. A. Mixon, M. M. Mkrtchyan, A. E. Novembre, M. L. Peabody, W. M. Simpson, R. G. Tarascon, H. H. Wade, W. K. Waskiewicz, G. P. Watson, J. K. Williams, and D. L. Windt, "The SCattering with angular limitation in projection electron-beam lithography (SCALPEL) system," *Japanese Journal of Applied Physics Part 1-Regular Papers Short Notes & Review Papers*, **34**, pp. 6663-6671, 1995.

[136] L. R. Harriott, S. D. Berger, C. Biddick, M. I. Blakey, S. W. Bowler, K. Brady, R. M. Camarda, W. F. Connelly, A. Crorken, J. Custy, R. Dimarco, R. C. Farrow, J. A. Felker, L. Fetter, R. Freeman, L. Hopkins, H. A. Huggins, C. S. Knurek, J. S. Kraus, J. A. Liddle, M. Mkrtychan, A. E. Novembre, M. L. Peabody, R. G. Tarascon, H. H. Wade, W. K. Waskiewicz, G. P. Watson, K. S. Werder, and D. Windt, "Preliminary results from a prototype projection electron-beam stepper-scattering with angular limitation projection electron beam lithography proof-of-concept system," *Journal of Vacuum Science & Technology B*, **14**, pp. 3825-3828, 1996.

[137] L. R. Harriott, "Scattering with angular limitation projection electron beam lithography for suboptical lithography," *Journal of Vacuum Science & Technology B*, **15**, pp. 2130-2135, 1997.

[138] S. Y. Chou, P. R. Krauss, and P. J. Renstrom, "Imprint lithography with 25-nanometer resolution," *Science*, **272**, pp. 85-87, 1996.

[139] S. Y. Chou, P. R. Krauss, W. Zhang, L. J. Guo, and L. Zhuang, "Sub-10 nm imprint lithography and applications," *Journal of Vacuum Science & Technology B*, **15**, pp. 2897-2904, 1997.

[140] S. Y. Chou, P. R. Krauss, and P. J. Renstrom, "Nanoimprint lithography," *Journal of Vacuum Science & Technology B*, **14**, pp. 4129-4133, 1996.

[141] B. G. Casey, D. R. S. Cumming, I. I. Khandaker, and C. D. W. Wilkinson, "Nanoscale embossing of polymers using a thermoplastic die," presented at Micro- and Nano-Engineering, Leuven, Belgium, 1998.

[142] N. Tanaka, H. Kawanishi, and T. Ishikawa, "Photoluminescence Study of Electron-Beam-Induced Damage in GaAs/AlGaAs Quantum-Well Structures," *Japanese Journal of Applied Physics*, **32**, pp. 540-543, 1993.

[143] A. Grill, *Cold Plasma in Materials Fabrication*: IEEE Press, 1994.

[144] K. Asakawa, T. Yoshikawa, S. Kohmoto, Y. Nambu, and Y. Sugimoto, "Chlorine-based dry etching of III/V compound semiconductors for optoelectronic application," *Japanese Journal of Applied Physics Part 1-Regular Papers Short Notes & Review Papers*, **37**, pp. 373-387, 1998.

[145] J. Daleiden, K. Eisele, R. E. Sah, K. H. Schmidt, and J. D. Ralston, "Chemical-Analysis of a $Cl_2/BCl_3/IBr_3$ Chemically Assisted Ion-Beam Etching Process For GaAs and InP Laser-Mirror Fabrication Under Cryo- Pumped Ultrahigh-Vacuum Conditions," *Journal of Vacuum Science & Technology B*, **13**, pp. 2022-2024, 1995.

[146] K. M. Eisele, J. Daleiden, and J. Ralston, "Low temperature chemically assisted ion-beam etching processes using Cl_2, CH_3I, and IBr_3 to etch InP optoelectronic devices," *Journal of Vacuum Science & Technology B*, **14**, pp. 1780-1783, 1996.

[147] S. K. Murad, "Characterization of dry etching processes of III-V semiconductors in silicon tetrachloride plasmas," *Thesis submitted in Electronics & Electrical Engineering*, University of Glasgow, 1993.

[148] S. K. Murad, C. D. W. Wilkinson, and S. P. Beaumont, "Selective and non-selective reactive-ion etching of GaAs and AlGaAs in $SiCl_4$ plasma," *Microelectronic Engineering*, **23**, pp. 357-360, 1994.

[149] S. K. Murad, N. I. Cameron, S. P. Beaumont, and C. D. W. Wilkinson, "Effects of O_2 addition to $SiCl_4/SiF_4$ and the thickness of the capping layer on gate

recess etching of GaAs pseudomorphic high electron mobility transistors.," *Journal of Vacuum Science and Technology B*, **14**, pp. 3668-3673, 1996.

[150] T. Baba, N. Kamizawa, and M. Ikeda, "Nanofabrication of GaInAsP/InP 2-dimensional photonic crystals by a methane-based reactive ion beam etching," *Physica B: Condensed Matter*, **227**, pp. 415-418, 1996.

[151] T. Baba and T. Matsuzaki, "Fabrication and photoluminescence studies of GaInAsP/InP 2- dimensional photonic crystals," *Japanese Journal of Applied Physics, Part 1: Regular Papers & Short Notes & Review Papers*, **35**, pp. 1348-1352, 1996.

[152] T. Yoshikawa, S. Kohmoto, and K. Asakawa, "Cl_2 ECR Plasma Etching of III/V Semiconductors and Its Application to Photonic Devices," *Electronics and Communications in Japan*, **77**, pp. 260-237, 1994.

[153] S. Miyakuni, R. Hattori, K. Sato, H. Takano, and O. Ishihara, "Low Ion Energy Electron-Cyclotron-Resonance Etching of InP Using a Cl_2/N_2 Mixture," *Journal of Applied Physics*, **78**, pp. 5734-5738, 1995.

[154] M. Kushida, Y. Imaizumi, K. Harada, N. Ueno, and K. Sugita, "Dry-etching durability of copolymers and polymer blends of vinylnaphthalene or alpha-methylstyrene with methyl methacrylate," *Japanese Journal of Applied Physics, Part 1: Regular Papers & Short Notes & Review Papers*, **34**, pp. 4234-4238, 1995.

[155] "CRC Handbook of Chemistry and Physics," , 73rd ed, pp. 9-131.

[156] Y. Hikosaka, H. Toyoda, and H. Sugai, "Drastic Change in CF_2 and CF_3 Kinetics by Hydrogen Addition into CF_4 Etching Plasma," *Japanese Journal of Applied Physics Part 2-Letters*, **32**, pp. L690-L693, 1993.

[157] N. Omori, H. Matsuo, S. Watanabe, and M. Puschmann, "Influence of carbon monoxide gas on silicon dioxide dry etching," *Surface Science*, **352-354**, pp. 988-992, 1996.

[158] D. Coquillat, S. K. Murad, A. Ribayrol, C. J. M. Smith, R. M. De La Rue, C. D. W. Wilkinson, O. Briot, and R. L. Aulombard, "Nanometre scale

reactive ion etching of GaN epilayers," *Materials Science Forum*, **264-268**, pp. 1403-1406, 1998.

[159] K. D. Choquette, F. M. Geib, C. I. H. Ashby, R. D. Twesten, O. Blum, H. Q. Hou, D. M. Follstaedt, B. E. Hammons, D. Mathes, and R. Hull, "Advances in selective wet oxidation of AlGaAs alloys," *IEEE Journal of Selected Topics in Quantum Electronics*, **3**, pp. 916-925, 1997.

[160] N. Holonyak, "AlGaAs Native Oxide," International patent, WO 92/12536, 1992.

[161] R. D. Twesten, D. M. Follstaedt, K. D. Choquette, and R. P. Schneider, "Microstructure of laterally oxidised AlGaAs layers in vertical-cavity lasers," *Applied Physics Letters*, **69**, pp. 19-21, 1996.

[162] H. R. Borsje, H. M. Jaeger, and S. Radelaar, "Ultra-high resolution negative e-beam resist: AlF_3," *Microelectronic Engineering*, **17**, pp. 311-314, 1992.

[163] S. F. Pellicori and E. Colton, "Fluoride compounds for IR coatings," *Thins Solid Films*, **209**, pp. 109-115, 1992.

[164] K. Hjort, "Sacrificial etching of III-V compounds for micromechanical devices," *Journal of Micromechanics and Microengineering*, **6**, pp. 370-375, 1996.

[165] M. A. Afromowitz, "Refractive index of $Ga_{1-x}Al_xAs$," *Solid State Communications*, **15**, pp. 59-63, 1974.

[166] D. Labilloy, H. Benisty, C. Weisbuch, T. F. Krauss, R. Houdre, and U. Oesterle, "Use of guided spontaneous emission of a semiconductor to probe the optical properties of two-dimensional photonic crystals," *Applied Physics Letters*, **71**, pp. 738-740, 1997.

[167] L. Goldstein, F. Glas, J. Y. Marzin, M. N. Charasse, and G. Leroux, "Growth By Molecular-Beam Epitaxy and Characterization of InAs/GaAs Strained-Layer Superlattices," *Applied Physics Letters*, **47**, pp. 1099-1101, 1985.

[168] S. John, "Strong Localization of Photons in Certain Disordered Dielectric Superlattices," *Physical Review Letters*, **58**, pp. 2486-2489, 1987.

[169] E. M. Purcell, "Spontaneous Emission Probabilities at Radiofrequencies," *Physical Review*, **69**, pp. 681, 1946.

[170] H. Yokoyama, "Physics and device applications of optical microcavities," *Science*, **256**, pp. 66-70, 1992.

[171] S. L. McCall, A. F. J. Levi, R. E. Slusher, S. J. Pearton, and R. A. Logan, "Whispering-gallery mode microdisk lasers," *Applied Physics Letters*, **60**, pp. 289-291, 1992.

[172] T. Baba, "Photonic Crystals and Microdisk Cavities Based on GaInAsP-InP System," *IEEE Selected Topics in Quantum Electronics*, **3**, pp. 808-830, 1997.

[173] A. F. J. Levi, S. L. McCall, S. J. Pearton, and R. A. Logan, "Room temperature operation of submicrometre radius disk laser," *Electronics Letters*, **29**, pp. 1666-1667, 1993.

[174] U. Mohideen, W. S. Hobson, S. J. Pearton, F. Ren, and R. E. Slusher, "GaAs/AlGaAs microdisk lasers," *Applied Physics Letters*, **64**, pp. 1911-1913, 1994.

[175] S. Kristjansson, M. Li, N. Eriksson, M. Hagberg, K. J. Killius, and A. Larsson, "Circular grating coupled DBR laser with integrated focusing outcoupler," *IEEE Photonics Technology Letters*, **9**, pp. 416-418, 1997.

[176] E. Argence and T. Kahan, *Theory of Waveguides and Cavity Resonators*, English ed. London: Blackie & Son Ltd., 1967.

[177] J. M. Gerard, B. Sermage, B. Gayral, B. Legrand, E. Costard, and V. ThierryMieg, "Enhanced spontaneous emission by quantum boxes in a monolithic optical microcavity," *Physical Review Letters*, **81**, pp. 1110-1113, 1998.

[178] G. Owen and P. Rissman, "Proximity Effect Correction For Electron-Beam Lithography By Equalization of Background Dose," *Journal of Applied Physics*, **54**, pp. 3573-3581, 1983.

[179] R. Khare, E. L. Hu, J. J. Brown, and M. A. Melendes, "Micromachining in III-V Semiconductors Using Wet Photoelectrochemical Etching," *Journal of Vacuum Science & Technology B*, **11**, pp. 2497-2501, 1993.

[180] S. Adachi, "Properties of Indium Phosphide," , London: INSPEC, 1991.

[181] C. Seassal, J. L. Leclercq, and Viktorovitch, "Fabrication of InP-based freestanding microstructures by selective surface micromachining," *Journal of Micromechanical Microengineering*, **6**, pp. 261-265, 1996.

[182] P. Petit, P. Legay, G. LeRoux, G. Patriarche, G. Post, and M. Quillec, "Controlled steam oxidation of AlInAs for microelectronics and optoelectronics applications," *Journal of Electronic Materials*, **26**, pp. L32-L35, 1997.

[183] H. Takenouchi, T. Kagawa, Y. Ohiso, T. Tadokoro, and T. Kurokawa, "Laterally oxidised InAlAs-oxide/InP distributed Bragg reflectors," *Electronics Letters*, **32**, pp. 1671-1673, 1996.

[184] M. Kanskar, P. Paddon, V. Pacradouni, R. Morin, A. Busch, J. F. Young, S. R. Johnson, J. MacKenzie, and T. Tiedje, "Observation of leaky slab modes in an air-bridged semiconductor waveguide with a two-dimensional photonic lattice," *Applied Physics Letters*, **70**, pp. 1438-1440, 1997.

[185] C. A. Klein, "The Excitation Mechanism in Electron-Beam Pumped Lasers," presented at Proceedings Physics of Quantum Electronics, 1966.

GLASGOW UNIVERSITY LIBRARY